ENGINEERING STRUCTURE AND PHASE VIA TEMPERATURE MANIPULATION IN THIN FILM OXIDES GROWN BY ALD

A Dissertation
Presented to
The Academic Faculty

by

Brandon Deane Piercy

In Partial Fulfillment
of the Requirements for the Degree
Doctor of Philosophy in the
School of Materials Science and Engineering

Georgia Institute of Technology
December 2019

ENGINEERING STRUCTURE AND PHASE VIA TEMPERATURE MANIPULATION IN THIN FILM OXIDES GROWN BY ALD

Approved by:

Dr. Mark Losego, Advisor
School of Materials Science and Engineering
Georgia Institute of Technology

Dr. Nazanin Bassiri-Gharb
School of Mechanical Engineering
Georgia Institute of Technology

Dr. Eric Vogel
School of Materials Science and Engineering
Georgia Institute of Technology

Dr. William Alan Doolittle
School of Electrical and Computer Engineering
Georgia Institute of Technology

Dr. Michael Filler
School of Chemical and Biomolecular Engineering
Georgia Institute of Technology

Date Approved: October 03, 2019

To my family, who steadfastly supports me

ACKNOWLEDGEMENTS

This dissertation is the culmination of a community who has surrounded, encouraged, and provided endless support to me over the past five years. I profusely thank my parents, who laid the groundwork for me to succeed through intentional parenting, a well balanced education, and through constant sacrifice to provide me with new opportunities. I also thank my sister, a wellspring of truly new and creative ideas, who I can always rely on to hear me and whom I will always unconditionally support and love.

I would like to thank my advisor, Mark Losego, for his initial belief in me from the very beginning of this journey, and throughout my development as a scientist and engineer. This research group required a lot of faith that we would accomplish something new, especially as we spent our first year building our new reactor in our office as we waited for the power and ventilation to be installed in what would eventually become one of our several labs. I want to credit Mark for having a vision of what we could be capable of and for the five, ten, and more year plans of the reactors, equipment, and research we would be able to build and do. I believe that Mark's vision and the opportunities provided to me by Georgia Tech have unlocked many doors and given me the chance to develop and learn skills across many disciplines that I will continue to use for my entire career.

I would like to thank my coworkers in our group: Collen, Yi, Emily, Jamie, Shreya, and Shawn, whom I have had the privilege of working alongside and mentoring throughout my PhD career. Thank you all both for your help with my research and for taking the reins of the day-to-day running of the lab and continuously improving it. Each new member of the group has brought incredible dynamism, passion, and capabilities, and I am excited to see the next stages of research in the lab. I would like to specifically thank Jamie and Shawn for their help in preparing and collecting data for the final push of this thesis. Additionally, I would like to acknowledge the many undergraduates who I have worked with in the group, particularly Andrew, Renee, and Leila, and wish them continued success in their research and career. I also want to thank my collaborators at Emory: Sarah, Daniel, Jia, Aimin, and Qiongyi, for their close collaborations during the first few years of my PhD and for the productive outcome of our work. Thanks also to David in the IEN for his help throughout the years with all of my many X-ray issues and questions.

I would like to thank the Georgia Tech MSE staff, particularly Hope, Teresa, and Dracy, for all of their help in uncountable ways to smooth the path forward for me to focus on my work. I especially appreciate the incredible dedication Hope has for our community and for her invaluable assistance whenever I needed help or guidance.

The majority of this work was supported by the Department of Defense (DoD) through the National Defense Science and Engineering Graduate Fellowship (NDSEG) Program.

Finally, I want to thank my church community for supporting me with friendship, neighbors, food, music, and a shared life together throughout my time in Atlanta. I would not have been able to complete this work without their assistance, both physically and spiritually, and I will deeply miss this family as I continue to the next phase of my life.

TABLE OF CONTENTS

LIST OF FIGURES

LIST OF SYMBOLS AND ABBREVIATIONS

ALD	Atomic Layer Deposition
TMA	Trimethylaluminum
DEZ	Diethylzinc
XRD	X-Ray Diffraction
XRR	X-Ray Reflectivity/Reflectometry
PH-ALD	Pulsed-Heating ALD
XPS	X-Ray Photoelectron Spectroscopy
FLA	Flash-Lamp Annealing
SFG	Sum Frequency Generation (Spectroscopy)
CVD	Chemical Vapor Deposition
UI	User Interface
UX	User Experience
AFM	Atomic Force Microscopy
SIMS	Secondary Ion Mass Spectrometry
PLD	Pulsed Laser Deposition
CVD	Chemical Vapor Deposition
MBE	Molecular Beam Epitaxy
PED	Pulsed Electron-Beam Deposition
MOCVD	Metal Oxide Chemical Vapor Deposition
MOVPE	Metal Oxide Vapor Phase Epitaxy
AZO	Al-doped ZnO
TCO	Transparent Conducting Oxide

SUMMARY

Atomic Layer Deposition (ALD) is a critical thin film deposition technology with applications spanning microelectronics, solar fuels, and biological preservation due to its advantages of a wide precursor library for the majority of the periodic table, exquisite control over growth rates, and the ability to deposit at extremely low temperatures. One critical parameter in ALD growth is deposition temperature, which defines the "ALD window"—a temperature range in which ALD growth kinetics hold. Most ALD processes tend to be limited to deposition temperatures of <300 ˚C, causing ALD films to be typically amorphous as-deposited. While amorphous inorganic films are often thought to be structurally equivalent, films grown by ALD can vary significantly in mechnical, optical, thermal, and electronic properties. By changing deposition temperature from room temperature to 150 ˚C, amorphous TiO_2 films are shown to exhibit a change in density of 15% and a change in optical polarizability of 10%. These shifts in density correspond to a decrease in the thermal conductivity of TiO_2 thin films and a decrease in Ti^{3+}-based electron trap states.

High deposition temperatures are usually required to deposit crystalline films, which are typically not compatible with ALD precursors. A method called resistive pulsed-heating ALD (PH-ALD) is introduced as a strategy to circumvent the thermal limitations of ALD precursors by applying a short heat pulse to the film after low-temperature deposition cycles in the ALD process. The PH-ALD technique is used to grow epitaxial ZnO films on c-plane sapphire using the low-temperature diethylzinc-water ALD process. Epitaxial films are grown at pulse temperatures of 500 ˚C and above, and at deposition cycles:heat pulse ratios of 5:1. Furthermore, the PH-ALD process is

used for templating epitaxial growth in ZnO, with films as thin as 5 PH-ALD cycles capable of templating an epitaxial film up to 100 nm thick. Electrical and optical measurements are shown to be comparable to films grown by other physical and chemical vapor deposition techniques, indicating that the PH-ALD method may be a practical approach for the growth of complex crystalline oxide thin films. To support future workers in this field, detailed descriptions of control software, hardware, and reactor designs are provided to enable the development of ALD systems that can incorporate external sensors and controllers for advanced intelligent processing recipes.

CHAPTER 1. ATOMIC LAYER DEPOSITION

Atomic layer deposition (ALD) has exploded in popularity since it was first developed in the 1970s and 1980s. Initially starting as a tool for depositing III-V semiconductors and materials for electroluminescent displays[1-3], it has become an essential component in modern semiconductor manufacturing for its ability to deposit high-k dielectrics for processors and memory[4-9]. ALD has also shown promise in fields as diverse as batteries[10-12], biology[13], and art conservation[14] due to the technique's unparalleled ability to deposit highly conformal films at low temperatures at a scale of a few nanometers. These advantages have the driven the development of new precursors, new equipment, and new processes to continually expand the reach of ALD and ALD-like processing to make it the preeminent scalable, nanoscale thin film growth technology.

This opening chapter aims to give an overview of the fundamental theory behind ALD processing and some background into the growth of crystalline binary and multi-component oxide films by ALD. I will then discuss the background of pulsed-heating ALD and the related flash-lamp ALD concept. Finally, I will present a statement of purpose for this thesis.

1.1 ALD Fundamentals

1.1.1 *The ALD Process*

Atomic Layer Deposition (ALD) is a powerful deposition technique for growing conformal and dense thin films with sub-monolayer growth precision. ALD has been used to grow films across the bulk of the periodic table[15-16] with a range of complementary atoms or the bare element. ALD is a subset of chemical vapor deposition (CVD) in which two or

more complementary and volatile precursors are dosed into a reaction such that they are separated by time or space. These reactants are preferentially chosen such that they:

- do not self-react,
- react rapidly with a complementary compound and with the substrate of interest,
- are highly volatile,
- are all stable over some temperature window.

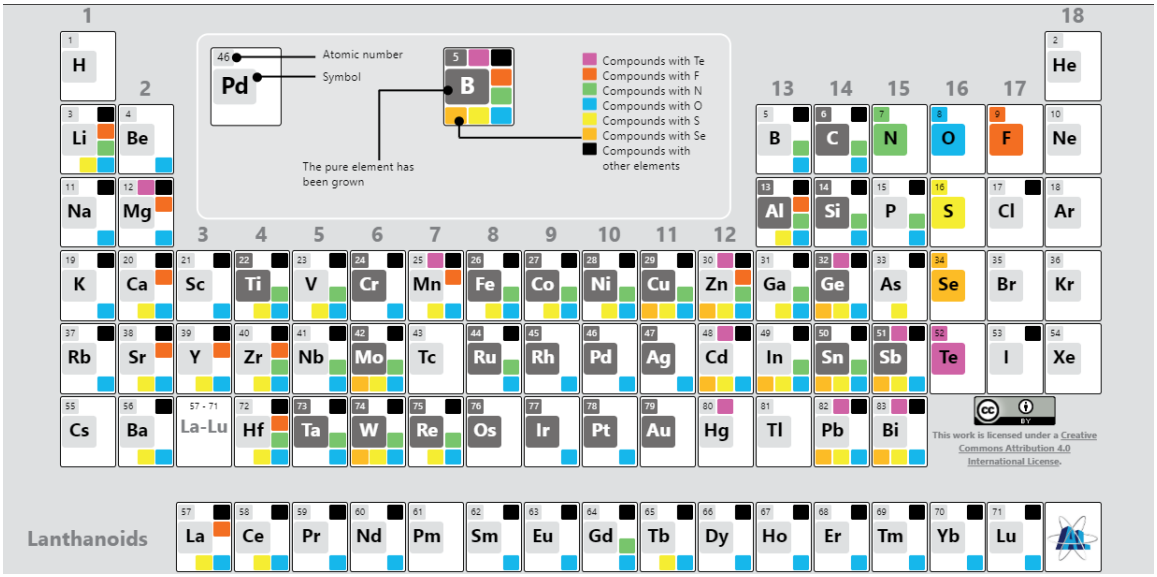

Figure 1.1. Compounds grown by ALD processing with a variety of complementary atoms.[17]

The prototypical ALD process consists of four steps, shown in Figure 1.2. First, the ALD chamber is exposed to a volatile ALD precursor, which reacts with exposed surfaces and forms a monolayer of half-reacted precursor. Second, the chamber is purged with carrier gas to remove any unreacted precursor, reaction byproducts, and any physisorbed molecules on the material surface. This purge step is often the most time-consuming step of the ALD process but is critical to maintaining the separation between precursor and co-reactant. In the third step, a co-reactant or oxidant is dosed into the chamber, where it reacts

with the half-reacted precursor molecules to regenerate the initial surface chemistry. Fourth, the co-reactant is purged out to remove excess and byproducts from the chamber to prepare the process to repeat again.

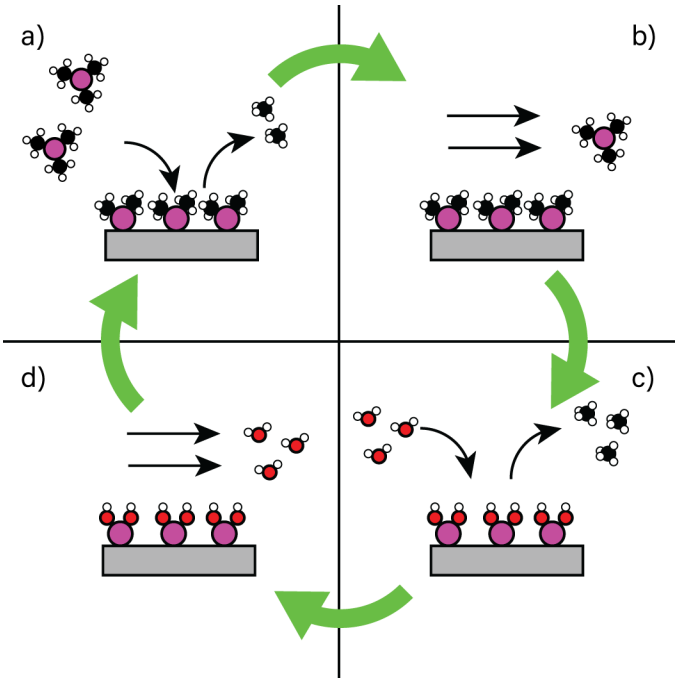

Figure 1.2. Schematic illustration of a thermal ALD process. In a), a precursor is introduced into the chamber and allowed to react with available surface sites, potentially generating side products which are purged out of the reaction zone. In step b), the chamber is then purged out of any unreacted or physisorbed precursors. In c), the co-reactant is dosed into the reaction zone, reacting with the previously deposited film and regenerating the surface sites, after which any unreacted co-reactant is purged out in step d). Dose steps are time- or space-separated from each other by the sequencing process.

1.1.2 *Precursor Selection and the ALD Window*

When developing an ALD process for a compound, the most critical step is precursor selection. There is a limited selection of precursors for any particular element that satisfy the requirements of high reactivity, volatility, and self-limiting reaction.[16, 18-21] However, most precursors typically come in the following forms: halides, alkoxides, alkylamides, cyclopentadienyls, or combinations of these ligands. Each precursor comes with a different combination of an effective thermal window, co-reactant compatibility,

growth rate, doping characteristics, and crystallinity. Examples of the varying growth rate in the TiO_2 ALD system are shown in Figure 1.3. From this figure, we see drastically changing growth-per-cycle (GPC) rates depending on precursor and deposition temperature. There are several key features we observe from this figure. The marked 0.5 Å/cycle growth rate appears to be consistent on average across a wide range of precursors, indicating that this corresponds to an "ALD monolayer"–which does necessarily correlate to a crystalline monolayer of Ti-O, as described by Puurunen for the TMA-H_2O reaction.[16] We also observe that all of the organic precursors are mostly decomposed by a deposition temperature of 400°C, with the alkoxides and alkylamides beginning to decompose around 250-300°C. Decomposition here is determined by an increase in the GPC, corresponding with the transition from a self-limited ALD-mode growth to a continuous CVD-mode growth.

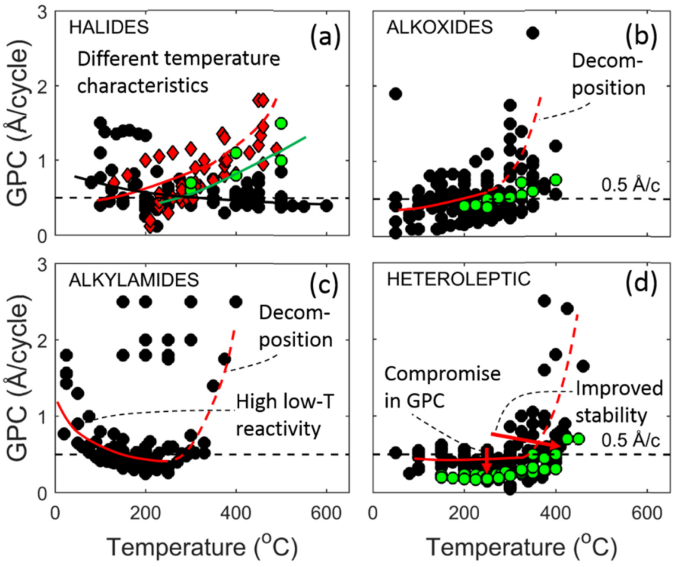

Figure 1.3. Growth rates collected from literature from a variety of TiO_2 ALD precursors. The dashed line represents the "typical" 0.05 nm/cycle growth rate. a) red diamonds, green circles, and black circles represent TiI_4^-, TiF_4^-, and $TiCl_4^-$, respectively. b) the green circles highlight thermal decomposition in $Ti(OMe)_4$. d) $CpMe_5$-containing precursors are highlighted. Reprinted with permission from *Semicond. Sci. and Technol.* 2017. 32, 093005. Copyright 2017 IOP Publishing Ltd.

The region of consistent growth rate at intermediate temperatures is generally referred to as the "ALD window." The ALD window specifically refers to the range of temperatures where we observe self-limiting, saturated growth over an arbitrary number of cycles.[16] Usually, the ALD window also corresponds to a range of temperatures where the growth rate is constant, however we can see from systems like TiO_2 that growth rate does fluctuate with temperature even though it may fulfill the ALD growth condition. The critical features in the ALD window are that only chemisorbed molecules remain on the surface after a precursor is dosed, they remain bound sufficiently long to remove all the non-chemisorbed species, and that precursors do not decompose. Outside of the ALD window, several non-ALD growth modes may occur. At temperatures below the window, precursors can physisorb or condense on the surface such that they do not have a high enough vapor pressure to be fully removed by the purge step. This results in high growth rates as a subsequent co-reactant dosing step reacts with both the chemisorbed and physisorbed molecules. Low temperatures may also make some precursors non-reactive, so they do not bind to the surface; in this case, zero or very slow growth is observed. At temperatures above the ALD window, precursors can decompose onto the surface, causing continuous CVD-like deposition and resulting in rapid growth. Another possibility is that the reactants are too energetic and desorb from the surface after initially binding, resulting in low or zero growth. Understanding these growth behaviors is critical to establishing a successful ALD process.

Saturation curves can be used to determine whether growth occurs within the ALD window. A saturation curve describes the growth rate as a function of the dose period of each ALD precursor. Several possible adsorption dynamics are shown in Figure 1.4.[16] For

example, in the TMA-H_2O reaction, saturation curves for the dose time of TMA, the dose time of H_2O are typically used to determine the ALD growth window. In the example of changing the TMA dose time, at sufficiently short dose periods the surface will not be fully saturated, resulting in sub-monolayer coverage. With increased dose time, the precursor will be allowed to fully saturate on the surface. After saturation, longer dose times should not result in a different growth rate. The same effect should be seen for the H_2O half reaction. Example saturation curves from the literature for the thermal ALD TMA-H_2O reaction at 250°C are shown in Figure 1.5.[22-23]

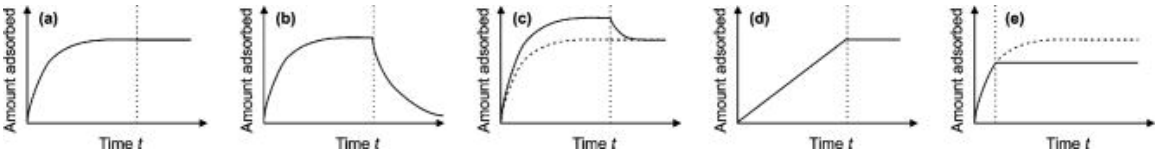

Figure 1.4. Different adsorption behaviors as a function of time: a) irreversible saturating adsorption, or self-terminating reaction, b) reversible saturating adsorption, c) combination of reversible and irreversible saturating adsorption, d) irreversible non-saturating adsorption, and e) irreversible saturating adsorption interrupted before saturation. Reprinted from *J. Appl. Phys.* 2005. 97, 121301 with the permission of AIP Publishing.

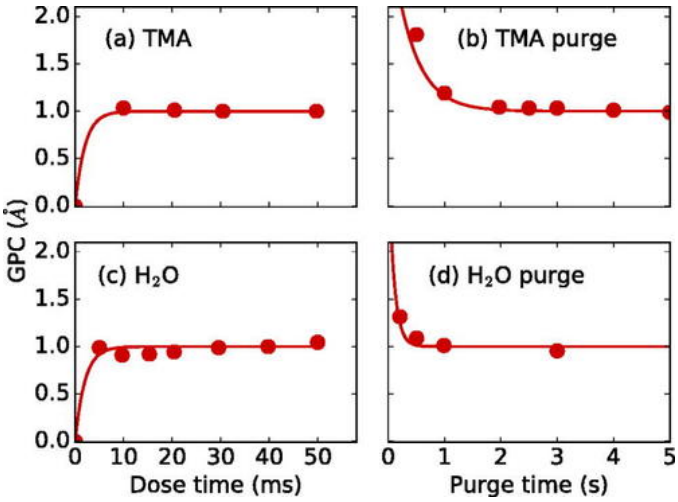

Figure 1.5. Saturation curves for thermal ALD of Al_2O_3 at 250°C. Reprinted from *J. Vac. Sci. & Technol. A* 2017. 35, 05C313 with the permission of AIP Publishing.

Vandalon and Kessels have used vibrational sum-frequency generation (SFG) spectroscopy to examine the surface coverage of -CH_3 groups on an ALD Al_2O_3 surface after the TMA and H_2O half-cycles.[22, 24] SFG spectroscopy is an advanced non-linear optical technique where a surface is illuminated by a pulsed visible and IR laser. The IR beam is modulated by the vibrational states of surface molecules, which then combines with the visible carrier beam to form a reflected sum-frequency generated beam. SFG spectroscopy contains FTIR-like data but focused at the interface, and so can accurately detect monolayers and sub-monolayers of surface coverage. SFG can also be used to detect molecular orientation due to the angular dependence of the SFG optical configuration.[25] SFG analysis showing the surface coverage of -CH_3 with saturation curves after TMA and H_2O half-cycles as a function of deposition temperature is shown in Figure 1.6. For the TMA half-reaction, we observe that the surface saturates with -CH_3 moeities after dose times of less than 50 ms, and that the surface remains saturated for longer dose times independent of temperature. In contrast, the H_2O half-reaction is strongly sensitive to temperature, not reaching full saturation until relatively high temperatures of 200°C. This effect is partially explained by a shift in the surface reaction kinetics from high to low temperature. At high temperatures, each TMA molecule binds to a single -OH site, making the Al site more reactive to the incoming H_2O molecule and creating more reaction sites. At lower temperatures, the TMA molecule instead can coordinate to two surface -OH sites, reducing the reactivity of the remaining -CH_3 ligand and reducing the total number of reactive sites. However, even though the surface does not fully saturate on the H_2O pulse at lower temperatures, self-limiting growth is still observed. In the case of the TMA-H_2O reaction, low-temperature self-limiting growth is likely caused by site-starvation where

bifunctional coordination of the TMA to the hydroxyl terminated surface consistently limits growth and prevents continuous deposition.

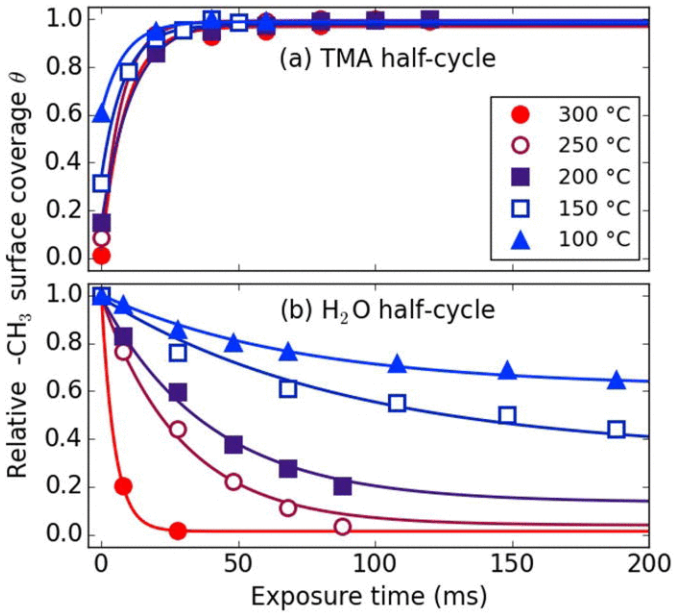

Figure 1.6. -CH_3 surface coverage θ determined from sum-frequency generation spectroscopy in the TMA-H_2O ALD system across a) the TMA half-cycle and b) the H_2O half cycle. Solid lines are fits to the data. Reprinted from *Appl. Phys. Lett.* 2016. 108, 011607 with the permission of AIP Publishing.

The dependence of growth mechanism on ALD growth temperature can have effects on film structure. Decoster *et. al.* describe how varying ALD growth temperature in Al_2O_3 thin films can have significant effects on density, with lower-temperature growth reducing the film density by up to 15% versus the highest temperature.[26] Lower-temperature films also exhibit a reduced thermal conductivity. The reduction in density from lower deposition temperatures may be explained in part by the reduced surface site density observed by the SFG studies, which also corroborates the consistent growth rate across temperatures of 0.11 nm/cycle across growth temperatures.

ALD is an extremely capable thin film growth technique that enables the precise growth of a wide range of materials; however, there are significant complexities and non-

obvious chemical behavior that are not often considered. Even in the extremely ideal TMA-H_2O reaction, the process is very sensitive to temperature, with the effect changing the degree of surface coverage, molecular coordination, and film properties. More complex molecules with different reaction kinetics can also introduce complexities with steric hindrance and ligand side reactions along with the different chemisorption conformations and reactivities observed in the TMA system.

1.2 Crystallinity in ALD Thin Films

The properties of many oxide films depend strongly upon their crystalline phase and quality. For example, the high-k dielectric material ZrO_2 has three principal polymorphs: tetragonal (t), cubic (c), and monoclinic (m) which can have very different dielectric constants, from 20 (m) to 40 (t). Likewise, HfO_2 exhibits dielectric constants from 16 (m) to 70 (t).[27-30] Accessing these high-k phases is critical for shrinking dielectric layers in microelectronics. Furthermore, orientation can also play a major role in film properties, especially with low-symmetry phases.[31]

In other CVD or PVD growth techniques, film crystallinity is controlled by the substrate temperature. Growth temperatures of >600 °C permit surface reorganization and alignment to an equilibrium crystal structure at that temperature, while orientation can be controlled by using substrates with an appropriate crystal structure and orientation. Critically, high quality control over crystallinity happens by crystallization at the monolayer scale; post-deposition anneals typically do not preserve crystal orientations or layer structures.

1.2.1 *Deposition Temperature Dependence of Crystallinity*

Crystallinity in ALD films is limited by the ALD window of precursors. As shown in Figure 1.3, most ALD precursors decompose above 300 – 400 °C, which is below the equilibrium temperature for many crystalline polymorphs. However, higher temperature precursors, particularly halides, can often be used to grow crystalline phases. In a 2013 review, Miikkulainen *et. al.* collected a comprehensive list of ALD processes used to grow crystalline phases across many of the common ALD oxide processes.[15] The growth of crystalline phases depends strongly on the ligands used as well as the precursors. For Al_2O_3, films grown on nearly every substrate using an organic precursor are amorphous, but those grown using $AlCl_3$ form hexagonal, cubic, and tetragonal films at temperatures above 600 °C. In TiO_2, the amorphous phase is the most common, but anatase films can also be grown at moderate temperatures from 150 °C to 350 °C (organics) or to 680 °C (halides). At temperatures above 400 °C, the rutile polymorph can also be detected with the halide precursors. Finally, ZnO growth is almost exclusively in the hexagonal wurtzite phase from room temperature up to 400 °C (organics) or 550 °°C (halides). These examples show that crystallinity in ALD films is not obvious, and typically is strongly dependent on the precursor, processing conditions, and substrate.

1.2.2 *Size Effects in ALD Films*

One of the key advantages of ALD is the ability to grow ultra-thin films. However, the crystallinity of ALD films can often depend strongly on the thickness of the film. At equilibrium, with a relatively "thick" film on the order of hundreds of nanometers, deposition temperature is the only factor in determining the phase of the deposited film. However, thinner films often require higher temperatures to induce crystallinity. In the $TiCl_4$-H_2O system, anatase phase growth is observed from 150-350 °C but only on films

thicker than 50 nm.[32-35] At thicknesses below 10 nm, no anatase phase is detectable by RHEED up to 210 °C, between 15-55 nm the films are polycrystalline anatase with random orientation, and at greater thicknesses the crystals develop a preferred [110] orientation normal to the substrate.[35]

ZrO_2 growth also exhibits thickness-dependent crystallization dynamics. At growth temperatures above 230 °C and thicknesses above 50 nm, the $ZrCl_4$ + H_2O process produces monoclinic phase films, but thinner films from 5-20 nm thick remain amorphous even at growth temperatures of 300 °C.[15, 36] At higher temperatures, small crystallites of monoclinic and tetragonal ZrO_2 can also form, but typically not the entire film bulk. Other workers have observed that at low thicknesses below 14 nm and growth temperatures of 300 °C, ZrO_2 grows in a tetragonal habit while above 14 nm the film is mixed tetragonal and monoclinic.[37] This behaviour also can be seen with other precursors like tetrakis(dimethylamido)zirconium (TDMAZr), which can begin to crystallize to a cubic phase at 210 °C and to a mixed monoclinic and orthorhombic phase at 350 °C.[38]

Nanolaminates are often used to control the development of specific phases in ALD films. ALD is well-suited to nanolaminate growth by using "super-cycles," or **z** repeated blocks of growing **x** layers of one compound followed by **y** layers of another, for an overall structure of $[\mathbf{A_xB_y}]_\mathbf{z}$. In the ZrO_2-Ta_2O_5-based nanolaminate system, periodic interlayers of the Ta_2O_5 promotes the formation of the tetragonal ZrO_2 phase at thicknesses of 10 to 50 nm.[4, 39-40] The preference towards the tetragonal phase of the ZrO_2 layers is driven by the high growth temperatures and templating effects from the Ta_2O_5 interlayers. However, when the Ta concentration is too high, the overall film reverts to an amorphous phase, indicating that the excess Ta suppresses crystallite nucleation. Other work in the ZrO_2-

HfO_2 system shows that the crystallinity of a ZrO_2 film deposited at elevated temperature strongly depends on the surface crystallinity.[37, 41] Both ZrO_2 and HfO_2 have the same crystal structures, but HfO_2 deposited by ALD generally is amorphous. If a seed layer of amorphous HfO_2 is first deposited, then the full nanolaminate stack becomes amorphous. However, if a seed layer of nanocrystalline ZrO_2 is deposited, then the overall stack becomes nanocrystalline. The degree of crystallinity versus amorphous domains then becomes controlled by the thickness of the nanolaminate layers, where thicker layers form larger crystalline grains.

1.2.3 *Complex Functional Oxides*

A major goal in ALD processing is the development of growth strategies for multi-component crystalline functional materials. These multicomponent oxides are critical for applications like advanced solar materials, high frequency electronic devices, and transparent conducting oxides. The ability to grow thin, highly-conformal films over complex topographies in these applications is a significant benefit for ALD over alternate deposition techniques, which are typically line-of-sight. However, ALD has typically struggled in matching the properties of films grown by techniques like MBE or PLD because of its limited control over film stoichiometry and its low deposition temperataure, limiting interlayer diffusion and crystallization during growth. Addressing these challenges is essential for expanding the utility of ALD for functional materials.[42]

One application for ALD has been in the development of conformal transparent conducting oxide (TCO) films. Doped ZnO films have been frequently explored for ALD growth[43-46] due to the easy availability and use of ZnO and dopant precursors, typically trimethyl[aluminum, indium, gallium], or TMA, TMIn, and TMGa. The standard approach

for growing multi-component oxide films like doped ZnO with ALD is to use a "super-cycle" approach, where *y* layers of a dopant compound *B* is periodically interleaved with deposition cycles of the host material *A* in a deposition pattern like $[A_xB_y]_z$, where *z* represents the total number of supercyles. The effective doping concentration can be adjusted by changing the ratio of the number of host layers *x* to dopant layers *y*. ALD-grown ZnO-based TCO films generally have higher resistivies that their PVD-deposited counterparts; for example, ALD-grown Al-doped ZnO (AZO) typically has resistivities on the order of 10^{-3} Ω cm, around one order of magnitude than the best sputtered AZO films. The higher resistivity in ALD AZO films has been attributed to polycrystallinity, random grain orientation, smaller grain sizes, and poor dopant mixing.[47-48] However, some mixing can be natively achieved in the AZO growth process as the TMA precursor has been observed to etch the growing ZnO film, promoting interlayer diffusion, particularly at higher ratios of Al:Zn. This behavior has the side effect of making the doping ratio of Zn:Al more Zn-rich compared to that expected by the rule of mixtures.[49]

A more challenging problem is the growth of ternary or higher-order multicomponent oxide compounds, such as perovskites. In principal, ALD is well suited for the growth of these multicomponent compounds because of the wide library of elements available to ALD, augmented by an explosion of new precursor compounds over the past several years with different ALD windows, reactivities, and ligand types. However, the twin problems of low deposition temperature and digital growth pose significant challenges in the development of high-performance multicomponent oxides. Perovskites specifically have been a focus of the ALD community due to their wide range of applications. The development of new precursors with high temperature ALD windows has enabled the

successful growth of many perovskite materials as it is easier to find overlapping ALD windows between different precursors, and the higher deposition temperatures promote more crystalline films.[42, 50] In other cases, the driving force for crystallization is sufficiently high to promote the solid-state reaction into a high-quality crystalline film after a post-deposition anneal. For example, high-quality $BaTiO_3$ films have been grown using a superlattice approach in which regions of partially crystalline $Ba(OH)_2$ and amorphous TiO_2 are layered together, followed by a post-deposition anneal.[51] This approach avoids a major issue with multicomponent film deposition, wherein the two precursors or solid state layers chemically interact, affecting growth dynamics such that the growth behavior may not resemble the equivalent growth in the binary system.[52] Similar work on $BaFeO_3$ has shown that films deposited by this approach on an epitaxially-compatible substrate like $SrTiO_3$ can be annealed to form an epitaxial film, pointing towards the development of high-quality crystalline ALD oxides.[53]

One of the most technologically critical multicomponent oxides is lead zirconate titanate (PZT), a highly tunable temperature-stable ferroelectric material. Several workers have reported the growth of PZT by ALD by the interleaved deposition of PbO_x, ZrO_2, and TiO_2. While ZrO_2 and TiO_2 both have well-established ALD processes, there are much fewer precursors available for PbO_x growth. Early work in PZT ALD growth used the direct liquid injection of Pb precursors through a vaporizer and deposited at 240 °C[54-55], while workers later developed an all-gas-phase process using $Pb(tmhd)_2$ with $ZrCl_4$ and $Ti(^iPr)_2(tmhd)_2$[56] followed by an all-ß-diketonate process with $Pb(tmhd)_2$, $Ti(^iPr)_2(tmhd)_2$, and $Zr(tmhd)_4$[57]. More recently, films have been grown using $Pb(Et)_4$ and the alkylamides tetrakis(ethylamido) zirconium (TEMAZr) and tetrakis(dimethylamido) titanium

(TDMAT) with O_3 as an oxidant.[58-59] In general, these films were all amorphous as deposited but crystallized to the perovskite phase after high temperature anneals between 600-950 ˚C. However, controlling the composition of the deposited and annealed PZT films is very challenging, as the different Zr and Ti precursors tend to suppress the uptake of the Pb, or otherwise disrupt or interact with the active precursor. Furthermore, the described Pb precursors do not necessarily fully self-saturate, meaning that choosing the dose and purge times are essential for modifying the Pb content, hence affecting the post-anneal crystallization and limiting the ferroelectric response.[59] The development of more performant PZT films will require precursors that have more stable ALD growth kinetics along with better ALD window overlap, such as the recently described $Pb(dmamp)_2$[60], along with a better understanding of the interlayer diffusion between the different metal components under growth and annealing.[61]

1.3 Pulsed-Heating ALD

One strategy to improving film structure in ALD films is to integrate a layer-by-layer annealing process into the growth process. Layer-by-layer *in situ* heating in ALD has been sporadically explored over the past two decades, principally as an approach to improve film densities. Layer-by-layer annealing techniques, which is called in this thesis generally by the term "pulsed-heating ALD" (PH-ALD), enhance the properties of thermal ALD films by promoting densification and driving off contaminants at the growing surface of the film. The general principal is to integrate an annealing step into the overall ALD layer-by-layer process, resulting in growth process of [**n** ALD cycles]-[heat pulse]. This approach has been successful in improving film densities beyond that capable of a bulk post-deposition anneal but suffers from long process times and complex engineering

requirements. Nevertheless, PH-ALD represents a potentially useful method to enhance film properties, access new phases, and tune film structure in ALD films.

The typical approach to improve densities in ALD thin films is to conduct a post-deposition anneal after the deposition. However, Conley *et. al.* with HfO_x[62-63] and Nabatame *et. al.* with $HfAlO_x$[6] discovered in the early 2000s that by conducting an *in situ* anneal step during the purge period after every ALD cycle, the resulting films were denser and with a lower leakage current than could be achieved by ALD followed by a post-deposition anneal alone. These anneals were conducted at a temperature of 420 °C, below the temperatures required for a post-deposition anneal but above the stable deposition temperatures for the Hf or Al precursors. These results show an *in situ* anneal captures behavior that is related to both the anneal temperature and the surface chemistry of the as-deposited ALD layer.

1.3.1 *Flash-Lamp Annealing*

A major problem with the layer-by-layer annealing approach is the significant extra time it adds to the ALD growth process. ALD is thought to be a "slow" process, taking often up to one minute per ALD cycle, which typically deposits around 0.1 nm. Heating and cooling the sample for the layer-by-layer annealing process can add significant time to the process, up to several minutes per cycle. This slowdown can make ALD nonviable for many production processes, which may need to deposit several hundred cycles. To speed up processing time, several workers have explored using flash-lamp annealing (FLA) to limit the energy delivered into the ALD film. In flash-lamp processing, a sample is irradiated with a short intense burst of light in the visible spectrum from a xenon flash lamp. The short active time of the lamp means that the total energy delivered to the sample

is limited even though the lamp power output is very high. This method allows the surface layers of the material to reach a high effective temperature while the rest of the sample and the substrate remains at the ambient processing temperature. When the lamp goes dark, the cool substrate acts as a heat sink to quickly remove the heat from the material.

In 2012, Langston *et. al.* described using a flash lamp system which used repeating pulses of 2.9 ms bursts to *in situ* anneal a growing TiO_2 film.[64] After every ALD deposition cycle, a xenon flash lamp would be flashed for several millisecond-duration pulses, reaching average temperatures from 196 °C to 559 °C with 1 flash to 40 flashes, respectively. In TiO_2, the as-deposited film remained amorphous at a deposition temperature of 160°C, but the FLA-processed film was nanocrystalline, principally in the anatase phase with some brookite component. A similar approach was taken by Henke *et. al.* to densify a growing ALD Al_2O_3 film. Henke *et. al.* used a single xenon flash of 1.8 s to heat the Al_2O_3 film grown at a low temperature of 75°C, achieving a 10% densification which could not be achieved by a post-deposition anneal at 600 °C.[65-66]

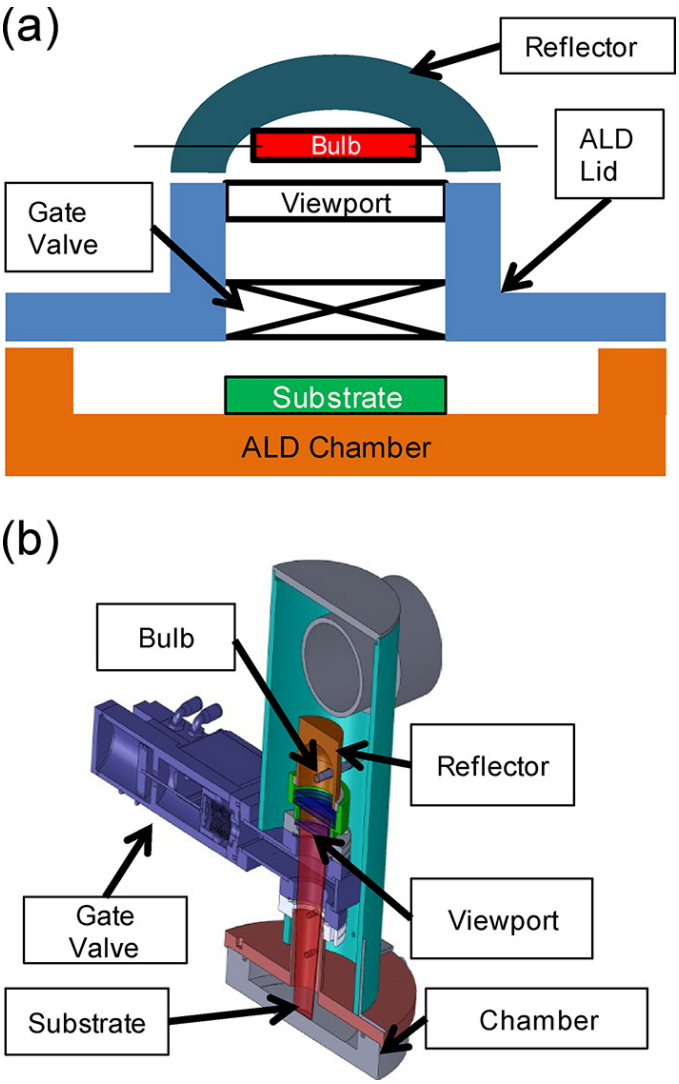

Figure 1.7. Flash-lamp annealing ALD system. Reprinted with permission from *J. Phys. Chem. C.* 2012. 116, 45, 24177-24183. Copyright 2012 American Chemical Society.

While FLA ALD systems do offer promise for depositing denser, more crystalline films, they are much more complex than typical ALD systems and require custom design and integration of the flash components. An example tool schematic from Langston *et. al.* is shown in Figure 1.7. Furthermore, it is not trivial to determine the amount of heating experienced by the growing film, as there are several factors that all influence the amount of heat transferred into the film. One issue is that different materials absorb the lamp

radiation differently, meaning that heat measurements from one material to another are not consistent. Another issue is that the temperature gradient within the film may have a different profile depending on the thermal conductivity and absorptivity of the film. A third issue is that the flash lamp system must be isolated from the ALD process environment, otherwise the optical windows will be also be coated, attenuating the lamp power and requiring frequent replacement. This means that the FLA processing must be limited to the purge phase only.

1.4 Statement of Purpose

As ALD continues to expand into new application spaces, it has become more critical to deposit functionally active films beyond the more common applications of dielectrics and barrier coatings. However, due to thermal limitations of most organic ALD precursors, most ALD films are grown at low temperatures between 100-300 ˚C, resulting in amorphous-phase films. Subsequent post-deposition anneals generally result in randomly-oriented polycrystalline films that may be in several phases instead of a specific desired phase. As a result, a significant amount of development in the ALD community has focused on identifying new precursors that can be used to grow films at higher deposition temperatures. While a number of new precursors have been developed for common elements, less-common elements have fewer well-characterized or effective precursors; also, most new precursor compounds are not easily available to use.

Many common ALD-grown films do have desirable properties even in an amorphous phase, such as Al_2O_3, TiO_2, HfO_2 and ZrO_2. However, the properties of these films can vary significantly with deposition temperature and precursor type. These differences in properties have generally been attributed to dopant effects from the different

precursor ligands, such as C, N, and Cl. However, there has been less attention focused on the effect of film structure on these properties.

ALD has also been explored for the growth of multicomponent functional oxides, but suffers from two problems. The first problem is that in a multicomponent growth process, all precursors need to have overlapping ALD windows. This constraint often limits the choices of precursors that can be used, which compounds the problem that precursors may often interact differently with a multicomponent film than in a binary growth process. The second problem is that many functional oxides require specific crystalline phases for their properties which would require growth at high temperatures above the ALD window. To solve this problem, workers typically deposit laminates of amorphous films then later anneal the film to crystallize it. However, this solution has poor control over phase, stoichiometry, and orientation.

In this thesis, I demonstrate how temperature can be used to manipulate the structure and properties of ALD oxides. First, I examine the use of deposition temperature to manipulate the structure of amorphous TiO_2, resulting in significant changes in density, optical, thermal, and electrical properties. Second, I demonstrate a strategy for independently tuning film structure using pulsed heating during the "purge" phase of an ALD cycle, effectively decoupling precursor-related growth effects from the ultimate film structure. These key objectives are given below:

- The structure and properties of amorphous ALD films can be precisely tuned using deposition temperature.
- Deposition kinetics can be decoupled from film structure by annealing during the inactive purge time during ALD.

- Layer-by-layer pulsed-heating annealing can be used to access crystalline phases inaccessible to standard thermal ALD.

I will address these goals by using common ALD chemistries to grow unconventional material structures. I will first focus on TiO_2 as a prototypical amorphous functional film, examining structure-property correlations in density, optical properties, thermal conductivity, and electrical conductivity. I will then focus on ZnO as a prototypical crystalline film, examining the critical thermal driving forces required to induce crystallinity and epitaxial growth on a highly strained lattice.

I will also provide detailed commentary on tool design from both hardware and software perspectives to support the development of future pulsed-heating ALD systems. There is a significant deficiency in the literature on the design of control systems for ALD-type systems, making it difficult for new entrants to develop custom tools with new and unique features. My contribution to the community in this way is to provide an understanding of how to design and build a low-cost PH-ALD system which can be easily integrated into other existing ALD tools. I will also provide a detailed understanding on how to design and build control software for ALD-like systems that is robust and extensible such that it can effectively control systems with complex and new capabilities.

CHAPTER 2. EXPERIMENTAL METHODS AND EQUIPMENT

In this chapter, I will describe the equipment used for the fabrication of the ALD thin films used for this thesis and provide a brief overview of the characterization tools and methods that were used.

2.1 Flow-tube Atomic Layer Deposition Reactor

2.1.1 *Reactor Design*

Most ALD processing was conducted within one of two home-built, hot-wall, flow-tube style reactors. Purified nitrogen gas (99.999%, Airgas) was continually flowed through an O_2 purifier (SAES Pure Gas) to remove any residual water and oxygen impurities. The N_2 was then split and delivered through two gas pathways, each metered using a mass flow controller (MFC) set to maintain constant flow and a chamber pressure of 1.7 Torr. Each pathway had either precursor chemicals or an oxidant, typically water, connected in a direct-port configuration. Precursors and oxidants were delivered into the flowing N_2 carrier gas stream using stainless steel, pneumatically actuated, computer controlled high-speed valves (Swagelok or Ham-Let). The gas was then introduced into the primary reaction tube through an expanding nozzle. The reaction tube was at least 36 inches to promote even mixing and laminar flow over the samples. An MKS 728B Baratron capacitance diaphragm gauge and a Pirani-enhanced convection gauge (Kurt J. Lesker Co.) were installed at the end of the reaction tube to measure process pressure and low-vacuum pressure, respectively. A sequence of Sodasorb acid-neutralizing filters and activated carbon filters (Mass-Vac) were used to treat the exhaust before exhausting to a fluorocarbon rotary vane pump. All process lines were resistively heated to 110 ˚C with heat tape controlled by external PID controllers (Omega CN7800), then wrapped with

fiberglass insulation followed by aluminum foil. The reaction tube was wrapped with high-temperature heat tape and independently controlled to reach the target deposition temperature. Reactor operation, recipe sequencing, and data collection was managed by a custom LabVIEW software system.[67]

2.1.2 *ALD Pneumatic Control Hardware*

Our primary ALD reactors are controlled used a custom relay-actuated, pneumatic control box system which interfaces with an external LabVIEW program, shown in Figure 2.1. The general design of the system takes in clean, dry compressed air and passes it through a manifold, where it is switched to external pneumatic-actuated components using banks of eight poppet-style 3- or 4-way solenoid valves (Humphrey, M153 [3-way] or M154 [4-way]). The 3-way valves are used for actuating single elements that require on/off control, while the 4-way valves are used for actuating an "exclusive or" type device, such as a bubbler with a bypass valve and the bubbler inlet valve where only one valve should always be active. The solenoid valves are themselves actuated using an electromechanical relay control board (Generation 1: OnTrak ADR2000, Generation 2: Numato 16-ch relay board) which digitally interfaces with the external control computer.

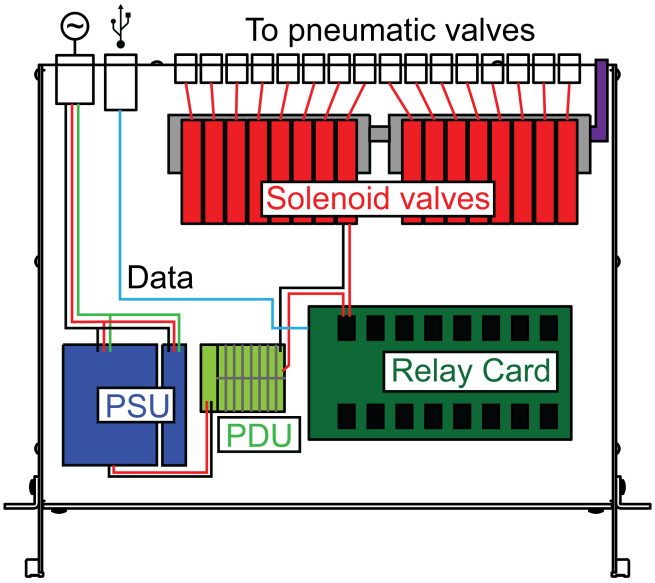

Figure 2.1. Schematic of a 16-channel Generation 2 pneumatic control box. 3- or 4-way solenoid valves (red) are connected to a manifold (grey) which is supplied with compressed air (purple). Valves connect through bulkhead connectors to external pneumatic valves or other components. Solenoid valves are electrically actuated using a digital relay card (dark green). Commands from an external computer are transmitted over USB (cyan) to the relay card, which actuates electromechanical relays powered by a 12VDC AC/DC converter power supply unit (PSU, dark blue). 24VDC from another PSU is distributed through a power distribution unit (PDU, light green) to the solenoid valve. Components are installed in a 3U rack unit chassis.

2.2 Pulsed-Heating Atomic Layer Deposition Reactor

For the pulsed-heating ALD experiments described in Chapter 5, a specialized PH-ALD reactor was designed and developed. This reactor integrates an AlN/W high-power heater controlled along with the pneumatic valves for the ALD processing, allowing for sequential pulsed heating integrated into the processing recipe. This reactor also served as a test-bed for novel control electronics and software detailed in Chapter 3. Otherwise, the reactor is substantially similar to those described in section 2.1, using a hot-wall flow-tube style reactor.

2.2.1 *Heater Design and Integration*

AlN/W heaters (Oasis Materials) were used for the heating element. The high thermal conductivity of AlN means that it can be thermal expansion matched to the tungsten heating element, allowing for high power densities for a rigid ceramic package. The heater used was approximately a 1 cm x 1 cm square with gold contact pads for attaching clip leads, shown in Figure 2.2. The resistance of the heater was 1 ohm, with the overall system resistance typically 2 ohms. For temperature monitoring during the process, a fine-gauge type-K thermocouple (Omega) was clipped to the heater stage using a stainless-steel clip. Contact to the heater was made using stainless steel clips crimped to copper wire. The thermocouple and electrical lines were passed through a single CF feedthrough.

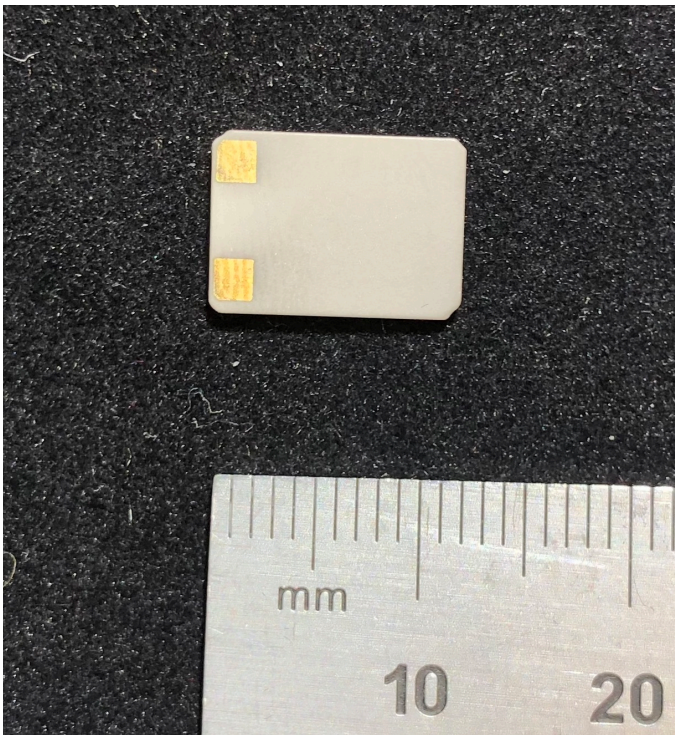

Figure 2.2. Image of the AlN/W tungsten heaters used as the high-power heating stage.

Power control was managed through a linear power supply (B&K Precision). A voltage and current limit were chosen to keep the power consumption of the heater below

its maximum power envelope of 500 W/cm^2. At low temperatures, the low resistance of the heater causes it to draw a significant amount of current which can cause the heater to break once the tungsten element heats up and increases in resistance. At higher temperatures, the relatively high resistance of the heater means that the dissipated power becomes less dominated by the current draw through the heater, so a voltage limit is used to provide an upper bound on the power consumption by the heater. More sophisticated control could be achieved using an active feedback mechanism to measure the current and voltage through the heater and adjust the voltage and current limits to fit the power maximum of the heater. Heat pulses were controlled through a home-built, general purpose ALD control software by switching a 15A DC solid state relay (Schneider Electric model 861) connected to a digital output on a control PLC (Koyo CLICK PLC).

2.2.2 *Reactor Design*

A schematic of the chamber is shown in Figure 2.3. A home-built, hot-wall style reactor was used with a 304 stainless steel cross as the reaction zone. A precursor line and an oxidant line were connected to the chamber using flexible 304 stainless steel tubing. The chamber and all process lines were wrapped in heat tape and maintained at 110 ˚C. UHP N_2 was used as the process gas with a flow rate of 60 sccm, with a chamber pressure of 1.7 Torr, measured by a convection-enhanced Pirani gauge. Precursors and oxidants were dosed into the flowing gas stream using computer-controlled pneumatic valves. An activated carbon trap was used before exhausting to a rotary vane pump.

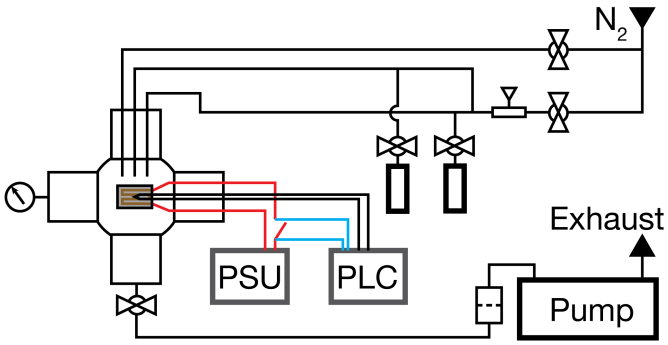

Figure 2.3. Schematic of chamber design. Ultra-high purity (99.999%) N_2 is used for purge and process gas and metered by an MFC before passing over separated precursor and oxidant lines. All pneumatic valves are controlled by the PLC and control software combination, not indicated here. Electrical power (red lines) and thermocouple signal lines (black lines) are both passed through a CF electrical feedthrough. A solid-state DC switch is controlled by the PLC to actuate the heater (blue lines).

2.2.3 *Thermal Characterization*

The thermal response of the heater is shown in Figure 2.4. The heater can reach a temperature over 600 ˚C after a 5 second heat pulse and 1000 ˚C after a 20 second pulse. While the heating time is quite fast, the cooling time in this configuration takes about three minutes to return to the ambient chamber temperature of 110 ˚C.

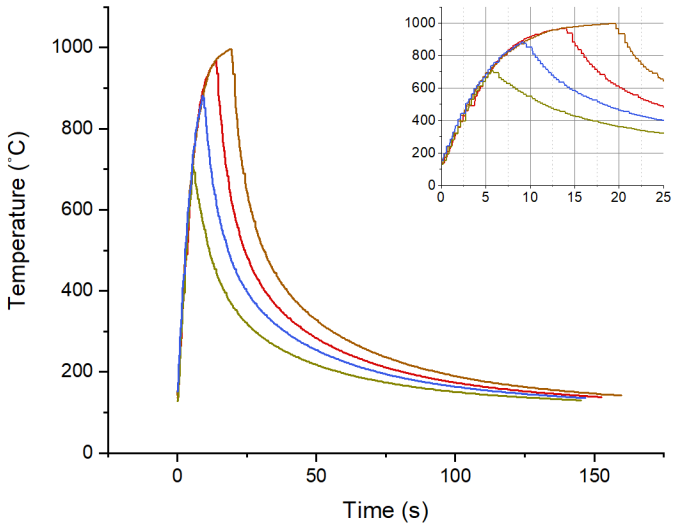

Figure 2.4. Characteristic stage temperature after a single heat pulse for pulse durations of 7 to 20 seconds. Pulse traces are taken from a series of five pulses each. (inset) Magnified view of the heating phase of a heat pulse.

To reduce the time to cool the heater to ambient temperature, the chamber was designed to blow process gas directly on the sample stage. Figure 2.5 shows the difference in cooling rate between a passively radiatively cooled sample and an actively cooled sample. Active cooling cools at twice the rate of the passive cooling, reaching 200 ˚C in two minutes versus the passive cooling, which takes over four minutes. However, further increases in gas flow do not significantly reduce the cooling rate.

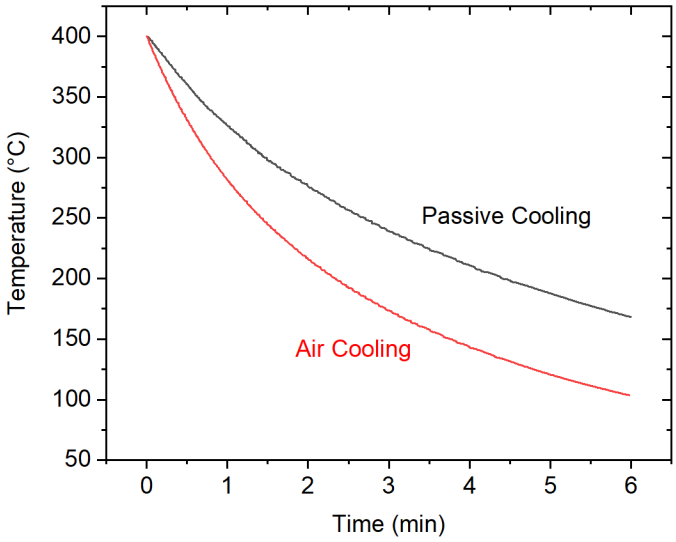

Figure 2.5. Cooling rates in vacuum versus with flowing nitrogen. Passive cooling data is taken from the chamber pumped to 35 mTorr with no flowing N_2. Active cooling is taken with 60 sccm N_2 gas flowing at 1.7 Torr chamber pressure.

Heat pulses are extremely repeatable both within a deposition run and between experiments. Figure 2.6 shows a representative selection of thermal pulse data from a deposition run of 500 PH-ALD cycles to 400 ˚C. For all heat pulses, the "on" time for each heat pulse within a run is the constant.

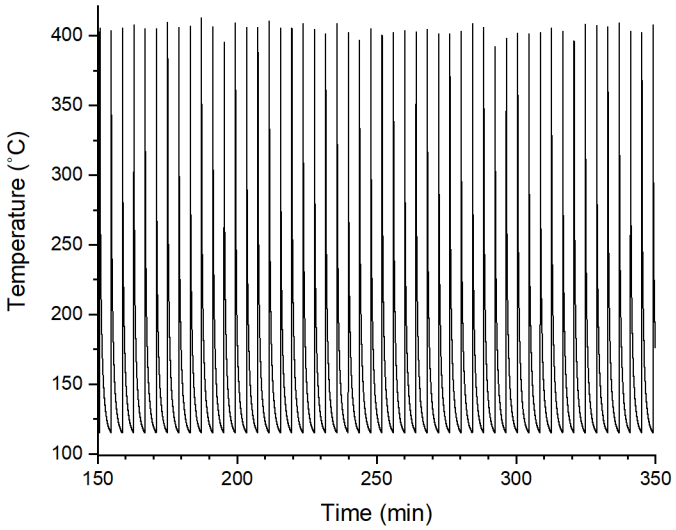

Figure 2.6. Stage temperature samples during a PH-ALD run to 400°C taken from the middle of a run.

2.2.4 *Summary and Conclusions*

High-power resistive heaters are a low-cost and easy-to-implement method to integrate pulsed-heating capability into existing or new ALD designs. Solid-state electronic controls are easily integrated into standard control systems used for pneumatic valve control, making it simple to add pulsed heating steps into a standard ALD process. Unoptimized, AlN/W heaters in this system can have heating rates of more than 100°C/s and can return to an ambient chamber temperature of 110°C within 3 minutes. Heaters are also stable within the deposition environment, enduring hundreds of heat pulses with ALD growth while retaining temperature performance. Further development may involve incorporating more sophisticated control electronics that can maximize the power delivery to the heater, especially at high temperatures. Custom-designed heaters can also be implemented that incorporate gas- or liquid-cooling to speed up the cooling process.

2.3 Characterization Tools and Techniques

A variety of thin film characterization methods were used in this thesis, particularly focusing on film structure, composition, and chemical state.

2.3.1 *Spectroscopic Ellipsometry*

Spectroscopic ellipsometry is a technique typically used to measure the optical properties and film thicknesses of transparent and semi-transparent thin films at high resolution and at low thicknesses. If the film properties are well known, ellipsometry can repeatably measure film thicknesses with a precision of 0.002 nm. Ellipsometry operates by measuring the change in optical polarization and amplitude caused by interactions and reflections within a transparent or semi-transparent film. In ellipsometry, a sample is illuminated with polarized light and collected at a known angle, where the phase shift in

the light (Δ) and the ratio of the amplitudes of the reflected polarized light (Ψ) are measured. While ellipsometry can be done in either single-wavelength or multi-wavelength (white light spectroscopic) modes, most modern ellipsometers use the spectroscopic method. From the Δ and Ψ parameters, the optical constants n and k and the film thickness can be extracted by fitting an optical model of the film stack to the ellipsometric parameters. Properties like roughness and density can also be extracted from ellipsometry.[68]

2.3.2 *Grazing Incidence X-Ray Diffraction (GIXRD)*

Grazing or glancing incidence X-ray diffraction is a variation on the more standard symmetric θ-2θ X-ray diffraction (XRD) designed to improve signal collection from thin surface films.[69] In GIXRD, the incidence X-ray source is kept at a low fixed angle α, typically just above the angle for total reflection in the target material. The detector is then swept through 2θ. By using a low fixed incidence angle, more of the surface film is illuminated by the X-ray beam, while less of the substrate is illuminated. As result, potentially weaker signals from the surface film can be observed with less influence from the substrate. Fast collection optics are typically required for this method as the total illuminated volume is often much less than in a conventional symmetric XRD scan, significantly increasing the time for data collection.

2.3.3 *X-Ray Reflectivity (XRR)*

X-ray reflectivity is a thin film characterization technique that uses specular reflections off surfaces and interfaces to measure film thicknesses and densities in a thin film stack.[70] In XRR, X-rays are reflected off the film surface and any internal interfaces in the stack. These reflected waves constructively and destructively interfere with each

other, causing a periodic oscillation in the observed intensity with reflection angle. Thickness is determined by the distance between the periodic oscillations, and the thickness of higher-order repetitive structures like laminates can also be extracted from a Fourier transform of the data. Film density can also be determined by the change in amplitude of the X-ray beam with reflection angle, as higher density films, corresponding to a higher electron density, will attenuate the X-ray beam more strongly. Since nearly all materials are X-ray transparent, XRR is an effective method for measuring the thickness and density of thin film structures that are opaque or on a non-reflective substrate.

2.3.4 *High Resolution X-Ray Diffraction (HR-XRD)*

High resolution X-ray diffraction refers to XRD techniques used to probe single-crystal or textured materials which may not be apparent from symmetric θ-2θ measurements. In these measurements, a careful alignment to the substrate is required to ensure that the X-ray source and detector are capturing diffraction from the correct crystal orientations. For the ideal signal measurements, a monochromator should be used to filter the source beam to Cu-Kα radiation and a three-bounce geometry should be used to reduce the angular width of the X-ray source beam as much as possible. Measurements are made along the θ-2θ Bragg reflection axis, by rocking the sample relative to the source beam in ω, and by rotating the crystal into an off-axis orientiation in χ (also referred to as ψ), then spinning the crystal φ. θ-2θ indicates the phases present in the sample, the ω rocking curve indicates the tilt distribution of a particular crystal, and the off-axis φ measurement indicates the rotational symmetry of the crystal. These measurements combined provide deep insight into the orientation, structure, and size of textured and epitaxial films.[71-74]

2.3.5 *Raman Spectroscopy*

Raman spectroscopy is a vibrational spectroscopy method used to evaluate film structure, stress, temperature, and bonding moeities. The technique is complementary to Fourier-transform infrared spectroscopy (FTIR). In Raman, an incident light beam is absorbed by the target material, where it either loses (Stokes shift) or gains (anti-Stokes shift) energy by interacting with the vibrational states of the material. The red- or blue-shifted light is then re-emitted from the material where it is collected and amplified. Raman shift can be used to fingerprint Raman-active crystals or to detect shifts in their vibrational system after processing.[75-77]

2.3.6 *Secondary Ion Mass Spectrometry (SIMS)*

Secondary ion mass spectrometry is a technique typically used to measure the elemental composition as a function of depth within a material, although it can be used to detect chemical states.[78] In SIMS, an ion beam is directed at the target material, generating secondary ions at the target. Heavier ions like Ga or Bi can rapidly penetrate a sample surface, generating a large flux of secondary ions with a sputter rate of tens of monolayers per second. For faster depth profiling, an assisting oxygen sputter gun can also be used to accelerate etching of the surface. Secondary ions generated by the ballistic collision are analyzed in a mass spectrometer, which are correlated to their starting location by time-of-flight. While SIMS is a destructive technique, it only damages a small area of the film (~1 mm^2), unlike other techniques like cross-sectional TEM or SEM. SIMS can also sputter at much higher rates than other methods like XPS as it uses much heavier ions and accelerating voltages.

2.3.7 *Time-Domain Thermoreflectance (TDTR)*

Time-domain thermoreflectance is a thermal measurement technique used to measure thermal conductivity in extremely thin films.[79-82] TDTR is a pump-probe type measurement, where a sample is heated with a short, high energy laser pulse, then the surface reflectivity is measured as a function of time by a low energy probe laser. TDTR is especially useful for measuring time-resolved phenomena and low-*k* materials due to the sensitivity of the thermoreflectance measurement.

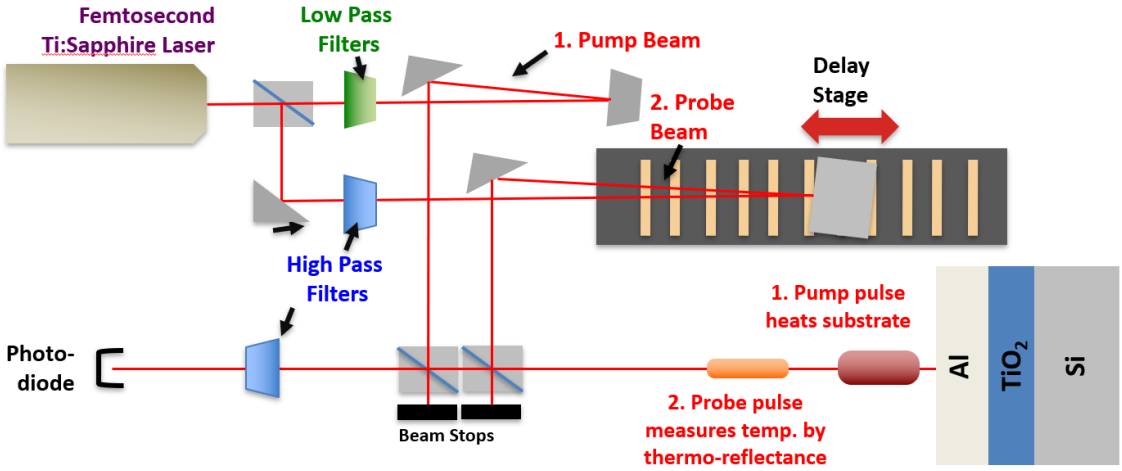

Figure 2.7. Diagram of a typical TDTR setup. Pump and probe beams are both derived from the same Ti:sapphire source laser to maintain coherence. The delay stage is used to adjust the probe delay time after the pump laser. An Al transducer is required on the surface to transmit the thermal energy into the substrate as well provide a good thermoreflectance measurement surface.

2.3.8 *Atomic Force Microscopy (AFM)*

Atomic force microscopy is a method to measure surface topography with picometer to nanometer scale resolution. AFM is a scanning probe microscopy technique where the height of an atomically sharp tip is measured as it scans across a surface. A feedback loop

coupled with a piezoelectric stage is used to maintain a constant distance from the sample surface.

CHAPTER 3. CONTROL SOFTWARE THEORY AND IMPLEMENTATION

In this chapter, I address the theory and design of control software targeted principally for ALD systems but which can be extended to any sequential deposition or "recipe"-based programmable control system. The objective of this chapter is to provide a starting point for future researchers working with custom hardware to deploy an effective yet flexible software system, along with commentary on how to engineer such software to be reliable and consistent for extended operation.

3.1 Introduction

A common application of ALD is in the growth of complex multi-level or hierarchical films. Materials with complex nano-architectures can harness novel properties that are not necessarily found in the bulk or even in a monolithic thin film. For example, techniques like molecular beam epitaxy (MBE) are capable of producing precise quantum well heterostructures when integrated with precisely sequenced mechanical shuttering action.[83] Sequential delivery of vapor-phase precursors in atomic layer deposition (ALD) permits growth of nanolaminates with various novel properties not observed in the bulk.[84] Liquid-phase layer-by-layer (LbL) deposition is similarly capable of generating nanomaterials and composites with unique properties.[85]

Most sequential processing methods focus on only two materials deposited in a simple pattern. Quantum wells, for instance, require an A-B-A schedule of deposition, while laminates of ALD-deposited materials typically repeat in a regular $(A\text{-}B)_x$ pattern. However, new research efforts in multicomponent nanocomposites, compositionally graded interfaces, or hybrid materials are emerging that require more complicated dosing

sequences.[86] Schematic diagrams of these types of structures are shown in Figure 3.1. Software tools that support these efforts will simplify implementation and accelerate the discovery of new hybrid materials.

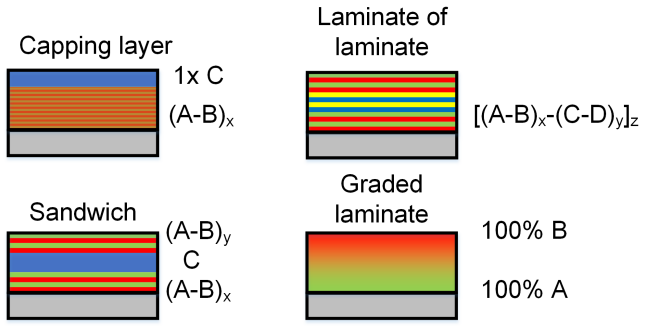

Figure 3.1. Examples of complex hetero-structures enabled by ALD. Reprinted from *J. Vac. Sci. and Technol. B* 2015. 33, 043201 with the permission of AIP Publishing.[67]

In this chapter, I will discuss the theory and implementation of the ALD control software used to operate the reactors used in this thesis. Although various forms of ALD equipment have been well documented over the past four decades, there is almost no information available to community on the design and implementation of compatible control software. This lack of information is likely in part due to the "simple" nature of ALD processing–sequence of several repeating steps—and as such does not require complex control algorithms or techniques. However, the need for more sophisticated control software has become clear as ALD processing has matured and related growth techniques have like vapor-phase infiltration (VPI)[87] have developed. I will first describe an algorithmic approach based on artificial intelligence concept called "behavior trees" that enables complex recipes with run-time decision making. I will then describe how this concept has been implemented in a) a standalone application using LabVIEW and b) a distributed microservice system using Go.

3.2 Behavior Tree-Based Control Algorithm

3.2.1 *Introduction*

In 2015, Selvaraj and Takoudis described a prototype of ALD control software capable of depositing laminates of several materials by using multiple precursor lines.[88] This article is one of the few in the literature describing the design of an ALD software control system. Their approach uses two nested "For-loops": the inner loop iterates over the valving actions required to deposit a single layer of a compound while the outer loop iterates over each different laminate. A flow chart describing the algorithm is shown in Figure 3.2. Generally, most ALD software systems use single or multiple for-loops to control the sequential valve operations. However, the disadvantage of this approach is that most naïve implementations hard-code the valve operation steps. For example, a program designed for ALD operation may have four "valve-programming" options for the precursor dose, purge, co-reactant dose, and final purge steps. However, if extra operations are needed then it becomes necessary to edit the code to add extra options. Identifying methods to write control software that can accommodate a wide variety of control options is essential for developing next-generation thin film tools.

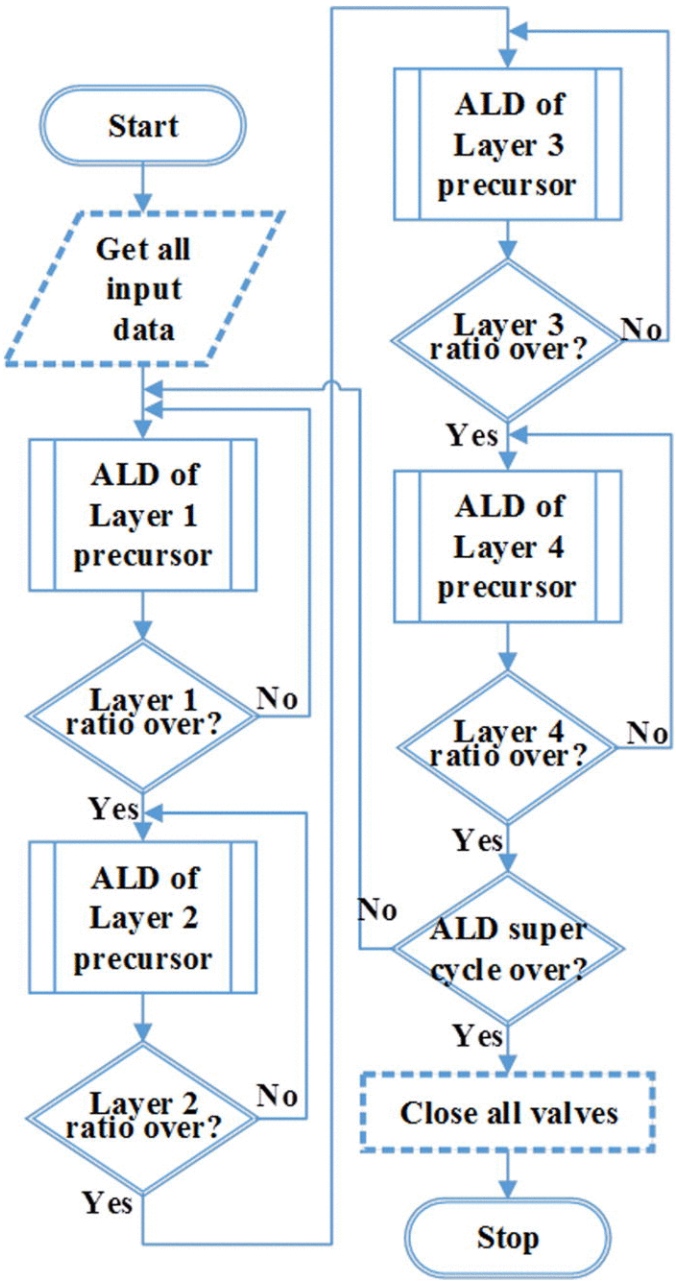

Figure 3.2. Flowchart showing a for-loop based algorithm for ALD supercycles. Additional ALD layers must be added into the core algorithm to add extra "layer" instructions into the operation. Reprinted from *J. Vac. Sci. and Technol. A* 2015. 33, 013201 with the permission of AIP Publishing.

An extensible ALD control software needs to be able to handle many complex deposition patterns without requiring the user to edit the underlying code. One approach to this problem is to model the ALD deposition recipe as a "tree" instead of a simple sequence

of steps.[89] Over the past decade, the artificial intelligence and video game communities have developed similar *behavior tree* algorithms to achieve highly flexible frameworks for structuring the potential actions of computer-controlled actors.[90] Using these techniques, the automated characters in video games have become near lifelike due to their nearly limitless decision behavior. Similar algorithmic strategies can be replicated for ALD controls applications, facilitating the growth of complex film structures and allowing for intelligent decision making based on external sensor inputs that may be non-trivial to implement using other recipe models.

3.2.2 *Loop-Based Constructs*

To illustrate the idea of sequential deposition, consider the Al_2O_3 ALD reaction. In this reaction, trimethylaluminum (TMA) and water are sequentially dosed and purged from a reactor chamber to alternately deposit "monolayers" of "aluminum" and "oxygen" on a surface. The processing sequence is composed of four steps: 1) dosing TMA, 2) purging the chamber, 3) dosing water, and 4) purging the chamber.[8] These steps are illustrated in Figure 3.3. Each step corresponds to a specified valving actuation defined by the control software. In typical sequential deposition software, this process is implemented as a loop over those four steps, with the number of iterations specified.

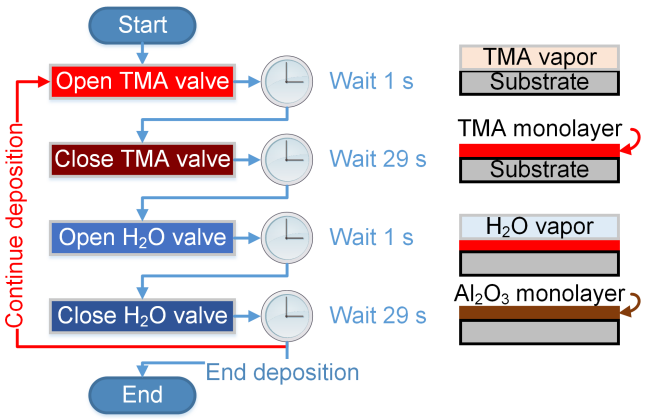

Figure 3.3. Flowchart of the model alumina ALD process from a valve control perspective. Reprinted from *J. Vac. Sci. and Technol. B* 2015. 33, 043201 with the permission of AIP Publishing.

Generally, this can be expressed as a loop over a series of discrete "command" events, which represent direct commands to hardware. For an MBE application, a command event might be the opening or closing of a molecular beam shutter, while in LbL deposition it might be the dosing of a specific precursor.

A laminate approach involves the sequential looping over two or more separate deposition sequences, where each deposition sequence consists of a series of command events. An example of this process is shown in Figure 3, where individual deposition sequences for Al_2O_3 and TiO_2 are combined to produce an Al_2O_3-TiO_2 laminate. If a single material alone is considered as a first-order process, the laminate process can be described as a second-order process. Using a simple "For-loop" architecture, the control software must be re-programmed to achieve higher order processes. In other words, a single "For-loop" is required for a single sequential deposition process like Figure 2 but two nested "For-loops" must be programmed to achieve a two-part laminate like the one shown in Figure 3.4. In the next section we introduce a tree-based architecture that easily extends such control software to an arbitrary level of complexity without re-programming.

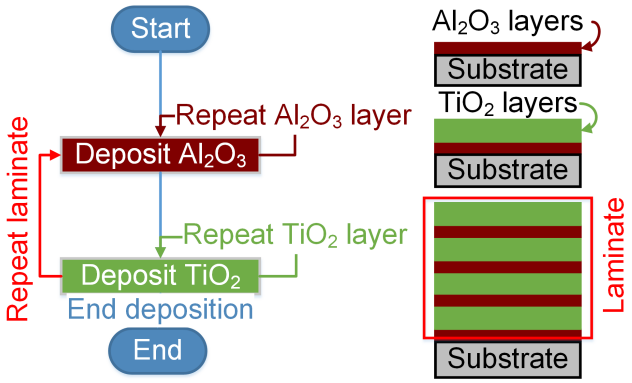

Figure 3.4. Alumina-titania deposition flowchart. The individual valving commands for the two materials are encapsulated in the "Deposit Al2O3" and "Deposit TiO2" steps. Reprinted from *J. Vac. Sci. and Technol. B* 2015. 33, 043201 with the permission of AIP Publishing.

3.2.3 *Tree-Based Program Model*

To show the correspondence between loop- and tree-based architectures, we re-implement the deposition sequence of $[(Al_2O_3)_1\text{-}(TiO_2)_3]_4$, using the scheme shown in Figure 3.5. Here, we separate the deposition sequence into discrete data storage "nodes," represented as colored boxes in Figure 4a. Each node stores parameters in the form of "<key>: value" pairs and can have zero or more children. For example, in the first level, the "Deposit Al_2O_3" node stores the parameter "<cycles>: 1" and has four child nodes. Pointers from parent to children nodes are also shown as blue lines to demonstrate the data path.

Nodes with children, such as those at the root and first level (e.g. "Laminate", "Deposit Al_2O_3", and "Deposit TiO_2"), are designated as "***control nodes,***" as they organize the control flow of the program, but do not directly send commands to hardware. Control nodes store program flow parameters; in our example we include a "<cycles>" parameter to represent the number of times a node should be revisited before completing execution.

Nodes without children (e.g. "Open <TMA> valve") are designated as "***command nodes,***" as they represent the actual commands to the hardware. These nodes store specific commands to hardware, like opening/closing valves or setting pressure/temperature parameters, and a "<duration>" parameter.

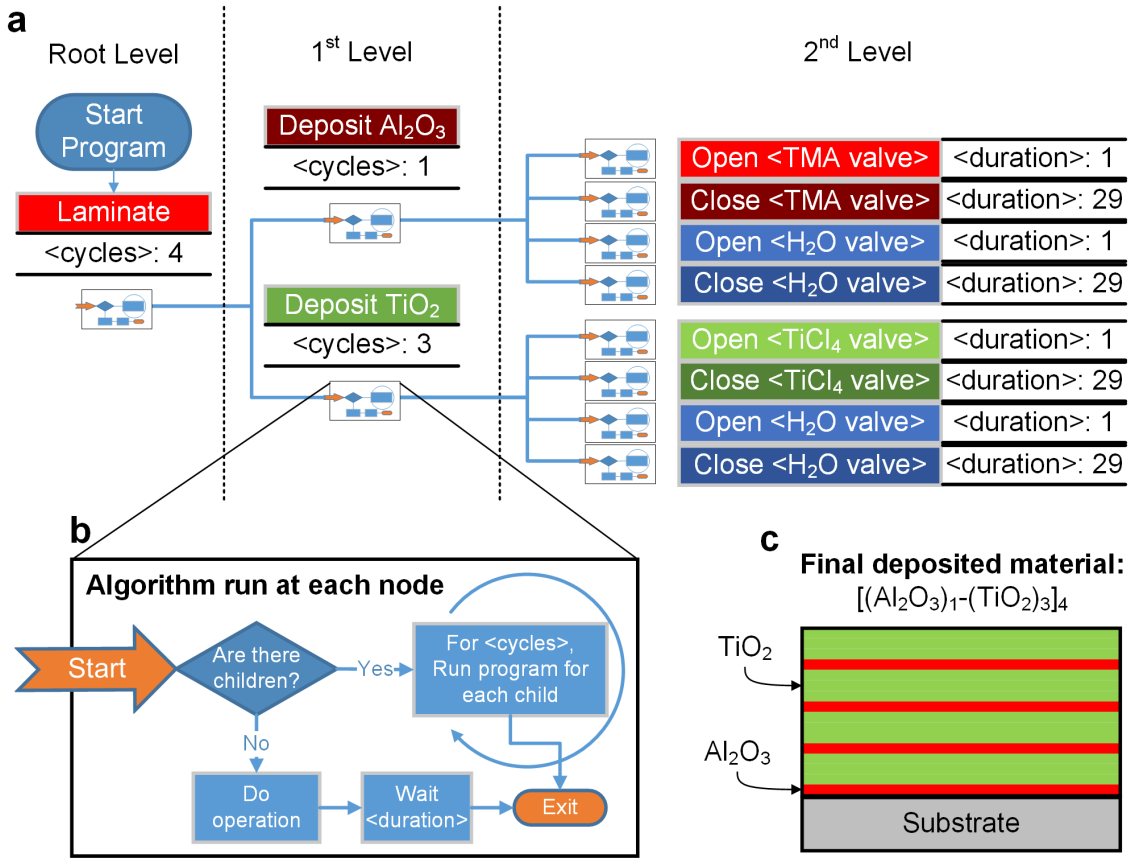

Figure 3.5. a) Expressing an alumina-titania laminate using a tree-based approach. b) Recursive algorithm independently executed for each node at each level, following parent-child relationships and proceeding from top to bottom. When there are no children, as in the 2nd Level shown here, then the operation is executed. c) Schematic of deposited laminate material. Reprinted from *J. Vac. Sci. and Technol. B* 2015. 33, 043201 with the permission of AIP Publishing.

The traversal algorithm (detailed in Figure 3.5b) operates by either recursively launching a new instance of the algorithm for each child <cycles> number of times if it is at a control node, or by executing the operation if it is at a command node. This results in

a stack of algorithm instances starting from the root control node and proceeding until a terminating command node.

Several different deposition cases can now be considered using this tree framework:

0^{th} order: A single command node, such as the "Open <TMA valve>" step in the 2nd level of Figure 4a.

1^{st} order: A control node with a set of command nodes as children, as seen for the "Deposit Al_2O_3" or "Deposit TiO_2" control nodes in Figure 3.5a.

2^{nd} order or higher: A control node with a set of control nodes as children, such as the "Laminate" control node in Figure 3.5a.

Higher-order structures, like laminates of laminates, can be produced by adding additional levels to the tree hierarchy. Additionally, the traversal algorithm treats all nodes equally, making it possible to have 0^{th} order command nodes at the same level as a 2^{nd} order control node. From a practical perspective, the deposition sequence can be modified by changing the ordering and hierarchy of the different nodes, which makes it simple to adjust the order of operations and to implement copy-paste functionality without reprogramming the software.

3.2.4 *Adding Intelligence using Behavior Trees*

The tree algorithm described in section 3.2.3 is an effective approach to modeling sequential deposition processing but is still fundamentally a deterministic and linear sequence of operations, just condensed into a compact structure. Recipes implemented by this approach cannot, as-designed, read or intelligently respond to external sensor inputs. To incorporate this capability, we return to the original behavior tree concept. In the

behavior tree model, there are two types of nodes: the "control" nodes and the "command" nodes. In the system described in 3.2.3, a single type of control node is implemented—a *for*-loop over its children. However, the behavior tree formalism describes many different types of control nodes that extend the functionality of the tree to allow for input-driven decision making and power intelligent scripting capabilities.[90-92]

Behavior trees are built on nodes that have a few special properties. Each node must always store and return one of four states: "fresh," "running," "failure," or "success". In a typical behavior tree implementation, the tree will be recursively executed starting from the root every fixed amount of time, called a "tick." Every tick, each node that is called responds with its current state, recursively propagating down the tree to eventually end at a command node such as the valve execution nodes described above.

Command nodes implement their own code to decide what states they are in. For example, a command node that sends a command to valve might have the following lifecycle:

- Begin in a "fresh" state;
- When it is run, change state to "running" and send a command to external hardware;
- After the hardware responds, change state to "success" or "failure" depending on the response.

Control nodes, in contrast, have a few predefined behaviors that dictate how they operate. The basic behavior tree formalism describes two types of control nodes: *composite nodes* and *decorator nodes*. Composite nodes can have one or more children, while a decorator node can only have one child. Generally, composite nodes direct the flow of control through the tree while a decorator node adds functionality to its child.

The standard composite nodes are called **selector** and **sequence**. Both composite nodes work by running all their children in order from left to right one by one. **Selector** nodes will run each child node until one child returns "success." **Sequence** nodes run each child until one child returns "failure." From this perspective, the ALD algorithm described above is an implementation that uses exclusively **sequence** nodes. However, to add responsive capabilities, it is usually necessary to add **selector** nodes to make it possible to choose between two branches of the tree.

Several typical decorator node types exist that add extra features to their child node. One example relevant to ALD processing is the **repeater** node, which repeats the child node a specified number of times by recursively resetting the children to the "fresh" state until the counter has been reached. Another decorator node is the **conditional** node, which tests an external condition and return "success" if true and "failure" if false. Other types can be found in the literature or developed as necessary.

With these four control node types, complex recipes that can respond to external properties can be developed. Potential example applications with this method are:

- Growing a film until a specified thickness is reached instead of for a specified number of cycles.
- Waiting for pressures to reach a specified value before continuing in a recipe.
- Executing parallel commands to e.g. a plasma or thermal source during the ALD process.
- Dynamically adjusting growth parameters during a run.

3.3 Reference Software Implementation

LabVIEW was chosen as a model implementation because of its pervasive use in academic equipment and its native tree manipulation functions. The software presented here is a stripped-down demonstration intended to highlight the core behavior for integration into existing software. In order to use this software to control a physical system, it is necessary to, at minimum, build a driver to communicate with the hardware, although convenience functions to verify the data in the tree control and allow continuous operation are also recommended. In LabVIEW, buttons can be added to the graphical user interface to enable tree manipulation in continuous operation. Source code, explanatory comments and pseudocode is available in the supplementary material from Piercy and Losego, 2015.[67]

3.3.1 *Front Panel*

A LabVIEW front panel shows the display and user-interactable components of the application. In this implementation, a native tree control component is used to write the deposition sequence. This front panel tree is shown in Figure 3.6. Parameters associated with nodes are stored in columns, such as “Cycles” or “Duration” shown here. When not running, the deposition sequencer in editable with native context menus, including the use of common interface protocols (e.g., <Ctrl>/<Option>/<Alt> + drag to copy in Windows/Mac OS X/Linux) to add, modify, move, copy, or delete nodes. When the application is run, the software begins stepping through the sequence, highlighting the active step.

In this implementation, the “Data” attribute translates to an array of Boolean values, which can represent a series of open/closed valves or similar toggle controls. These outputs are simply displayed as a series of lit/unlit circular status lights in this example code.

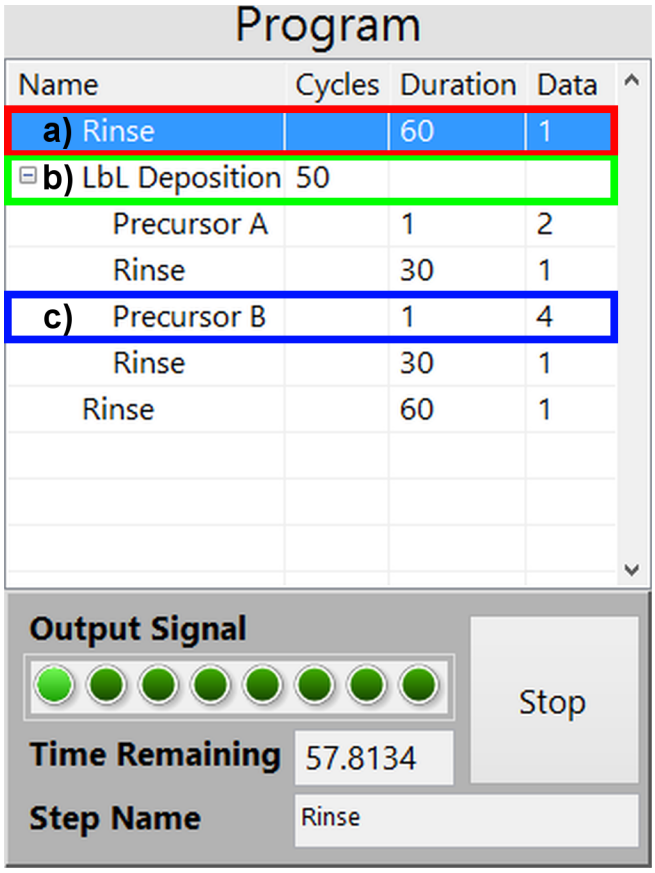

Figure 3.6. Front panel view of the application running a layer-by-layer deposition sequence. a) The currently active "command node" containing a command signal (Data) and operation time (Duration). The status window at the bottom shows the signal that is transmitted to the control hardware. b) A "control node" with children (Precursor A, Rinse, Precursor B, Rinse) and repetition information (Cycles). Here, this node repeats 50 times. c) A child "command node". Reprinted from *J. Vac. Sci. and Technol. B* 2015. 33, 043201 with the permission of AIP Publishing.

3.3.2 *Tree Traversal*

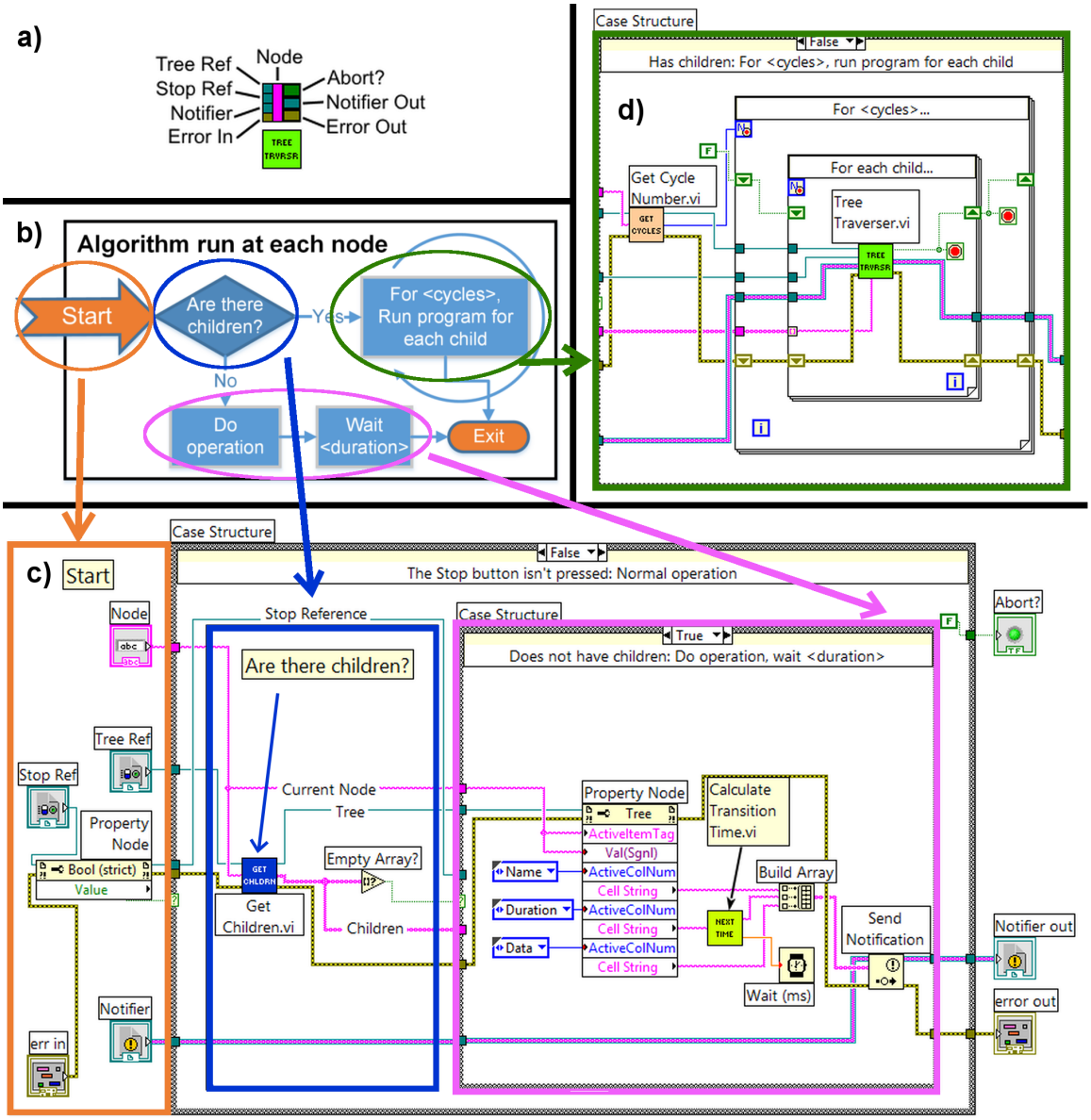

Figure 3.7. LabVIEW implementation of the tree-traversal algorithm which is implemented as a SubVI (i.e., subroutine). a) Input and outputs for the SubVI. b) Comparison of the algorithm flow chart shown previously in Figure 3.5 to the current implementation. c) Code showing the algorithm start, the check for children, and "command node" events in the algorithm. First: checks if a "Stop" button is pressed; if yes, aborts operation. Second: gets an array of all child nodes of the current node. Third: if the array of child nodes is empty (i.e., "command node" case) retrieves data for all the columns at the given node, sends the data to the display, then executes the command for <duration> seconds. If the array of child nodes is not empty, the control node case shown in d is executed; d) Code for the "control node" case, which recursively executes the "Tree Traverser" algorithm

<cycles> number of times for each child node. Reprinted from *J. Vac. Sci. and Technol. B* 2015. 33, 043201 with the permission of AIP Publishing.

In LabVIEW, the "block diagram" is analogous to code in traditional software languages. The "Tree Traverser" SubVI, shown in Figure 3.7, implements the algorithm schematically shown in Figure 3.5b. In this implementation, the algorithm first checks if the "Stop" button is pressed, and if true the program terminates. Otherwise, the algorithm generates a list of all the children of the supplied node using a helper "Get All Children" function, which returns an array of all immediate children of the provided node, or an array of all root-level nodes if no node is provided, shown in Figure 3.8. If no children are found, the SubVI enters the "command node" state, publishing the "Data" and "Name" parameters to the hardware notifier, calculating and pfublishing the timestamp of the next step, then waiting for "Duration" seconds. Otherwise, the algorithm begins two nested for-loops: the outer for the value of "Cycles" and the inner for each child node previously found. Every iteration, a new instance of the "Tree Traverser" SubVI is launched for each new child node. It is important to note that the LabVIEW software environment requires that "reentrant execution" be enabled in the VI properties to permit recursion. In this proof-of-concept implementation, the "Shared Clone Execution" option is used.

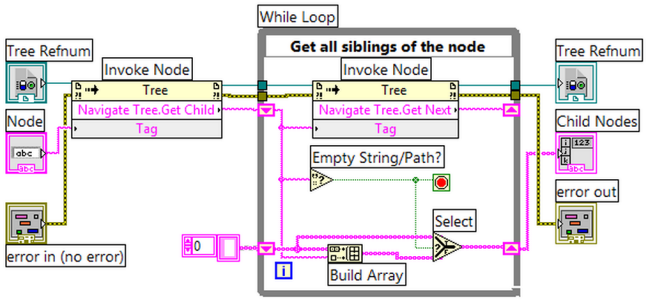

Figure 3.8. Code for the "Get Children" sub-VI which, given a starting parent node, returns an ordered array of immediate child nodes. If a parent node is not provided (Node == ""), the function will return an array of all root-level nodes. Reprinted from *J. Vac. Sci. and Technol. B* 2015. 33, 043201 with the permission of AIP Publishing.

The LabVIEW "Invoke Node" function, showcased in Figure 3.8, makes it easy to traverse a tree. The "Get Child" behavior takes in a node and returns the first child, or returns the first root-level node if nothing is provided. The "Get Next" behavior takes in a node and returns the next node at the same level and sharing a parent, or a "sibling". If there are no further siblings, "Get Next" returns an empty string. For each iteration of the shown while-loop, if the prior node is not null, the function appends the prior node to a running array of child nodes and finds and passes the next sibling to the next iteration of the loop.

3.3.3 *Example Sequences*

Existing single-component or laminate material approaches can be produced using the presented approach without needing to touch the source code. Pre- and post-deposition steps can be trivially integrated with the main deposition sequence by adding a command node at the root level. Deposition sequences can also have any number of sub-steps, making the algorithm suitable for processes that require incubation times or extra delays. This approach can also be extended to controlling separate types of hardware, such as

temperature or pressure, by adding additional parameters to the tree to designate which hardware component should be activated.

Example sequences for different potential structures facilitated by this software approach are illustrated in Figure 3.9. Here, general descriptions like “Deposit A” are used to represent the deposition sequence for an individual material, but these steps may be composed of multi-step sequences like those used in ALD or LbL deposition. By nesting simple deposition sequences under control nodes, very complex overall structures can be produced. For example, a “C”-capping layer can be added to an A-B laminate by placing a “C” control node as a sibling to the laminate control node. To deposit a graded laminate, a base A-B laminate process is copied and modified to have a smoothly changing number of A:B cycles. Finally, a higher order laminate is made by nesting simpler laminate control nodes under another parent.

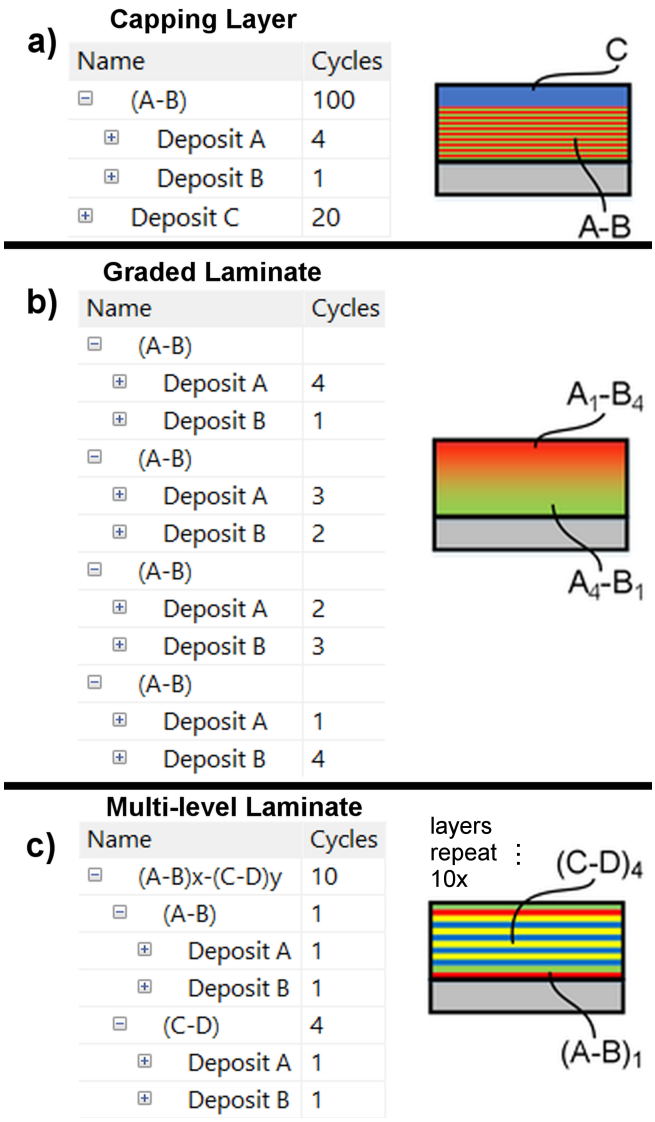

Figure 3.9. Several sample sequences are shown to illustrate potential applications of this approach a) A "capping layer" structure composed of a laminate of (A4-B1), coated with 20 cycles of C. b) Graded laminate of the form Ax-B(y-x), for y = 5 and x = 4 to 1. c) Multi-level laminate material of composition [(A-B)1-(C-D)4]10. Reprinted from *J. Vac. Sci. and Technol. B* 2015. 33, 043201 with the permission of AIP Publishing.

3.4 Practical Software Implementations

3.4.1 *Introduction*

Development of robust and scalable laboratory software is a difficult challenge, especially when interacting with non-standard hardware components and needing to

account for the integration of future equipment or analytical techniques. Many toolkits purport to simplify the development of efficient control software, but often come with hidden maintenance costs, such as operating system dependencies, limited code portability and maintainability, small user bases, and non-standard programming practices and tools. Also, many physical hardware components do not have compatible drivers or standard protocols, requiring the tool author to implement these software infrastructure components. In this chapter, I propose some implementation designs and potential pitfalls on software design and organization tailored towards laboratory control software, specifically for long-running, automated systems.

Several toolkits are specifically designed for interacting with controls systems and developing functional user interfaces. Some of the most popular are National Instruments' LabVIEW and Mathworks' SIMULINK. Both tools provide a comprehensive standard library for interfacing with physical protocols, mathematical operations, control loops, data processing and analysis, and standard programming methods. The key advantage of these techniques, however, is a drag-and-drop style interface used for both the programming interface and developing the graphical user interface (GUI). This approach makes it easy to quickly develop a prototype control software. However, quirks of the underlying programming languages often make the resulting software difficult to maintain and hard to add additional features. In this section, I will focus on LabVIEW as my example for graphical programming languages.

An example of a naïve programming practice encouraged in GUI programming toolkits is to link a program action directly to a user interface activity. This might look like sending a command to actuate a relay when a GUI button is pressed. In LabVIEW, one

might implement this with an “Event” structure linked to the button, which includes the code to send the relay-actuated command. This solution is quick to implement and easy to understand but has the hidden danger of mixing the presentation layer (the button-click event) with program logic (actuating a relay). If this approach is repeated for every button on an interface, it can become very difficult to deduce where the actual control logic is located.

3.4.2 *Local Deployment Using LabVIEW*

3.4.2.1 Architecture

Most sequential deposition tools in our laboratory are controlled with a custom LabVIEW program designed to provide a manual interface to directly operate valves and to allow users to develop and run complex sequential deposition recipes. This software is designed to use a version of a View-Controller architecture, separating the “View” presentation layer from the hardware communication conducted in the “Controller” layer. The View layer handles only the UI and communicates UI events by sending messages to one of several processes within the Controller layer. Within the Controller, independent processing loops communicate with each other using messages, retaining isolated data stores within each submodule. This approach makes it simple to add or modify functionality without affecting the rest of the software. The modules we use handle hardware control, filesystem management, recipe control, and logging, illustrated in Figure 3.10.

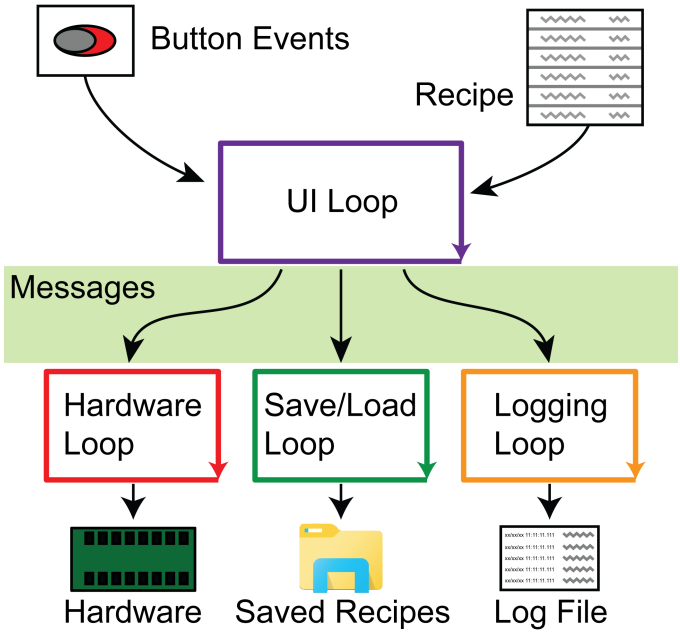

Figure 3.10. Schematic overview of the code architecture for the LabVIEW-implemented ALD control code. "Loops" are parallel *while*-loops which run continuously for the life of the program. "Messages" are objects containing a string and a payload which can be interpreted by the different loops.

A typical process flow begins with a user action, such as choosing to manually actuate a valve. The user presses a button on the UI, which triggers an event within the UI control loop. This event packages a message saying "button pressed" with data indicating the new button state, then sends this message to the hardware control loop. When the message is received in the hardware loop, it routes the "button pressed" message to a function where it parses the button data, sends a command to the external hardware, and waits for a confirmation response. Once a response is received, the hardware loop packages a message for the UI loop to update the displayed button state with the correct button data determined from the hardware response. Using this approach, it is easy to modify the hardware interaction component, such as by incorporating a log event or changing the hardware driver if a hardware upgrade is installed, without affecting the UI experience.

3.4.2.2 Hardware Selection and Interaction

It is often a major challenge to select and implement effective hardware-software interfaces due to the explosion of industrial communication standards, non-standard protocols, expensive components, and poor or limited documentation. Common options are to have a remote relay board controlled by transistor-transistor logic (TTL) or serial connections, a data acquisition (DAQ) unit, which can provide electrical isolation and normalization but does not conduct any processing, a programmable logic controller (PLC) which can autonomously perform basic automation tasks, or a full industrial computer or programmable automation controller (PAC). For this local system, we elected to use a remote relay board, meaning all controls are driven directly from the PC running the control software. This approach has the advantage of being able to simply control components at low cost, since there are no special protocols or programming libraries that need to be integrated into the code. However, it is more difficult to upgrade or replace hardware with a different version as the control commands are non-standard and would need to be updated. Also, extra external hardware components must be directly connected to the PC and use have their own driver components, which can make it challenging to add extra components in the future.

3.4.2.3 Performance and UX Improvements

To achieve higher reliability and timing consistency in the LabVIEW environment, some changes to the algorithm described in section 3.2.3 are deployed. In LabVIEW, operations that interact with the front panel have a significant performance penalty, and so using the native tree operations included with the “Tree” widget to perform real-time control lead to unpredictable timing issues. The solution used in this implementation is to

pre-compute the recipe to generate an unrolled sequence of steps shown in Figure 3.11, which are then iterated over in a loop. Doing so moves the execution environment away from the front panel reducing the variance in the timing execution to below 100 µs per operation.

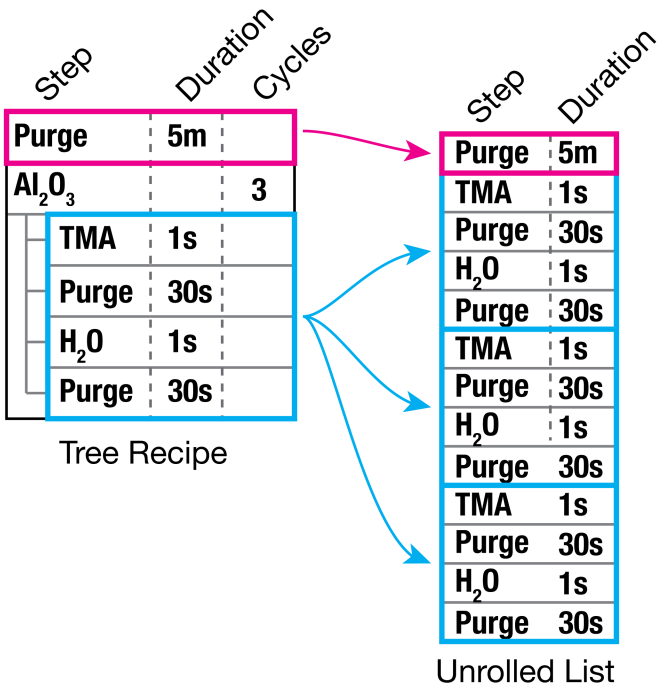

Figure 3.11. Illustration of the tree unrolling process. Control nodes, like the Al_2O_3 node on the left, are recursively traversed to generate a list of the command nodes that will be executed (right).

To protect against lost messages to the hardware, messages are continuously transmitted so that if any one message is lost then another one will be sent on the following program cycle. This is implemented by having two separate control loops in the hardware loop system: the program execution loop and the hardware communications loop. In the program execution loop, the software compares the current system time with the time that that the next program step should execute, then updates a "notifier", a type of shared variable, with the correct signal to be sent to the hardware. In parallel, the hardware

communication loop reads the most recent value from the notifier object, then transmits that value to the external control card. Using this approach, the most up-to-date message is sent to the controller within microseconds of the expected time and is continuously broadcast in case of a lost message.

To improve the user experience (UX), the control algorithm is changed to use a timestamp-comparison operation instead of a simple "Wait" function. Every program cycle, the current timestamp is compared with the timestamp of the most recent program step. If the current timestamp is greater than that of the previous step plus the step duration, the step counter is advanced, and the next step is executed. This approach means that the code is never blocked and can be responsive to input from other parts of the program, such as the UI loop. Pseudocode for this algorithm is shown below.

```
# program_state: MANUAL or AUTOMATIC
# program: a list of step data and durations
# current_step: the current step in program
# last_time: the timestamp of the previous step

last_time = getCurrentTimestamp()
current_step = 0

while true:
      message = checkInboundMessages()
      if message == "abort":
            program_state = MANUAL

      if program_state == AUTOMATIC:
            step = program[current_step]
            current_time == getCurrentTimestamp()
            if (last_time + step.duration >= current_time):
                  # quit if the program is done
                  if len(program) == current_step:
                        program_state = MANUAL

                  # advance to the next step
                  else:
            current_step += 1
```

```
            last_time = current_time

# send the step data to the hardware control loop
updateHardwareNotifier(step.data)
```

3.4.3 *Distributed Deployment Using Internet-of-Things Components*

A major disadvantage of the LabVIEW-based system that it must run on a Windows operating system to use most available libraries and drivers. Continuous operation means that it is difficult to apply updates to the operating system without interrupting ongoing processes. Most of the direct hardware control operations are extremely lightweight and do not need the capabilities of the full LabVIEW systems to run effectively. With the advent of modern single-board computers like the Raspberry Pi, full-featured operating systems can be deployed on small devices without the overhead and complexity of a Windows and LabVIEW-based stack. Modularizing the control code also makes it easy to maintain and update control algorithms and the user interface code.

The major features for modularizing the code are the separation of the UI into a web browser interface, a machine area network that allows communication between the deposition system and network-based sensors, and the use of a PLC or similar industrial computer that can interface directly with physical components. This approach uses standard internet and inter-machine communications protocols, making it possible to communicate with and control other components without needing to develop specialized drivers. A schematic diagram of how this system works is shown in Figure 3.12.

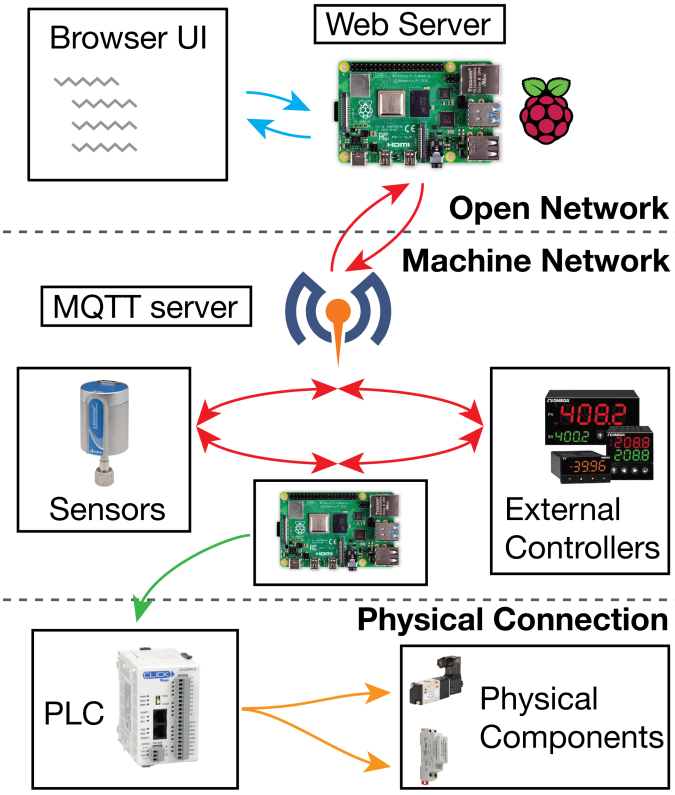

Figure 3.12. Illustration of a modular distributed controller system using standard communications protocols. The UI (top) is built using browser-based technologies, which transmits recipe data to the web server, which in turn transmits the recipe to a machine area network using the MQTT protocol (middle). Other MQTT-aware systems can be integrated to either receive or transmit data on the MQTT network. The hardware controller reads and executes the program described by the recipe, sending commands over Modbus or similar protocol to an attached PLC (bottom), which translates the commands to physical outputs to actuate external components.

CHAPTER 4. TEMPERATURE DEPENDENCE OF FILM STRUCTURE AND PROPERTIES IN LOW-TEMPERATURE ALD TiO_2

In this chapter, I describe work done to understand the structure-processing-property relationships in amorphous TiO_2 films grown by low-temperature ALD. First, I focus on structural properties, then I examine the thermal and electronic properties of this technologically critical material. The work described in this chapter is described in the following publications:

- **Piercy, B. D.**, Leng, Collen Z., Losego, Mark. D. *J. Vac. Sci. and Technol. A.* **35**, 03E107 (2017);
- Decoster, M. E., Meyer, K. E., Piercy, B. D., *et. al. Thin Solid Films.* **650**, 71-77 (2018);
- Nunez, P., Richter, M. H., **Piercy, B. D.**, *et. al. J. Phys. Chem. C.* **123**, 33, 20116-20129 (2019).

4.1 Introduction

Titanium dioxide is a common thin film material because of its ease of deposition[15], useful optical properties[32, 93-97], electronic applications[98-100], bio-compatibility[13], and (photo-)electrochemical activity[96, 100-110]. TiO_2 thin films have been grown by a variety of physical and chemical vapor deposition methods.[7, 32-33, 35, 96, 111-115] While significant effort has been spent examining the growth and properties of crystalline TiO_2 thin films, fewer studies have examined the fundamental structure and properties of amorphous TiO_2.

The growth of TiO_2 by ALD has been extensively explored due to the wide availability of convenient precursors, principally $TiCl_4$, $Ti(OCHMe_2)_4$ (titanium tetraisoproposide, TTIP), and $Ti(NMe_2)_4$ (tetrakis(dimethylamido)titanium, TDMAT).[20] ALD-grown TiO_2 exhibits unique charge transport properties compared to TiO_2 grown by

other techniques. In photoelectrochemical configurations, ALD-TiO_2 has been observed to be electrically "leaky", permitting hole transport over 50 nm, even though the film is nominally insulating.[98-100, 108, 116] ALD-TiO_2 has also been used as a stabilization layer for electrochemical and photocatalytic molecular sensitizer for its ability to transport electrons between the substrate and sensitizer without acting as a tunnel barrier.[101, 117-120] We have also observed this effect in inorganic systems like polyoxometalates[121] and perovskite quantum dots.[122] The films used in these applications are overwhelmingly grown at low temperatures and are therefore described as being amorphous; understanding the exact nature of the film structure is therefore critical for understanding the unique properties of ALD-TiO_2.

Amorphous materials are useful because of their homogeneity. The lack of crystalline grain boundaries usually reduces electrical leakage in dielectric applications[98, 123] and eliminates optical scattering.[93] However, despite being non-crystalline, the structure—and hence the properties—of amorphous thin films can vary significantly with deposition conditions. For example, Al_2O_3 thin films grown by ALD over a range of 50-250 °C remain amorphous but have densities ranging from 2.67 g cm^{-3} to 3.07 g cm^{-3} and thermal conductivities varying from 1.2 W $m^{-1}K^{-1}$ to 1.7 W $m^{-1}K^{-1}$.[124] TiO_2 thin films grown in a similar temperature window have been shown to vary in refractive index, and indirectly density, with both film thickness[125] and growth temperature[126], with important practical effects on electrical and physical transport behaviors. Previous reports have noted unique behaviors in this system at growth temperatures above 150 ˚C, such as thickness-dependent crystallization transitions[34, 125] and variations in film density from 150-250 ˚C. While other techniques, notably RF or reactive sputtering and reactive evaporation, are

capable of producing films with varying densities[114], ALD provides a sensitivity and replicability that makes it an ideal technique for probing the fundamental structure and properties of many amorphous thin film materials.

In this chapter, I first present the structural, physical, and optical properties of amorphous ALD TiO_2 films grown using the $TiCl_4$-H_2O chemistry as function measured as a function of deposition temperature and thickness. Key physical properties like the density of amorphous TiO_2 thin film density at growth temperatures below 100°C is presented, which is used to extend a density-refractive index relationship previously measured in plasma-enhanced chemical vapor deposition (PECVD) TiO_2 films to the ALD-TiO_2 system.[114] The optical polarizability of TiO_2 is calculated as a function of density and compared to measurements for other amorphous thin films previously reported.

I then discuss two collaborative studies based on these $TiCl_4$-H_2O films. The first study[127] is targeted towards understanding how growth temperature affects the thermal conductivity in amorphous TiO_2. One potential route towards realizing ultra-low thermal conductivity is through low-density amorphous films. Prior work with ALD-grown Al_2O_3 has shown that lower growth temperatures and density results in films with reduced thermal conductivity, in accordance with a differential effective medium model. To validate whether the differential effective medium model is generally applicable to ALD-grown amorphous films, we conducted thermal conductivity measurements using time-domain thermoreflectance on TiO_2 films grown at different temperatures and different thicknesses. This work is critical for cataloguing the thermal properties of nanoscale metal oxides for the future development of thermally insulating materials.

The second study[128] examines the electronic transport properties in amorphous ALD TiO_2 as a function of precursor type and deposition temperature. The hole-conducting property of ALD-grown amorphous TiO_2 has been promising for enabling Si-based photocatalytic reactors when coupled with metal catalysts in a p^+-Si|a-TiO_2|Ni device. In this system, the TiO_2 layer protects the Si from direct contact with a water environment, preventing photocorrosion of the Si absorber, while still permitting hole transport to the Ni catalyst layer. However, the cause of this hole-transport property is still poorly understood. To clarify the mechanism of hole transport in ALD a-TiO_2, different TiO_2 precursors were used to identify the influence of possibly dopant elements, while different growth temperatures were used to determine the effect of film density.

4.2 Density and Optical Properties of Low-Temperature ALD Films

4.2.1 *ALD Growth and Characterization*

TiO_2 samples were grown on n-type Si (100) substrates using a home-built hot-wall, flow-tube style reactor (§2.1). Silicon surfaces were initially cleaned using a 5-minute microwave air plasma treatment (Harrick Plasma). $TiCl_4$ was used as received as the precursors for TiO_2 (Strem, 99%) with deionized H_2O used as the oxidant. All precursors were kept at room temperature and were alternately dosed into the reaction chamber using time-sequenced solenoid valves.

TiO_2 growth was done in two stages to optimize the growth conditions at low temperature. Initially, TiO_2 films were deposited using 1000 cycles across the temperature range of 38-150 ˚C to determine growth rates (Figure 4.1). Subsequently, a set of films were grown across the temperature range with target thicknesses of 50 nm (inset of Figure 4.1) and a set of films with target thicknesses of 10, 20, 30, 40, and 50 nm. In order to

maintain growth rates within the canonical "ALD window" of 0.05-0.07 nm/cycle for $TiCl_4$-H_2O growth, longer purge times were used at lower growth temperatures.

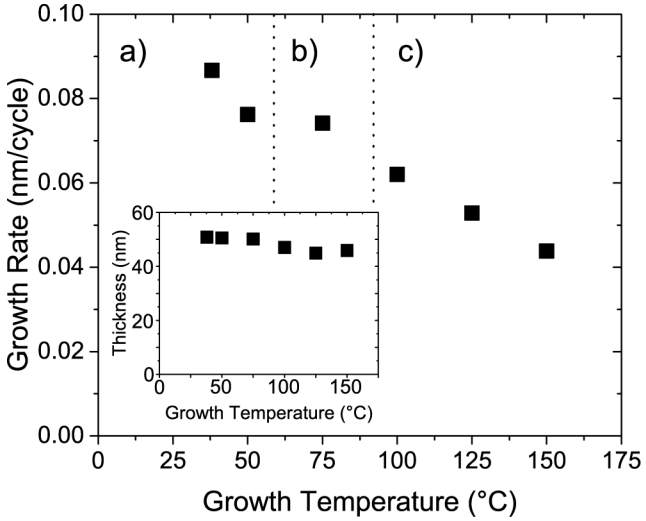

Figure 4.1. Three different dose/purge sequences were used for ALD-type growth. Dose/purge times are given as t1/t2/t3/t4 where t1 and t3 are dose times of TiCl4 and H2O, respectively, and t2 and t4 are purge times, all in seconds. The following sequences were used: a) .5/45/.1/30, b) 5/60/.1/45, and c) .5/90/.1/45. (inset) Film thicknesses between 45-50 nm, measured by ellipsometry. Reprinted from *J. Vac. Sci. and Technol. A* 2017. 35, 03E107 with the permission of AIP Publishing.

Spectroscopic ellipsometry (alpha-SE, J.A. Woollam Co.) was used to determine film thickness and optical refractive index. Measurements were collected at a fixed angle (70°) using 380 – 900 nm light. Data were fit to a Cauchy model using the included CompleteEASE software.

A theta-theta diffractometer (PANalytical Empyrean) was used for X-ray reflectometry (XRR) and grazing incidence X-ray diffraction (GIXRD). For XRR, a Bragg-Brentano primary optic was used with the following optics to parallelize the X-ray beam: a 0.04 radian Soller slit, a 4 mm mask, a 1/16° anti-scatter slit, and a 1/8° divergence slit on the incident side and a 1/16° A-S slit, a 0.04 rad Soller slit, and a PixCEL3D area detector set to line mode with only the center 3 channels active on the detection side.

PANalytical Reflectivity software was used to determine film thicknesses and density. For GIXRD, measurements were collected at an incidence angle of 1° to the surface plane with 480 s of collection time. GIXRD data was background subtracted to normalize the amorphous background.

Raman spectroscopy (inVia, Renishaw) was used as a complementary surface-sensitive method to GIXRD to detect the presence of the anatase phase. A 488 nm Ar+ laser was used with 30 s of collection time per sample. Time-of-flight secondary ion mass spectrometry (ToF-SIMS, ION-TOF) was used to probe the elemental composition of the TiO_2 samples using a Cs+ ion beam with a 2 kV accelerating voltage.

4.2.2 *Results and Discussion*

4.2.2.1 Structural Characterization

The crystalline structure of the ALD-grown TiO_2 thin films included in this study was probed with GIXRD and Raman spectroscopy. Figure 4.3 shows GIXRD data as a function of growth temperature. There is no appearance of any crystalline peaks below a growth temperature of 150 °C. This result is consistent with previous work by Aarik *et al.*[33-34, 77], who found that TiO_2 grown by the $TiCl_4$-H_2O process does not begin to crystallize until a growth temperature of approximately 150 °C. These authors also found a critical thickness of around 15 nm to initialize crystallization. This behavior is corroborated by work showing that films grown at temperatures even up to 300 °C remain amorphous under a critical growth thickness.[125] Therefore, we attribute the low intensity diffraction peak observed here to small grain size and low film thickness (50 nm compared to the 300 nm probed by Aarik *et al.*).

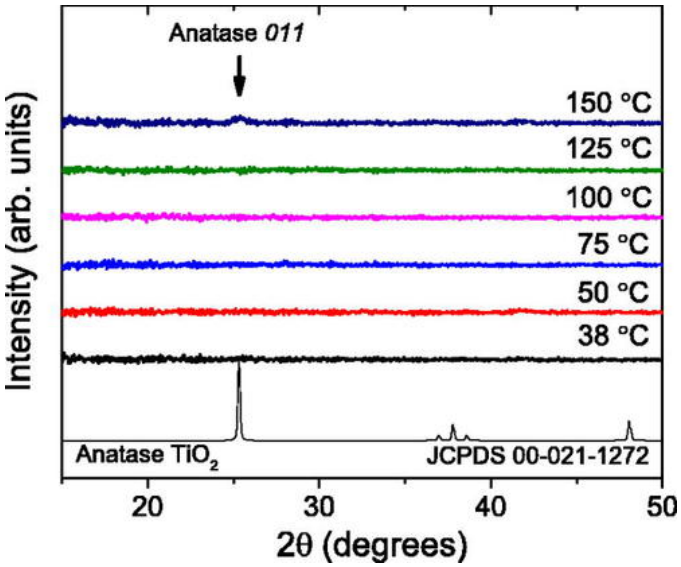

Figure 4.2. GIXRD data for TiO_2 samples grown at 38–150 °C. Spectra are background subtracted. Diffractograms are offset for clarity along with the TiO_2 reference spectrum.[129] Reprinted from *J. Vac. Sci. and Technol. A* 2017. 35, 03E107 with the permission of AIP Publishing.

The films were further investigated with Raman spectroscopy, shown in Figure 4.3, which was used to confirm the presence of the anatase polymorph. Anatase is well known to have a strong Raman scattering signal around 144 cm^{-1}.[75-77, 96] Raman excitations consistent with the anatase phase are only detectable at a growth temperature of 150 °C, consistent with previous reports.[77, 125]

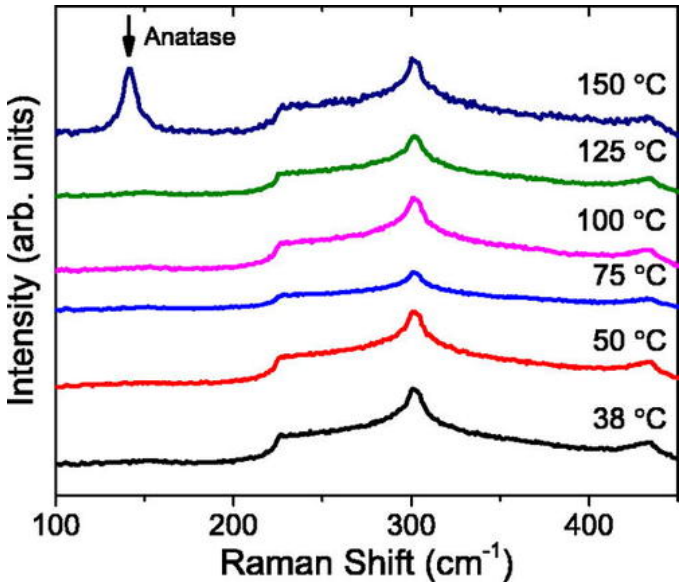

Figure 4.3. Raman scattering spectra showing the appearance of the 144 cm_{-1} anatase Raman peak at 150 °C growth temperature. Spectra are offset for clarity. Reprinted from *J. Vac. Sci. and Technol. A* 2017. 35, 03E107 with the permission of AIP Publishing.

XRR and optical ellipsometry were used to measure the mass density of the TiO_2 thin films. Mass density was computed from a fit of the critical angle of the XRR data (see inset of Figure 4) using a single layer model of TiO_2 on a Si substrate. The optical refractive index was computed from ellipsometric measurements, shown in Figure 4.4. Both XRR and ellipsometry show an increasing trend with growth temperature over the temperature range studied. Increasing refractive index with growth temperature has been observed in TiO_2 ALD in both the tetrakis-(dimethylamido) titanium (TDMAT)[130] and in the titanium tetraisopropoxide (TTIP)[125] systems. This behavior also matches the result observed in sputtered amorphous TiO_2 by Ottermann and Bange[114], who described the correlation between density and refractive index in Equation 4.1, where ρ is the mass density and η the refractive index (measured at 550 nm).

Equation 4.1. $\rho = 2.83\hat{n} - 3.27$

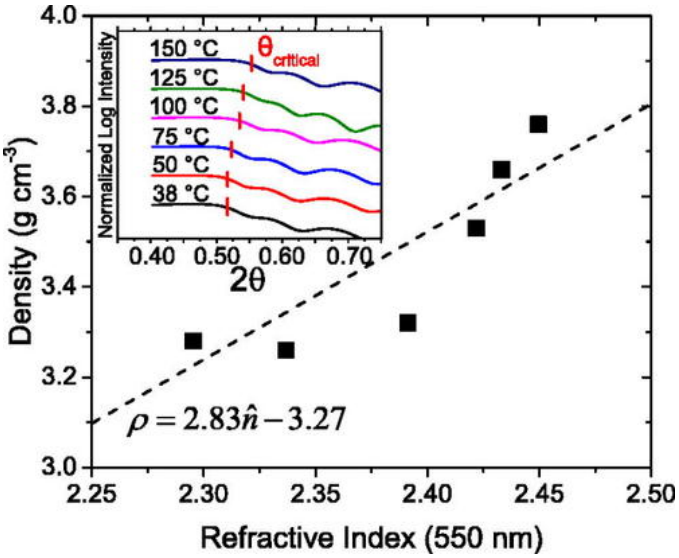

Figure 4.4. XRR-calculated density vs optical refractive index measured by ellipsometry. The dashed line represents the correlation in Equation 4.1. Error bars are less than the marker size. (Inset) XRR spectra at the critical angle. $\theta_{critical}$ markers are placed at the inflection point of the first XRR falloff. Reprinted from *J. Vac. Sci. and Technol. A* 2017. 35, 03E107 with the permission of AIP Publishing.

Using this correlation, mass densities were calculated directly from the refractive index, shown in Figure 4.5. At T > 100 °C, XRR and optical measurements of density agree well but tend to diverge at lower temperatures.

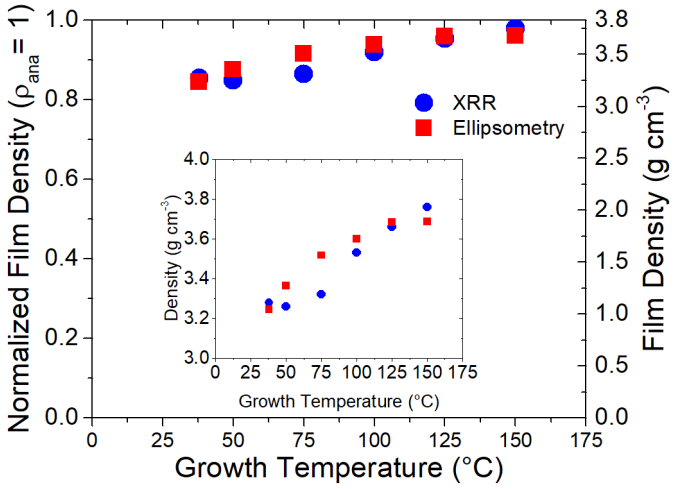

Figure 4.5. Film densities measured by XRR and ellipsometry. (Inset) Magnified view of density measurements. Reprinted from *J. Vac. Sci. and Technol. A* 2017. 35, 03E107 with the permission of AIP Publishing.

4.2.2.2 Optical Polarizability

Previous work has shown a dependence of the molecular polarizability on film density in plasma-enhanced TiO_2 films with a mixed amorphous/anatase structure.[123] The optical polarizability α_{opt} effectively describes the electronic interactions between the component ions, Ti^{4+} and O^{2-}, which can change depending on both the stoichiometry and the local atomic structure. The optical polarizability is captured in the Lorentz-Lorenz relation, given as:

Equation 4.2. $$\boldsymbol{\alpha_{opt}(\nu) = \frac{3}{4\pi N} \times \left(\frac{\hat{n}^2(\nu)-1}{\hat{n}^2(\nu)+2}\right)}$$

where N is the atomic density, $\hat{n}$ is the refractive index, and ν is the frequency of the incident light. Here, we have used XRR and ellipsometry to independently extract the atomic density and refractive index respectively for each thin film. By converting atomic density (N) to mass density (ρ) using a formula unit of TiO_2, we can then use the independently measured values of atomic density and refractive index along with Equation 4.2 to directly compute the optical polarizability of these thin films. Calculated optical polarizabilities as a function of mass density for our amorphous, ALD-grown TiO_2 thin films are shown in Figure 4.5. For reference, we also plot values from the literature for PECVD TiO_2 films with amorphous, anatase, and rutile structures.[123]

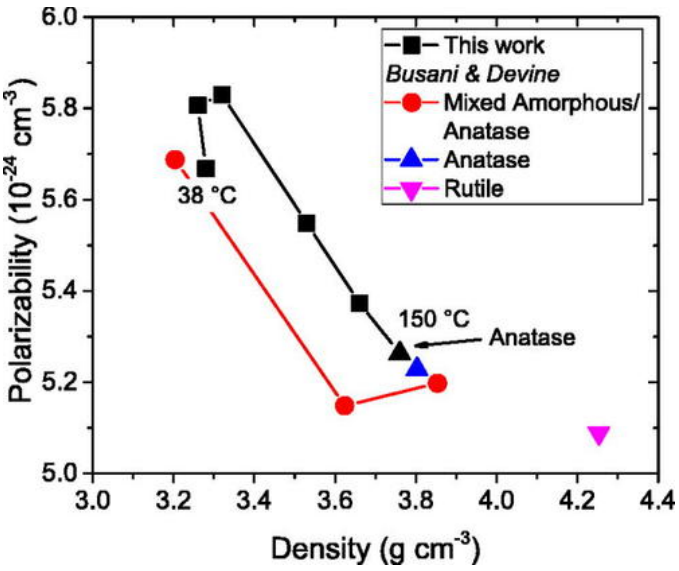

Figure 4.6. Optical molecular polarizabilities for ALD-TiO_2 (this work), PECVD-grown amorphous/anatase, anatase, and rutile films.[123] Reprinted from *J. Vac. Sci. and Technol. A* 2017. 35, 03E107 with the permission of AIP Publishing.

TiO_2 thin films grown by ALD are similar in both density and electronic structure to those grown by other techniques, such as PECVD. Measured values match the properties of the low-density amorphous TiO_2 and the crystalline anatase material. However, the optical, electronic, and physical density of amorphous materials can vary considerably depending on the ALD deposition temperature. Using ALD, we can systematically vary the molecular polarizability of these TiO_2 thin films from 5.25×10^{-24} cm^{-3} to 5.83×10^{-24} cm^{-3}. For amorphous films with mass densities from 3.8 g cm^{-3} to 3.3 g cm^{-3}, polarizabilities increase monotonically. However, these polarizabilities are consistently higher than those reported for PECVD grown material.

We attribute this increase in polarizability to Cl impurities, as detected by ToF-SIMS. Fig. 7 presents representative ToF-SIMS analysis for a selection of these films. If the overall concentration of O^{2-} is relatively constant across different samples, these data indicate that the relative Cl^- concentration is strongly dependent on growth temperature,

and Cl^- concentration increases significantly at low growth temperatures. A significant decrease in Cl^- concentration is also detected above 160°C when the film crystallizes. We expect Cl^- to increase the apparent density of the film by increasing the local electron concentration (scattering source for XRR) compared to O^{2-}. We also expect Cl^- to have a higher polarizability than O^{2-} based on its ground state atomic polarizability (2.18 $x10^{-24}$ cm^{-3} for Cl vs 0.802 $x10^{-24}$ cm^{-3} for O).[131] We therefore would expect that a TiO_2 thin film contaminated with moderate levels of Cl^- impurities to have both a higher *atomic* density and higher polarizability than a more pure TiO_2 thin film.

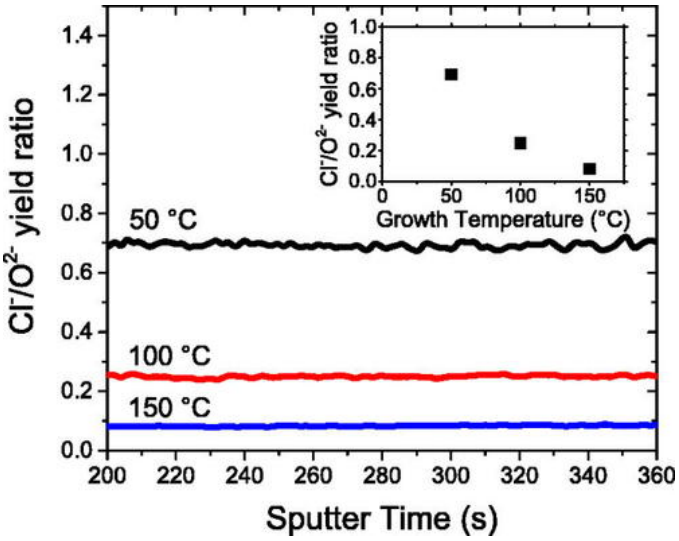

Figure 4.7. SIMS measurements showing the ratio of the sputter yield of Cl^- ions vs O_2^- in the bulk of the TiO_2 films. Sputter time is indicative of depth into the sample; the first 200 s are not included to avoid surface effects. Sputtering of the 50 °C film for 600 s did not penetrate through the TiO_2 layer and did not show any change in the Cl^-/O^{2-} ratio. Therefore, the pictured Cl^-/O^{2-} ratio for all samples is assumed to be representative of the bulk. (Inset) The averaged Cl^-/O^{2-} yield ratio for TiO_2 thin films prepared at three different growth temperatures. Reprinted from *J. Vac. Sci. and Technol. A* 2017. 35, 03E107 with the permission of AIP Publishing.

While the presence of Cl^- contamination explains the higher polarizabilities than previously reported PECVD material, it does not explain the decrease in polarizability with the film growth at 38°C. It is possible that the Cl^- concentration in films grown at such low

temperatures disrupts the local film structure in a way not simply modeled by the Lorentz-Lorenz function.

4.3 Thermal Properties of Low-Temperature ALD-TiO_2 Films

4.3.1 *Introduction*

The thermal properties of thin films often deviate significantly from their properties in the bulk due to size effects from electrons and phonons. Understanding how these thermal properties change with thin films of low densities and thickness is essential for the development of low thermal conductivity (κ) materials. ALD provides a high-precision platform for tuning the physical properties of thin oxide films through control over deposition temperature. Through control over atomic density and film thickness, it is possible to extract thermal resistances within a thin film along with scattering resistances from interfaces. With the growing importance of ALD in microelectronics and other temperature-sensitive applications, it is critical to understand how thermal conductivity is in amorphous films at the nanoscale.

The ability to systematically vary density and film thickness via ALD also provides the opportunity to validate different predictive models proposed for thermal conductivities in amorphous films. Many amorphous materials have been proposed to follow the "minimum limit model" for thermal conductivity[132], which only takes the speed of sound in a material and its atomic density, and which has been validated for many amorphous systems with low thermal conductivities. However, this model tends to fail for heterogeneous materials that have modified atomic structures or atomic densities below their theoretical value. A correction for this model is the "differential effective medium" model, which corrects the minimum limit model by incorporating an effective medium

calculation to account for the density difference versus the ideal density. This approach has been successfully validated in several low-κ heterogeneous systems.[124, 133]

Time-domain thermoreflectance (TDTR) is a highly sensitive thermal conductivity measurement technique particularly well suited to thin films, especially those with low thermal conductivity.[80, 82, 84, 134-136] TDTR is a laser pump-probe technique that measures the intensity of reflected thermal waves as they propagate into a film as a function of time, which is then compared to a model of the heat transport of our system under study to extract the thermal conductivity of each film.. Details of the TDTR measurement technique and corresponding data analysis are described elsewhere,[80, 137-138] while the specific sensitivity analyses and TDTR pump-probe traces for this work can be found in the full article.[127]

4.3.2 *Key Findings*

4.3.2.1 Thickness Dependence

Thermal resistances, R, and the calculated effective thermal conductivities, κ_{eff}, for Al_2O_3 and TiO_2 thin films are shown in Figure 4.8. The effective thermal conductivity is calculated by $\kappa_{eff} = \frac{d}{R}$, where d is the film thickness. Al_2O_3 films at low thicknesses demonstrate a negligible difference when grown on quartz substrates versus silicon substrates, indicating that at low thicknesses the substrate has minimal impact on the system thermal conductivity. In both Al_2O_3 and TiO_2 films, R and, hence κ_{eff}, increases with increasing film thickness, consistent with previous studies. This behavior has been attributed to the increased contribution of the intrinsic film resistance to the overall film resistance as the film thickness increases.

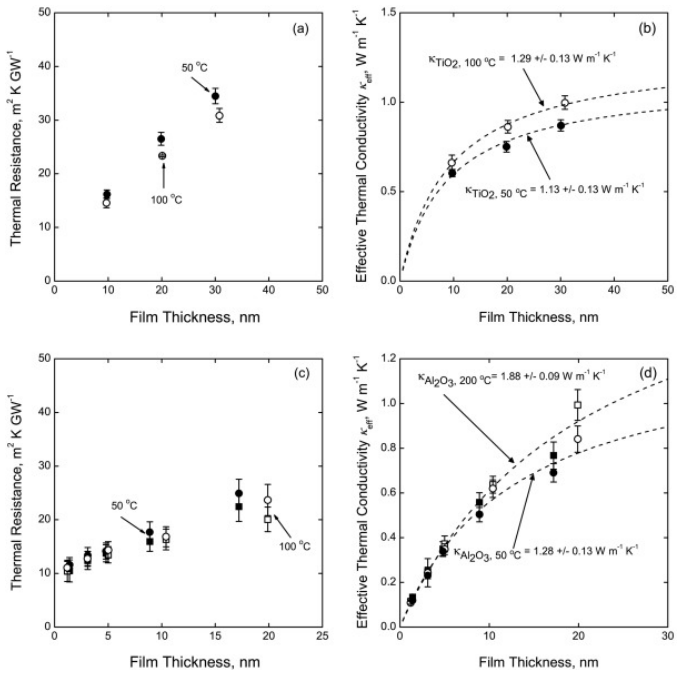

Figure 4.8. Thermal resistances *R* (left) and calculated effective thermal conductivies κ_{eff} (right) for TiO_2 (top) and Al_2O_3 (bottom) thin films. Al_2O_3 films were deposited on quartz (squares) and silicon (circles) substrates. Dashed lines are a fit to the series-resistor model shown in Equation 4.2.

A series resistor model is used to extract the contributions from interfacial resistances versus the intrinsic thermal conductivity, shown as follows:

Equation 4.2. $$\kappa_{eff} = \frac{\kappa_i}{1+\frac{R_{tot}\kappa_i}{d}}$$

R_{tot} is the total thermal boundary resistance from the Al/film and film/substrate interfaces, and κ_i is the intrinsic thermal conductivity of the amorphous film. For TiO_2 the thermal boundary resistance is calculated as 7.5 m^2 K GW^{-1} regardless of substrate or deposition temperature. However, the high thermal resistance of the TiO_2 films mean that the TDTR measurement in this situation is not sensistive to the boundary resistance.

4.3.2.2 Density Dependence

The thermal conductivity for Al_2O_3 and TiO_2 films as a function of refractive index, which is directly correlated to atomic density, is shown in Figure 4.9. With increasing

density, the observed thermal conductivity also increase, consistent with prior studies on the effect of reduced atomic density on thermal conductivity in amorphous films.[124]

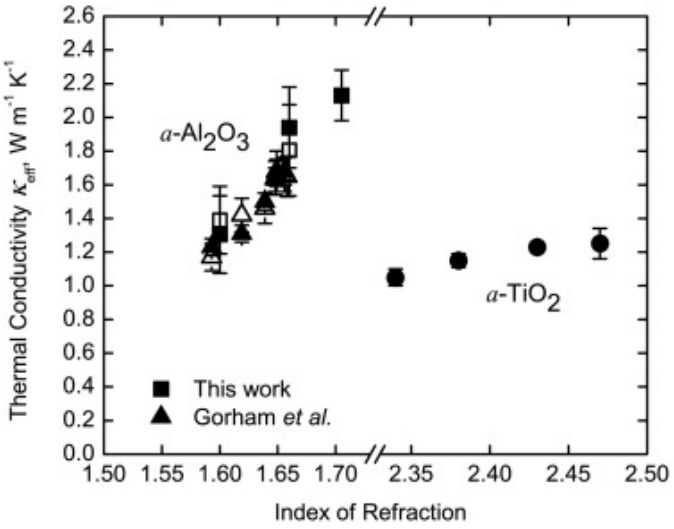

Figure 4.9. Thermal conductivity of a-Al_2O_3 and a TiO_2 as a function of refractive index. Al_2O_3 was deposited on quartz (open symbols) and silicon (filled symbols). Film thickness across all samples were held constant at 50 ± 5 nm.

The reduction in the thermal conductivity was then compared to the minimum limit model[132], expressed as:

Equation 4.3.
$$\kappa_{min} = \frac{\hbar^2}{6\pi^2 k_B T^2} \sum_j \int_0^{\omega_{c,j}} \frac{\tau_{min,j}\omega^4}{v_j} \frac{\exp\left(\frac{\hbar\omega}{k_B T}\right)}{\left(\exp\left(\frac{\hbar\omega}{k_B T}\right)-1\right)^2} d\omega$$

where κ_{min} is the minimum thermal conductivity, j is the phonon polarization index, τ_{min} is the minimum scattering time, ω is the angular frequency, $\omega_{c,j}$ is the cut-off frequency, and υ_j is the phonon group velocity. The speeds of sound for Al_2O_3 and TiO_2 are taken from literature[124, 139] and the density values for "fully-dense" Al_2O_3 and TiO_2 are used to compute the cut-off frequencies. Fits to this model are shown as solid lines in Figure 4.10.

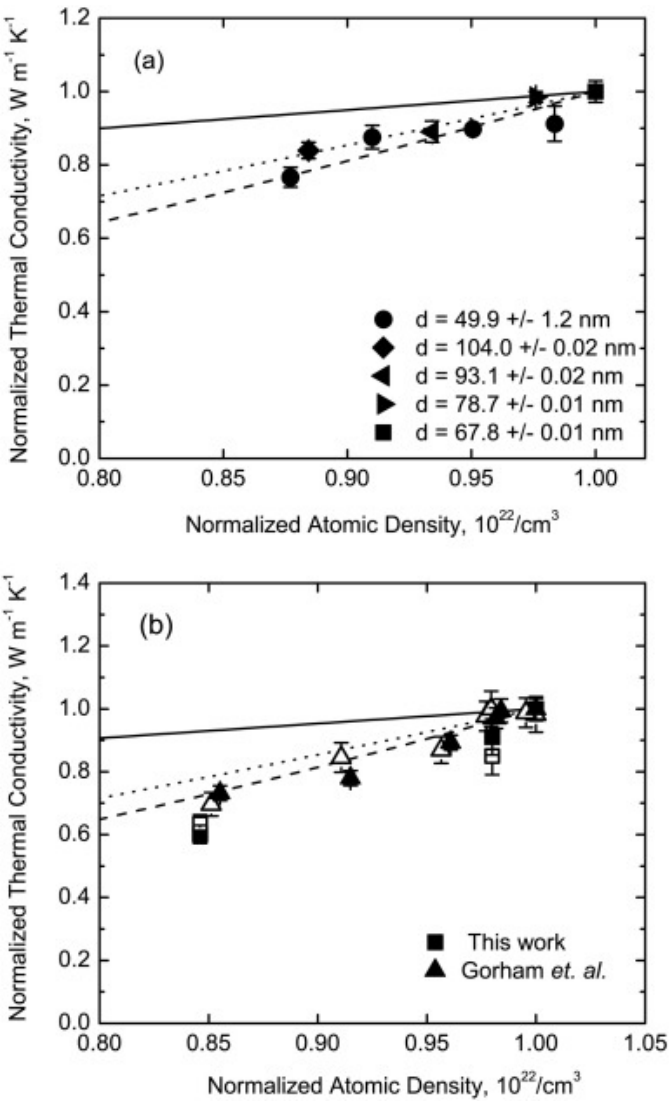

Figure 4.10. Normalized thermal conductivity of the a) a-TiO_2 and b) a-Al_2O_3 films as a function of normalized atomic density. Solid lines show the minimum limit model, the dotted lines the DEM approximation, and the modified DEM model in dashed lines.

To account for the reduced density in the amorphous films, a differential effective medium (DEM) model was used. In the DEM model, an "effective medium" is introducd, accounting for the extra "space" between the atoms. This model states that the thermal conductivity should scale with density, given as:

Equation 4.4. $$\kappa_{DEM} = \kappa\left(\frac{n}{n_{bulk}}\right)^{\frac{3}{2}}$$

In this model, κ can either be taken from the films with the maximum thermal conductivity, corresponding to the highest experimentally achieveable density, or it can be taken from the predictions from the minimum limit model in Equation 4.3. The model with the experimental is shown in Figure 4.10 as dotted lines while the minimum limit corrected model is shown as dashed lines.

From these data, we observe that the minimum-limit modified DEM model exhibits strong agreement with the the thermal conductivity data observed from experiment for both TiO_2 and Al_2O_3, suggesting that this model is a promising approach for predicting the thermal conductivities in low thermal conductivity thin films.

4.4 Electronic Transport in ALD TiO_2 Thin Films

4.4.1 *Introduction*

Although TiO_2 is known to have a high dielectric constant and is typically thought as non-conductive, it is commonly used use for injected electron transport due its low rate of recombination leading to long lifetimes and mean free paths within the film. More recently, hole conduction has been observed in TDMAT-grown films when used as an interlayer between a Si light absorber and a Ni or Ir photocatalyst. The source of the hole conduction has been a source of much discussion in the literature. The hole conduction is relatively insensitive to film thickness, with conduction observed in films up to 143 nm thick.[99] Some studies have proposed a defect-mediated conduction[99] but subsequent work examining films grown by different techniques don't show a specific dependence of conduction on defect states.[98] To further clarify the source of facile hole transport in TiO_2, we examined the effect of Ti^{3+} states on the conduction of a-TiO_2 films. Ti^{3+} states, visible through electron paramagnetic resonance (EPR) spectroscopy and valence band XPS, play

a large role in the electrical and optical properties of TiO_2.[140-146] Ti^{3+} is often associated with structural disorder and oxygen doping. The tunability of the ALD technique allows us to study the behavior of different forms of *a*-TiO_2 as a function of deposition temperature and precursor type. Understanding the source of hole-conduction in ALD-grown *a*-TiO_2 layers is critical for designing efficient visible light absorbers and photocatalytic systems.

4.4.2 *Key Findings*

The current-voltage characteristics of p+-Si|a-TiO_2|Ni are shown in Figure 4.11. All the ALD films showed Ohmic characteriztics at low biases, but at the same applied the TDMAT-grown film had more that an order of magnitude higher current density versus the least-resistive $TiCl_4$-grown film. The conductivities of the $TiCl_4$-grown films increased with growth temperature. Free carrier concentrations for the $TiCl_4$-grown films were 1-3 orders of magnitude smaller than the carrier concentration of the TDMAT-grown film, although the carrier concentrations increased with deposition temperature.

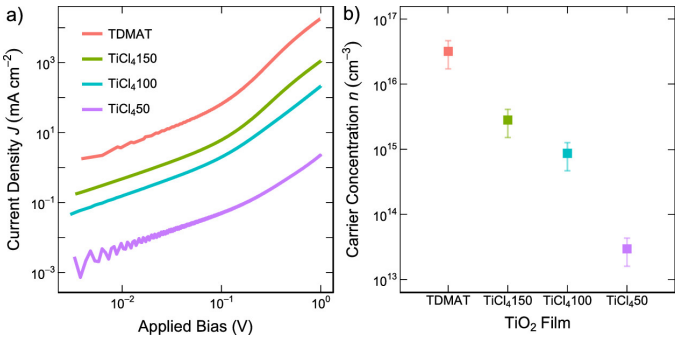

Figure 4.11. a) *J-V* curves and b) free carrier concentrations for p$^+$-Si|a-TiO_2|Ni film stacks, where the a-TiO_2 is grown by TDMAT-H_2O at 150 ˚C or $TiCl_4$-H_2O at 50, 100, or 150 ˚C. Reprinted with permission from Nunez, P. *et al. J. Phys. Chem. C* 2019, 123, 33, 20116-20129. Copyright 2019 American Chemical Society.

XPS valence band spectra of the TDMAT- and $TiCl_4$-grown films are shown in Figure 4.12. There is a small peak in all ALD-grown samples centered at 0.94 eV. The TDMAT-grown film is more intense in this region than the $TiCl_4$-grown films.

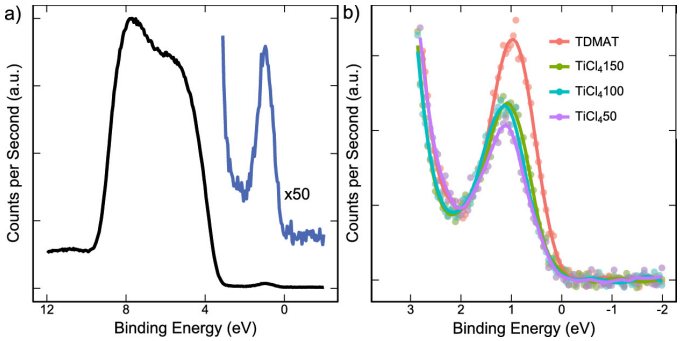

Figure 4.12. a) Valence-band XPS spectrum of TDMAT-grown film, with magnification. b) Valence-band XPS spectra of TDMAT- and $TiCl_4$-grown films. Reprinted with permission from Nunez, P. *et al. J. Phys. Chem. C* 2019, 123, 33, 20116-20129. Copyright 2019 American Chemical Society.

EPR spectra for the ALD-grown TiO_2 films are shown in Figure 4.13. The isotropic *g*-value calculated from the spectra at 1.939 is consistent with the presence of Ti^{3+} states.[147-148] There is also a sharp peak observed at a *g*-value of 2.000 in the 150 ˚C $TiCl_4$-grown ALD film. The sharpness of this peak may correspond to electrons trapped at oxygen vacancy sites or crystalline defects in the 150 ˚C-grown film. The same sharp peak is not present in the lower-temperature grown ALD $TiCl_4$ films.

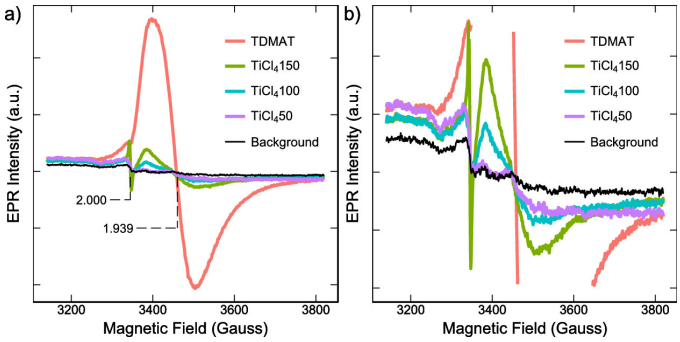

Figure 4.13. a) EPR spectra of the different ALD-grown TiO_2 films. b) Rescaled EPR spectra to show details of the smaller peaks. Reprinted with permission from Nunez, P. *et al. J. Phys. Chem. C* 2019, 123, 33, 20116-20129. Copyright 2019 American Chemical Society.

^{12}C and ^{14}N SIMS spectra of the ALD-grown films are shown in Figure 4.14. These impurities were selected becauuse they are potential impurities in the TDMAT precursor,

which has the formula $Ti(NMe_2)_4$. In contrast, the $TiCl_4$ precursor should have no C or N impurities. The concentration of ^{12}C and ^{14}N through all the ALD films are similar and very low, indicating that there is minimal contribution from extrinsic dopants in the TiO_2 films.

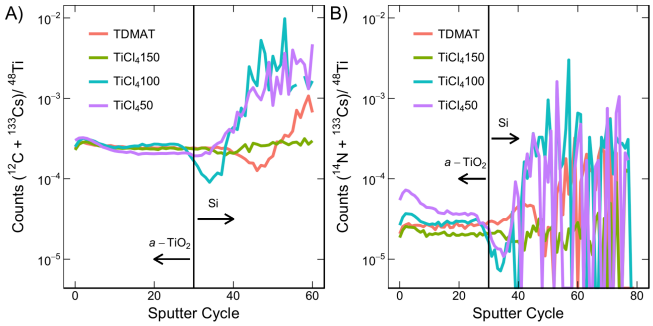

Figure 4.14. SIMS measurements of a)^{12}C and b)^{14}N for TiO_2 grown with TDMAT and $TiCl_4$ as a function of sputter cycles into the film. Reprinted with permission from Nunez, P. *et al. J. Phys. Chem. C* 2019, 123, 33, 20116-20129. Copyright 2019 American Chemical Society.

The EPR measurements show that there is a much higher concentration of Ti^{3+} states in the TDMAT-grown films compared to the $TiCl_4$-grown films. These Ti^{3+} sites are associated with oxygen vacances, which dope the film and provide trapping sites for free electrons in localized Ti-O octahedra.[149] These results have been validated by calculations which predict oxygen vacancies are the most probable origin of structural defect sites in TiO_2.[150-151] These Ti^{3+} sites, however, are not apparent by angle-resolved XPS measurements of the surface, indicating that their concentration is below the detection limit for XPS or that the surface layers are oxidized in contact with air or water, removing the Ti^{3+} states and oxygen vacancies. In this case, oxidation of surface sites would cause the surface layer to become more resistive; to avoid this, top contacts should be deposited without breaking vacuum to preserve the low-resistivity states in the as-deposited TiO_2 film.

From these results, we can conclude that the source of high hole conductivity in amorphous TiO_2 is likely due to oxygen defects and Ti^{3+} states in the TiO_2 film. The EPR results show that these defects are intrinsic to the film as deposited as the technique probes the bulk of the film. These results explain why the conduction persists through relatively thick ALD TiO_2 films. These results also demonstrate that extrinsic impurities are likely not the source of the conductivity, indicated by the low dopant concentrations measured by SIMS. These properties are therefore linked solely to the structure of the ALD film, which is controlled by both deposition temperature and precursor type.

4.5 Conclusions

Amorphous TiO_2 films deposited by ALD have a wide variety of structural, optical, thermal, and electronic properties that are extremely sensitive to the deposition conditions and precursor type. At deposition temperatures from 38 ˚C to 150 ˚C, film densities change by 15%, changing from 3.2 to 3.8 g cm^{-3}. This change in density directly correlates to changes in properties like the refractive index, which goes from 2.30 to 2.45 (measured at 550 nm) and the thermal conductivity which increases from 1.0 to 1.3 W $m^{-1}K^{-1}$. We also observe the onset of crystallization using Raman spectroscopy at a deposition temperature of 150 ˚C. The critical crystallization temperature in TiO_2 films is sensitive to deposition temperature, film thickness, and precursor type—TiO_2 films grown by TDMAT at the same temperature and thickness were fully amorphous. Using optical and X-ray measurements, we also calculated the optical polarizabilities for amorphous TiO_2 films as ranging from 5.26 up to 5.81 $x10^{-24}$ cm^{-3}, corresponding to the increased interatomic distances in reduced-density films along with possible defected states.

The reduced density films were used to validate thermal conductivity models used for low-temperature, amorphous materials. Precise control over the film density via ALD growth enables a systematic across densities and film thicknesses to extract the intrinsic thermal conductivity of ALD oxide thin films, as well as the interfacial boundary resistances. It was found that a differential effective medium model correction to the classic minimum limit model closely predicted the thermal conductivity of both amorphous Al_2O_3 and TiO_2 films, in contrast to the naïve minimum limit model along with an experimentally calculated DEM model. These results will enable future work in predicting and designing low thermal conductivity oxide films.

The effect of growth temperature and precursor was then investigated to elucidate the source of significant hole conduction in amorphous TiO_2. Electron paramagnetic resonance spectroscopy showed that Ti^{3+} defect states were the primary source of hole conduction, caused by oxygen vacancies trapping free electrons in local Ti-O octahedral structures. The EPR results showed that these states were highly dependent on the TiO_2 precursor, with TDMAT-grown films exhibiting much higher conductivity and Ti^{3+} concentration than $TiCl_4$-grown films deposited at the same or lower temperature. However, these defects were not visible in core-level XPS, with only valence-band XP showing the defect band due to the free electrons and oxygen doping. These results indicate that oxidation caused by exposure to air or water may quench the surface doping, implying that further photoelectrochemical systems using this approach should seek to avoid oxygen contamination to preserve high-conductivitiy contacts. Extrinsic dopants were shown to have minimal to no impact on the structure and conduction of the a-TiO_2 films, indicating

again that short-range film structure plays a major role in the properties of amorphous films.

CHAPTER 5. EPITAXIAL FILM GROWTH OF ZINC OXIDE ON C-SAPPHIRE WITH PULSED HEATING ATOMIC LAYER DEPOSITION

This chapter describes the use of a pulsed-heating ALD (PH-ALD) system using a high-power resistive heater to grow epitaxial ZnO films on c-sapphire from low-temperature precursors, demonstrating that PH-ALD is an effective technique for controlling crystallinity in ALD film growth. This proof-of-concept work shows that a simple resistive heater solution can grow films with unique morphologies that cannot be accessed by simple post-deposition anneals, and indicates that further investigation into PH-ALD technologies may enable new complex crystalline growth techniques via ALD.

5.1 Introduction

Pulsed-heating ALD in the literature has principally focused on the densification[62-63] or induced crystallization[64-66, 152] in amorphous films. The ability for PH-ALD to increase film density beyond what can be achieved by a similar post-deposition anneal indicates that there is unique solid-state chemistry occurring during the layer-by-layer anneal process.

Pulsed heating for atomic-scale epitaxial growth was explored during the early days of the atomic layer epitaxy field for the growth of Si and Ge from SiH_4 or GeH_4, respectively.[153-154] In this work, a CVD chamber with SiH_4 or GeH_4 with an integrated Xe flash lamp was used to alternately dose a purge gas or the precursor. During the precursor dose, the Xe flash lamp was flashed in short pulses several times. Unlike the more familiar modern ALD, no co-reactant was used, and only the sticking parameter of the precursor onto the substrate was used to enforce the self-limiting adsorption component. By carefully selecting the substrate temperature and precursor gas flow, consistent monolayer growth

could be achieved, with crystalline registry to the substrate material. A key concept in this work is that the adsorption dynamics should be separated from the reaction dynamics, which can be tuned independently using the substrate temperature and the pulse energy and frequency, respectively.

By using contemporary ALD precursors, we can rely on chemisorption instead of physisorption to adhere the precursor monolayer to the substrate surface. We therefore do not need to rely on substrate temperature to enforce self-limiting adsorption. Pulsed-heating then can drive surface reorganization, thereby promoting crystallization and crystallographic registry. This adds a third dimension to the atomic layer deposition picture, becoming adsorption, reaction, and structure or crystallization.

In this chapter, I will describe the use of resistive pulsed-heating ALD to grow epitaxial ZnO on c-plane sapphire. ZnO is a well-established material with applications in solar energy, photocatalysis, and piezoelectricity[155-157] and has been grown epitaxially with a number of techniques, including PLD[158], MBE[71, 159-161], PED[72], MOVPE[162] and MOCVD[163]. properties, such as in Unlike most other ALD-grown films, ZnO typically is crystalline as deposited[15], growing in the wurtzite phase. The difficulty is therefore in directing the growth of the material to be epitaxial instead of polycrystalline.

Prior work on hydrothermally-grown ZnO nanowires has shown that ALD ZnO can grow homoepitaxially on a ZnO seed layer.[164] Using this property, previous workers have used ALD to heteroepitaxially grown ZnO on substrates with low in-plane lattice mismatch, such as SiC[165] and GaN[166-168], with mismatches of 6% and 1.8%, respectively. Additionally, ZnO has successfully been grown on c-plane sapphire, which has a much higher lattice mismatch of 18.4%, by high-temperature ALD using $ZnCl_2$ and O_2.[169-171]

These studies indicate that growth temperature is the principle driving factor for the epitaxial growth of ZnO, with higher temperatures required to deposit directly onto substrates with higher lattice mismatches.

The objective of this work is to demonstrate how resistive pulsed-heating ALD can replicate the behavior of high-temperature ALD processes while using low-temperature organic precursors. I will focus on the epitaxial growth of ZnO on c-plane sapphire as a model system as a function of pulse temperature and pulse frequency. I will then examine how this approach can be used to deposit a thin seed layer of epitaxial ZnO layers, which can then be used to seed epitaxial growth through thermal ALD. I will also show how this deposition strategy results in films that are significantly different from post-annealed films from a structural perspective. This work will demonstrate how PH-ALD can be used to develop phase-controlled thin films using commonly available precursors in a low-cost and easy-to-implement fashion.

5.2 Experimental Methods

5.2.1 *Deposition Conditions*

PH-ALD deposition was conducted in a specialized PH-ALD reactor described in §2.2.2, with some ALD-only films grown in a different ALD reactor described in §2.1 to validate growth rates. For all PH-ALD samples, the chamber and deposition temperatures were 110 ˚C. Diethylzinc (99%, Strem) was used as-received for the precursor and deionized water for the oxidant. A single-crystal, *c*-plane sapphire (99.99% purity, MTI Corporation) was used for the substrate. Some ALD-only films were also deposited on test-grade [001] Si wafers with native oxide (WRS Inc.).

Each ALD cycle used a deposition sequence of 0.1s DEZ/30s purge/0.1s H_2O/30s purge, followed by the optional heat pulse sequence of t_{pulse}/180s purge, where the timings for the heat pulses are determined from the data shown in Figure 2.4. 500 ALD cycles were deposited for all conditions. Three different deposition series were explored: temperature, interleave ratio, and templating. For the temperature series, films were grown at pulse temperatures between 400 ˚C and 900 ˚C with one heat pulse for every ALD cycle. For the interleave series, all heat pulses were done at 900 ˚C and the ratio of ALD cycles to heat pulses was varied from 1:1 to 10:1. For the templating series, *x* PH-ALD cycles at a 900 ˚C pulse temperature and a 1:1 interleave ratio were first deposited, followed by 500-*x* standard ALD cycles at the chamber temperature. The value for *x* ranged from 1 to 50. Some ALD samples were also annealed in a flowing N_2 atmosphere at 900 ˚C for one hour. Due to long deposition times of up to 30 hours, especially for samples with 1:1 ALD:heat pulse ratio, most samples were only grown once or twice per condition.

5.2.2 *Characterization*

5.2.2.1 Structural Analysis

HR-XRD was used to characterize the crystallographic orientation of the samples. All characterization was conducted on a PANalytical Empyrean XRD system with a BBHD source optic and an PIXcel 2-dimensional detector. Calibration was conducted by first optimizing the height (Z) and inclination (ω) to the sample. The system was then calibrated to the position of the sapphire crystal by optimizing ω, the normal inclination χ (also referred to as ψ), and finally by 2θ-ω. From this position, 2θ-ω scans (corresponding to θ-2θ geometry in other systems) and ω rocking curves of the *002* ZnO peaks were taken. Off-

axis measurements were then measured for both Al_2O_3 $\{01\bar{1}8\}$ and the ZnO $\{10\bar{1}3\}$ films.[72]

Spectroscopic ellipsometry (alpha-SE, J.A. Woollam) was used to measure film thickness. A GenOsc model with a Tauc-Lorenz oscillator was used as the model for the ZnO layer. However, since the film stack uses sapphire as a substrate, spectroscopic ellipsometry had very unpredictable results since the substrate was essentially transparent. For the ALD-only films, thicknesses with low error were easily obtained. However, for many thermally-treated films it was difficult to resolve thicknesses with low measurement error likely due to a combination of the low substrate reflectivity and surface roughness.

AFM (Bruker Icon) was used to measure the surface topography of several samples. A n-Si tip (MikroMasch Hq:XSC11/AL) was used with a resonant frequency of 155 kHz, amplitude setpoint between 375-390 mV, and a scan rate of 1 Hz. ToF-SIMS (IONTOF 5-300) was used to measure sample composition as a function of film depth. The primary ion beam was oxygen at an accelerating voltage of 2 kV. The field of view was 150 μm x 150 μm and the beam was rastered over a 500 μm x 500 μm area. Depth profiles are presented starting from when the end of $-CH_3$ and Na^+ ion signals indicating surface contamination. Data is normalized to the total measured ion count and then to the maximum Al^+ signal.

5.2.2.2 Electrical and Optical Characterization

Room-temperature photoluminescence (PL) spectroscopy (Horiba Jobin Yvon HR800) with a 532 nm excitation laser was used to interrogate the optical properties of the films. Electrical characterization was conducted with an Ecopia HMS-5300 Hall effect measurement system at room temperature. Silver paste was used to make electrical contact to the ZnO surface.

5.3 Results and Discussion

5.3.1 *Growth Rate*

ALD films consistently grew at a rate of 0.18 nm/cycle, consistent with literature reports for the ALD of ZnO from DEZ+H_2O, PH-ALD samples under the most aggressive growth condition of every ALD cycle and 900 ˚C pulse temperature did show a reduction in growth rates to 0.16 nm/cycle (Figure 5.1). However, this reduction may be a function of increased density due to the pulses than a strictly reduced growth rate. Furthermore, the relatively high growth rates indicates that we are not sensitive to any potential evaporation of the ZnO surface layers as has been reported by other techniques.[162]

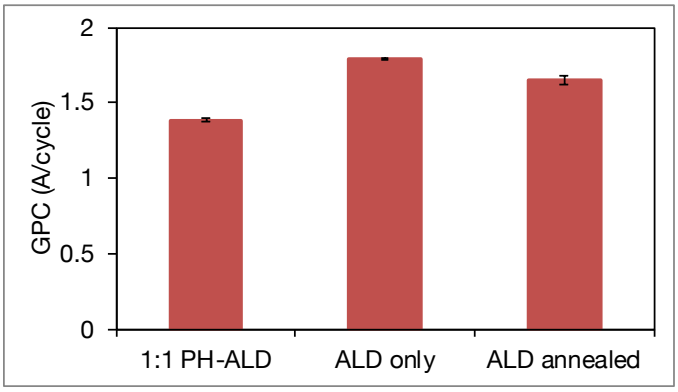

Figure 5.1. Growth rates between ALD, ALD with post-deposition anneal, and a 900 ˚C, 1:1 PH-ALD sample measured over 500 deposition cycles.

5.3.2 *Crystallography*

5.3.2.1 High-Temperature PH-ALD

2θ-ω scans for ALD, post-annealed ALD, and 1:1, 900 ˚C PH-ALD samples are shown in Figure 5.2. The ALD-only film has peaks for both the *002* and the *101* peaks, indicating the film is polycrystalline as-deposited, although the signal intensity is relatively low. After annealing, signal intensity increases significantly but the film remains polycrystalline. In contrast, the PH-ALD films have a very strong *002* reflection with no

101 signal, indicating that the PH-ALD film is fully oriented in the c-axis direction. Growth in the *002* plane is a common habit for ZnO, which often grows as a textured film.[172] We then measure the film mosaicity by ω rocking curves of the *002* ZnO peak. The FWHMs of these films are shown in

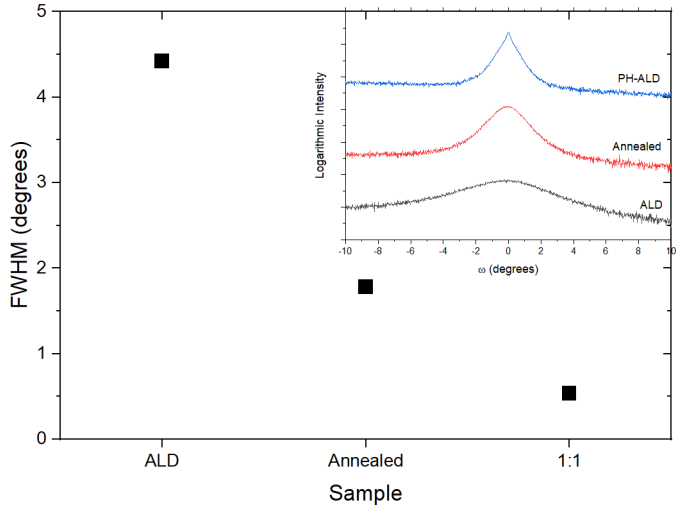

Figure 5.3. The PH-ALD film has a rocking curve FWHM of 0.53, which is comparable to that grown by other techniques like pulsed electron beam deposition with a FWHM of 0.65.[72]

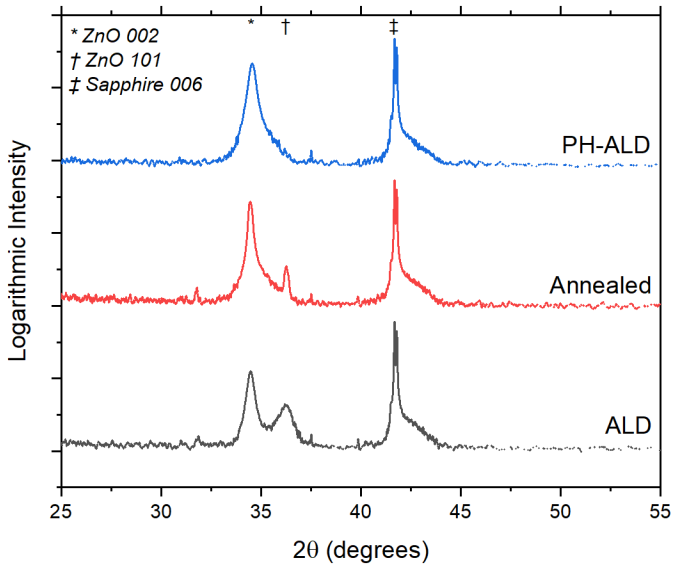

Figure 5.2. 2θ-ω of thermal ALD (bottom), ALD with a post-deposition anneal (middle) and 1:1, 900 ˚C PH-ALD (top).

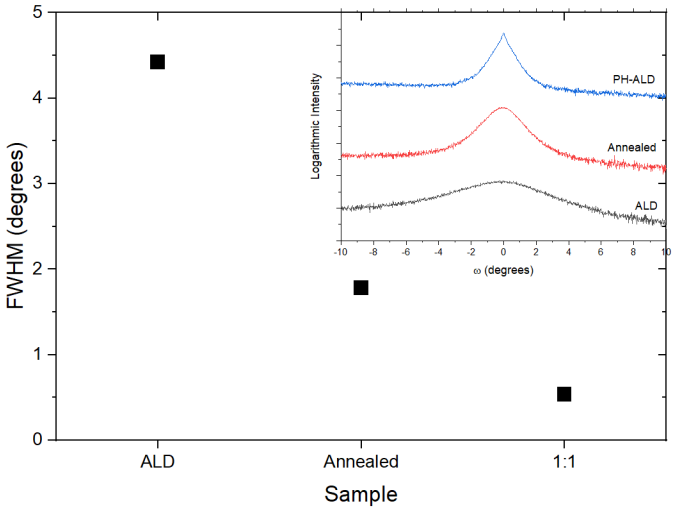

Figure 5.3. Rocking curve FWHM of the ZnO *002* peak for different growth conditions. (inset) Rocking curve traces.

To evaluate the epitaxial nature of the films, off-axis scans of the sapphire and ZnO were measured. The sapphire substrate shows three peaks offset by 120˚, while both the PH-ALD and post-annealed sample exhibit six well-defined peaks at a 60˚ offset, while the ALD only sample exhibits no particular peaks at the same inclination. In the PH-ALD sample, these peaks are offset by 30˚ relative to the Al_2O_3 substrate, while the post-annealed sample shows no such offset.

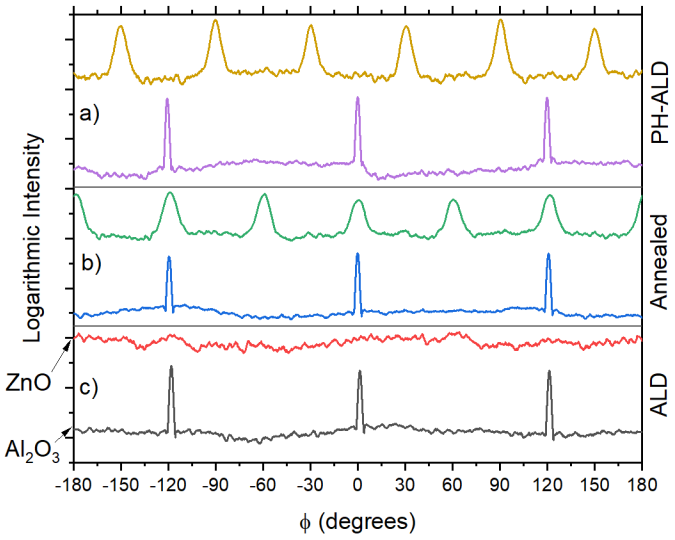

Figure 5.4. Off-axis rotation measurements of Al_2O_3 $\{01\bar{1}8\}$ (bottom traces) and ZnO $\{10\bar{1}3\}$ (top traces) signals for a) PH-ALD, b) ALD with N_2 anneal, and c) ALD only growth conditions

The unconventional six-fold symmetry for the ZnO peaks compared to the three-fold symmetry of the sapphire originates from steps on the c-plane sapphire surface.[173] The terraced surface provides different atomic surfaces for the growing film to nucleate on, permitting the growth of different crystalline variants that are nevertheless epitaxially aligned with the substrate. For the PH-ALD sample, the 30˚ offset from the sapphire substrate matches with the known epitaxial relationship:

Equation 5.1[159, 161] $$\mathbf{ZnO(0001)[2\bar{1}\bar{1}0]\ //\ Al_2O_3(0001)[1\bar{1}00]}$$

The 0˚ offset for the annealed ALD sample may correspond to graphoepitaxy on the sapphire step edges.[174-175] Graphoepitaxy describes the growth of aligned crystalline films constrained by surface topography of the substrate. In this case, the sapphire step edges combined with the hexagonal habit of both the sapphire and the ZnO constrain the growing ZnO film to a single rotational orientation instead of a fully random distribution, as seen in the ALD-only sample.

5.3.2.2 Varying Pulse Temperature

2θ-ω diffraction scans for PH-ALD samples with pulse temperatures from 400-900 ˚C are shown in Figure 5.5. Only the *002* reflection is observed at pulse temperatures of 600 ˚C to 900 ˚C, while both the *101* and the *002* reflections are present in the films grown at pulse temperatures of 500 ˚C and below. ZnO rocking curve scans, shown in Figure 5.6, show that the crystal quality increases with increases pulse temperature from a width of 3.5˚ at 500 ˚C to 0.5˚ at 900 ˚C. In the literature, ZnO films grown by other techniques also exhibit better crystal quality at higher growth temperatures, which is consistent with the growth behaviour seen in the PH-ALD system.[171]

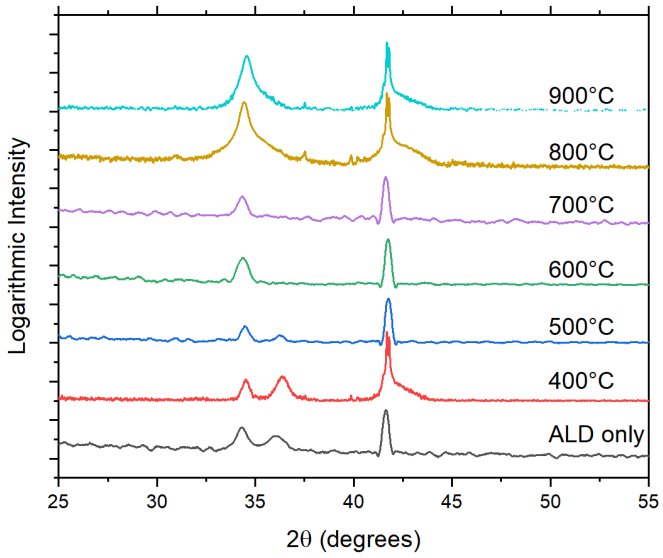

Figure 5.5. 2θ-ω scans of PH-ALD samples at different pulse temperatures.

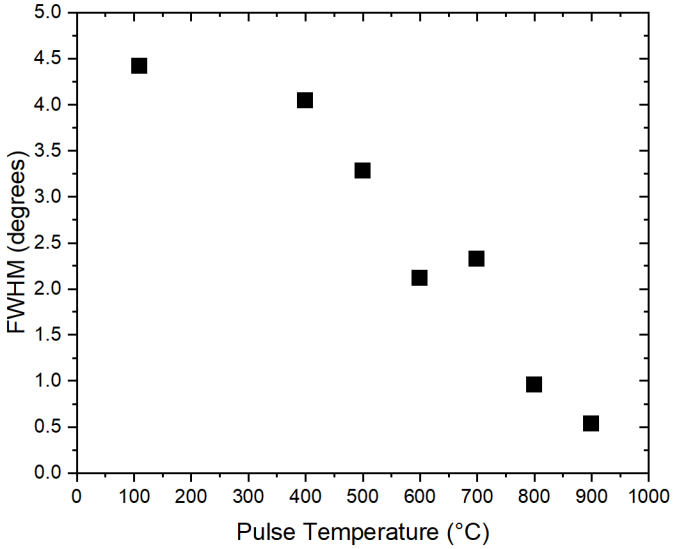

Figure 5.6. FWHM of ω rocking curves at the *002* ZnO peak for samples with different pulse temperatures. The ALD-only sample is marked as the pulse temperature of 110 ˚C.

5.3.2.3 Varying Interleave Ratio

To understand whether there is a transition phase from "layer-by-layer" annealing to "bulk" annealing, we investigated varying the ratio of ALD cycles to heat pulses. We looked at ratios from 1:1 ALD cycles to heat pulses to 5:1. 2θ-ω scans of these films are shown in Figure 5.7. For all the interleave ratios examined, no polycrystalline peaks were observed. This indicates that the ZnO crystallization is easily induced by the pulsed-heating approach and higher ALD:pulse ratios may be required to access a bulk annealing state. Rocking curve measurements, shown in Figure 5.8, show that the 1:1 films have the lowest FWHM, with the FWHM of higher-ratio films between 1 and 2˚.

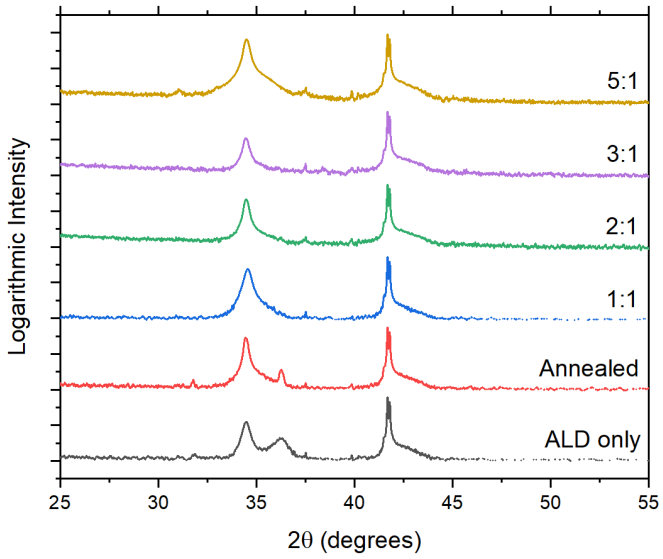

Figure 5.7. 2θ-ω scans of samples with varying [ALD cycles:heat pulse] interleave ratios, labelled on the left. N_2-annealed and ALD-only scans are shown for controls. All heat pulses are to 900 ˚C.

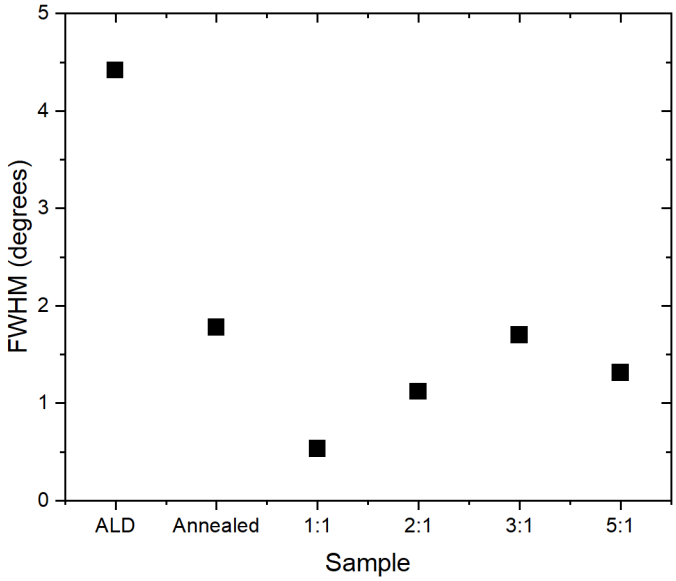

Figure 5.8. Rocking curve FWHM for films with different interleave ratios.

A potential reason that the interleave films do not exhibit a major change in crystallinity is the strong preference for ZnO to epitaxially template onto an appropriate substrate. The initial PH-ALD cycles may be sufficient to initiate the growth of an epitaxial seed layer, which can then template the following ALD layers with or without the heat

pulses. At significantly higher interleave ratios, it may be possible that the ALD-only growth component can initiate a polycrystalline seed layer which would then resemble the bulk-scale polycrystalline film.

5.3.2.4 Templated Films

Since ZnO can naturally grow homoepitaxially on a template via thermal ALD, standard ALD growth can be used as a probe to detect the minimum thickness required to nucleate an epitaxial ZnO film on sapphire. 2θ-ω scans are shown in Figure 5.9 from films composed of 1-50 PH-ALD cycles. For template thicknesses of 5 to 50 PH-ALD layers, films remain monocrystalline with only the *002* reflection present. There is no change until a single PH-ALD layer at which the film resembles the ALD-only film with a weak *002* and *101* reflection. Rocking curve FWHMs are shown in Figure 5.10. With thicker template layers, the FWHM decreases from 5.5˚ at 5 cycles to 1.3˚ at 50 cycles.

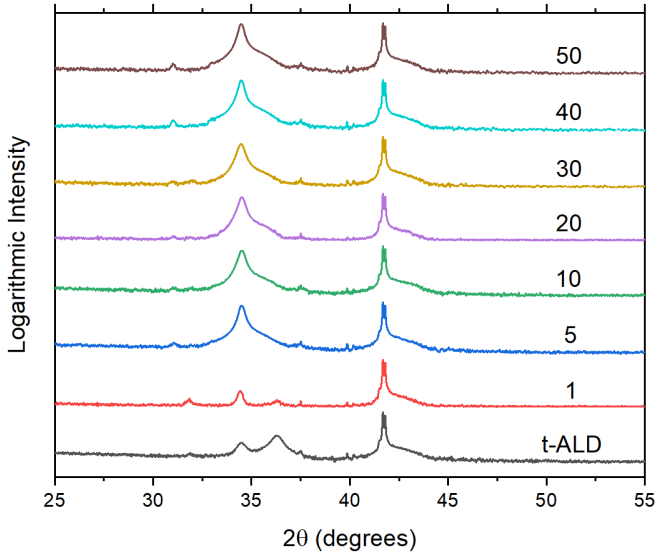

Figure 5.9. 2θ-ω scans for templated PH-ALD films, with *x* PH-ALD layers (noted in the annotations on the right) and 500-*x* thermal ALD layers. A control scan of ALD-only is noted as t-ALD.

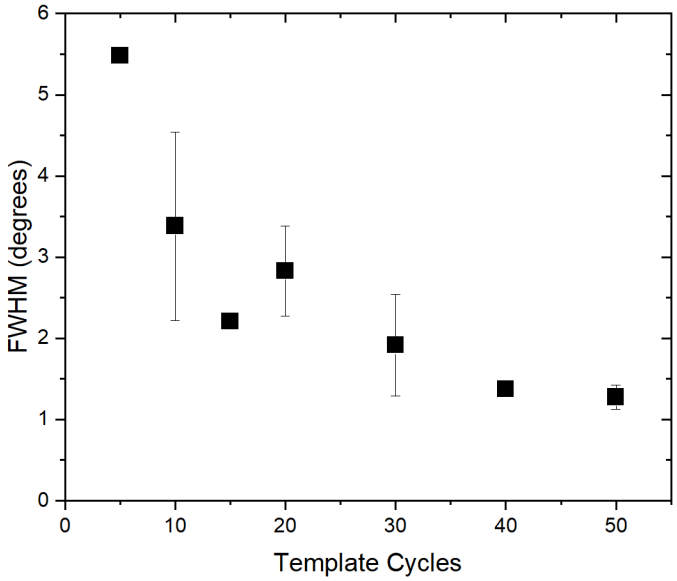

Figure 5.10. Rocking curve FWHM for PH-ALD templated films. No signal above background could be measured for the 1 PH-ALD cycle templated film.

Epitaxial films can be templated with as few as 5 PH-ALD cycles, but the crystal quality increases substantially with more template cycles. However, the improvement in crystal quality appears to slow down by 30-40 template cycles and does not appear to quickly approach the FWHM of the total 1:1 PH-ALD films. There is also more variance in crystal quality at lower temperatures, which may be due to higher sensitivity to the substrate morphology with thinner template films.

5.3.3 *Morphology*

The surface topography of sapphire and several PH-ALD-processed films was measured using AFM, shown in Figure 5.11 (height map) and . The ALD-only films are extremely smooth with a roughness of 0.3 nm, consistent with ALD literature. After annealing, the ALD films grow into large hexagonal crystallites with a crystal size between 100-200 nm with a roughness of 3.92 nm. In contrast, 400 ˚C and 900 ˚C PH-ALD samples have much smaller crystallite sizes of 25 and 35 nm, measured using an unbiased line counting frame, with the 400 ˚C sample having a roughness of 2.56 nm and the 900 ˚C a

roughness of 1.85 nm. A 50/450 templated sample shows larger-scale ordering, but does not show distinct crystallites like the PH-ALD or annealed samples. The difference in morphology between the PH-ALD and annealed films indicates that the growth mode of the two processes are extremely different. The PH-ALD films do not coalesce into large, distinct crystals and instead remain as a smooth compact film, indicating that there is minimal annealing of the bulk film even though the entire film is exposed to the high temperature pulses through the growth process. The template sample indicates that the nanocrystalline structure is not propagated through the ALD-only layer.

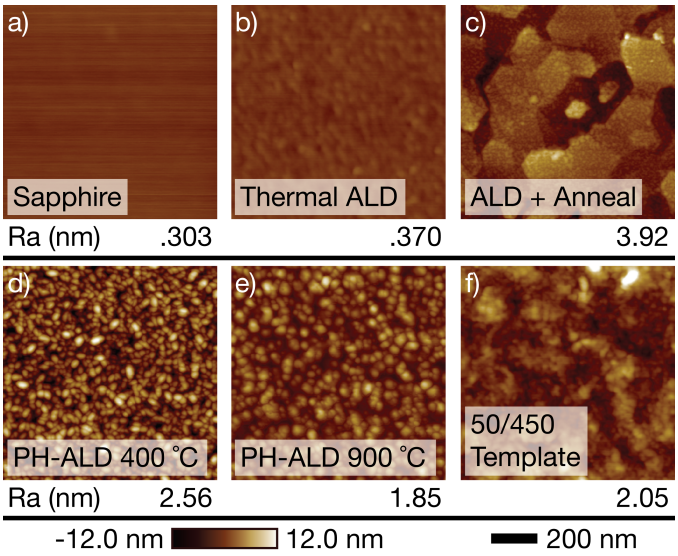

Figure 5.11. AFM images of surface topography for: a) bare sapphire, b) thermal ALD, c) annealed ALD, d) 400˚C 1:1 PH-ALD, e) 900˚C 1:1 PH-ALD, and f) 50/450 PH-ALD templated films. Images are from a 1 µm x 1 µm scan, with R_a roughness values calculated on a frame average basis and shown for each sample underneath the image.

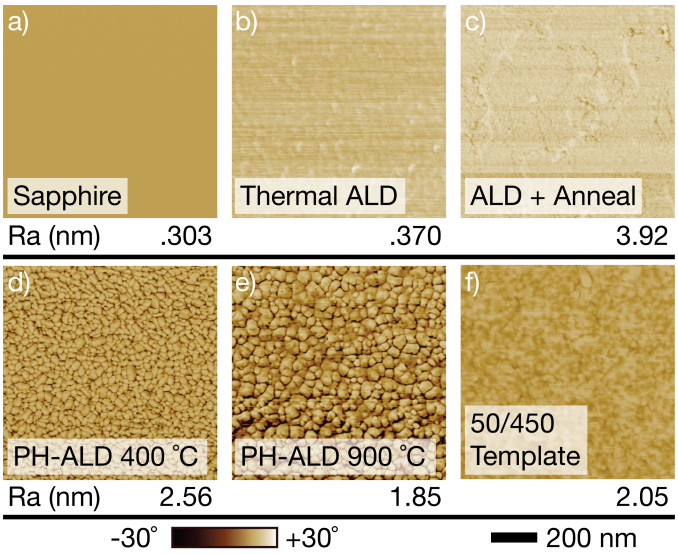

Figure 5.12. AFM phase images for a) bare sapphire, b) thermal ALD, c) annealed ALD, d) 400˚C 1:1 PH-ALD, e) 900˚C 1:1 PH-ALD, and f) 50/450 PH-ALD templated films. Approximate grain sizes for c), d), and e) are measured at 175, 25, and 35 nm, respectively, and measured using a line-based grid unbiased counting frame.

SIMS depth profiling was measured for the PH-ALD samples to interrogate interdiffusion between ZnO and sapphire films. SIMS profiles for sapphire, ALD-only, ALD with anneal, 1:1 PH-ALD films grown at 400 ˚C and 900 ˚C, and 50/450 templated films are shown in Figure 5.13. The ALD-only film shows an abrupt interface at the start of the sapphire film, indicating that there is minimal diffusion from the sapphire into the ZnO film. However, there is a long trailing Zn^+ signal into the sapphire bulk, indicating that the Zn^+ ions can readily dope into the sapphire surface even at low temperatures. Al-doping of ZnO has been commonly observed in the ALD literature in the growth of the transparent conducting oxide Al:ZnO (AZO)[176-177], but has not been noted for the doping into sapphire. In contrast to the ALD-only film, the post-annealed ALD film has a long intermixed domain extending deep within the sapphire film instead of an abrupt sapphire interface. The post-annealed film also has a number of pits extending through the entire

ZnO film to the sapphire substrate. In both high- and low-temperature PH-ALD films, there is no Al^+ doping through the ZnO layer until the interface. The 900 ˚C PH-ALD film appears to have a broader interfacial region than in the 400 ˚C film. Finally, in 50/450 templated film, there is a very abrupt Al^+ interface indicating that there is limited Zn-Al mixing in this condition.

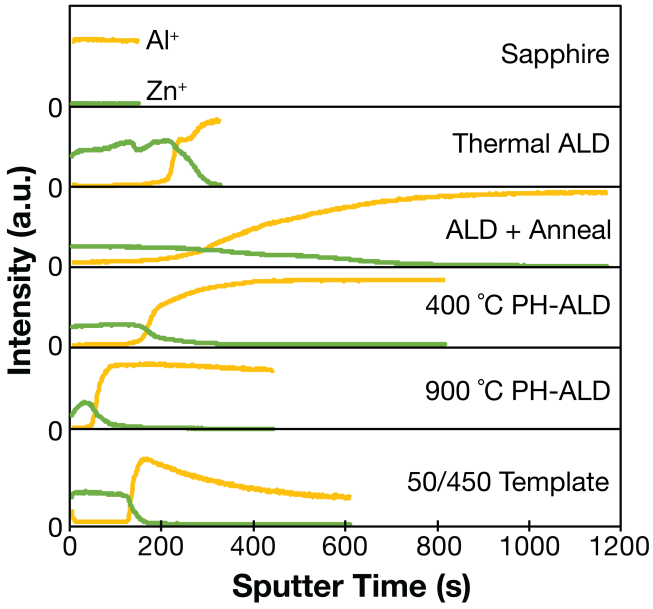

Figure 5.13. SIMS depth profiles into (top to bottom) sapphire, ALD, ALD + annealed, 400˚C PH-ALD, 900˚C PH-ALD, and 50/450 PH-ALD/ALD template. Yellow dashed lines are for the Al^+ signal and solid green lines are for the Zn^+ signal. Data is normalized to the total counts recorded by the instrument

5.3.4 *Optical and Electrical Properties*

Room temperature photoluminescence spectra of several PH-ALD films are shown in Figure 5.14. There is a single bright emission centered at 3.30 eV increases as the interleave ratio decreases from 5:1 to 1:1. This peak corresponds to the band edge emission of ZnO.[170] The N_2-annealed ALD sample appears to be at a slightly offset peak, centered at 3.28 eV, which is possibly replicated in the 1:1 PH-ALD film. The FWHM of all the samples are approximately 0.1 eV, consistent with room temperature PL of ZnO. [178]

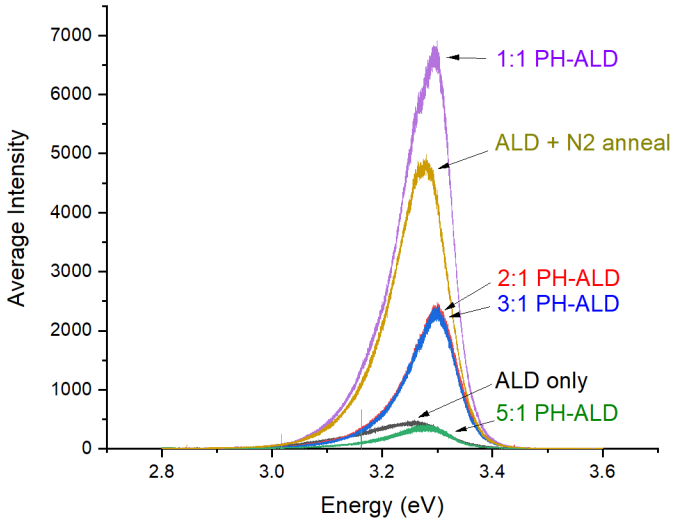

Figure 5.14. Room-temperature photoluminescence spectra for interleaved PH-ALD films.

The increasing intensity of the PL near-band-edge emission further confirms the improvement of the crystal quality with more intense PH-ALD processing. The slight shifts in the excitement edge between the annealed film and the PH-ALD films are possibly due to the different crystallite sizes of the two films as well as the strong Al doping into the annealed film. Further investigation is warranted using cryogenic PL to reduce the FWHM and separate out the excitonic mechanisms in the different films.

Carrier concentration and mobility measured by Hall-effect are shown in Figure 5.15. The ZnO is found to be *n*-type, consistent with other growth techniques. PH-ALD grown films have carrier concentrations from 10^{18}-10^{20} cm^{-3}, much higher than undoped films grown by techniques like PLD, which are typically in the range of 10^{16} cm^{-3}.[171] The electron mobility for the PH-ALD films range from 2-22 cm^2 $V^{-1}s^{-1}$, which are low compared to the theoretical mobility of ZnO in the bulk crystal of 300 cm^2 $V^{-1}s^{-1}$, but comparable to mobilities observed in techniques like PED of 11.53 cm^2 $V^{-1}s^{-1}$. Conductivities increase with PH-ALD intensity, reaching a maximum of 600 S cm^{-1} for the

1:1, 900 ˚C PH-ALD sample. In contrast, the ALD-only film had a conductivity nearly six orders of magnitude lower at 0.002 S cm^{-1}. Templated films exhibited higher conductivities than most of the interleaved films. The higher conductivities are due to a combination of the high carrier concentrations in the PH-ALD films with the high electron mobilities, especially in the higher intensity PH-ALD films. Overall, the PH-ALD films have electrical properties comparable to heteroepitaxial films grown on sapphire by other deposition techniques.

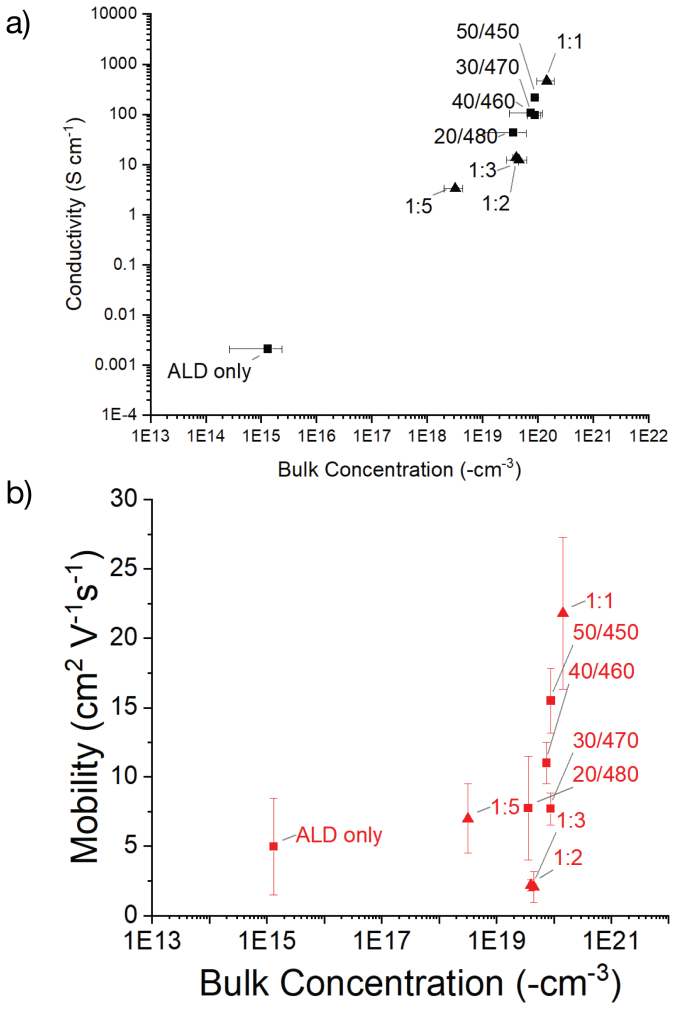

Figure 5.15. Electrical conductivity (top) and carrier mobility (bottom) measurements as a function of carrier concentration for interleaved and templated films.

5.4 Conclusions

PH-ALD was used to grow ZnO films on c-plane sapphire under a number of pulsed heating regimes using a high-power resistive heating stage. Pulse temperature proved to be the most sensitive method to control epitaxial growth and crystal quality, requiring temperatures above 500 ˚C to suppress the growth of the polycrystalline phase. With high temperatures, more frequent pulses, or thicker template films, the film quality and properties improved, consistent with the ZnO growth and PH-ALD literature. When compared to a post-deposition annealed ALD sample, crystallites in the PH-ALD samples were an order of magnitude smaller, did not exhibit pinhole defects, and only showed the epitaxial *002* crystal alignment. Electrical and optical properties of the PH-ALD films were comparable to films grown in the PVD and high-temperature CVD literature.

These results demonstrate that PH-ALD can be used to extend existing ALD techniques to direct crystalline growth in ALD films. The templating results show that epitaxial crystalline films can be nucleated with as few as 5 PH-ALD template cycles, persisting for 500 thermal ALD cycles. In standard ALD growth, the low growth temperature and layer-by-layer growth limit the development of crystalline seeds, requiring laminate structures and thicker films to constrain and direct the nucleation of films during post-processing. With PH-ALD, a few template cycles may be sufficient to build a dense crystalline layer of the target film and phase, promoting further crystalline growth by subsequent ALD cycles without requiring the long processing times added by the PH-ALD process. This strategy may have applications for film systems like ZrO_2 which is typically deposited using laminates like Al_2O_3 to control morphology. It may also be useful to aid in

depositing transition layers for heteroepitaxial systems that can be grown using an ALD process, such as an interlayer for GaO.

The PH-ALD technique may also be useful as a low-cost method for the growth of complex oxide films with multiple components. The broad library of chemistry and elements available to the ALD process makes it simple to add an element into an ALD process. Using PH-ALD, strategically-timed heat pulses can be used to drive multi-component phase transformations at the layer-by-layer level. By adjusting the pulse temperature and frequency, it may be possible to direct the growth of specific phases and structures, similar to other techniques like MBE or PLD. This proof-of-concept work shows that PH-ALD is a potentially valuable exploratory tool for phase-controlled ALD, with film properties comparable to other growth techniques. The resistive stage approach described in this chapter is a low-cost approach that can be easily integrated into existing ALD reactors for substrates that are heat-insensitive.

CHAPTER 6. CONCLUSIONS

6.1 Conclusions

Temperature is a key component in the ALD growth process but has typically been viewed as a parameter to control the ALD window of a precursor. Films grown at temperatures within the ALD window are typically then viewed as being structurally identical. This thesis has sought to demonstrate that temperature plays a significant role in directing film structure in both amorphous and crystalline films, even when all growth occurs within the ALD window. Furthermore, this thesis demonstrates that "growth temperature" can be finely manipulated in different stages of the ALD growth process to specifically manipulate **structure** without affecting **deposition**. By dynamically changing substrate temperature, desired film structures and phases can be chosen while keeping the deposition chemistry the same. This approach can open the door for ALD as a method for growing films with complex crystalline structures, which has not been well explored in the ALD community.

6.1.1 *Novel Control Systems for Sequential Deposition Tools*

A key objective of this thesis is to provide practical tools to the ALD and sequential deposition community for development of complex hierarchical structures leveraging the unique deposition capabilities of ALD-like processes. A major hole in the literature is a lack of openly published control systems and software for ALD tools, despite the wide availability of hardware designs. This thesis has attempted to resolve this issue by describing and providing an implementation of a novel software architecture that can be modified to meet the needs of complex sequential deposition tasks. The behavior tree system design is a robust algorithm from the AI and robotics communities, and makes it

possible to write complex recipes and program scripts without requiring programming knowledge. Many standard ALD processes can be naturally translated into this format, and the recipe format can be extended with capabilities like reading and responding to external sensors to adjust growth parameters on the fly.

This thesis also provides guidance for future workers on specific implementation strategies and good practices. Software architectures and designs for embedded and hardware-based control systems are often difficult to find. By providing hardware and software designs, this thesis seeks to provide future tool developers with a useful starting point to maintain and improve on existing sequential deposition control software.

6.1.2 *Film Properties of TiO_2 Deposited at Low Temperatures*

This thesis has illustrated how film density increases with deposition temperature in amorphous TiO_2 and how changing deposition temperatures can affect optical, thermal, and electrical properties of the film. The structural properties of films grown with the $TiCl_4$-H_2O chemistry at low temperatures has not been explored before this work. Using Raman spectroscopy, spectroscopic ellipsometry, and X-ray reflectometry, an increase in density of 15% was observed with growth temperatures from room temperature to 150 ˚C along with the onset of anatase crystal growth at 150 ˚C. These data also confirm that films grown by ALD are structurally similar to those grown by other growth techniques like PLD or reactive sputtering. These results are critical for ensuring that material properties and findings from other thin film communities are transferable to ALD films. Thermal and electrical measurements were then conducted to understand how different deposition conditions impact phonon and charge carrier transport through these films. Thermal studies indicated that decreasing the film density led to a corresponding decrease in the thermal

conductivity, consistent with results seen for other ALD systems and validating a differential-effective medium model for thermal conductivity in ALD films. Electrical studies then looked at how precursor choice affects the conduction mode and conductivity in ALD-TiO_2, pointing to new strategies for optimizing ALD-TiO_2 and related compounds for conductive interlayers.

6.1.3 *Heteroepitaxial Growth of ZnO on c-Sapphire*

This thesis then discussed the use of interleaved high-temperature heat pulses to direct the growth of heteroepitaxial ZnO films using a low-temperature ALD precursor. By exploring pulse temperatures and pulse frequencies, critical limits for the PH-ALD process to direct epitaxial growth in ZnO were identified. Using this information, a film templating strategy was used to determine that as few as 5 PH-ALD cycles were sufficient to template a thick epitaxial ZnO film grown by thermal ALD. Morphological studies indicated that the PH-ALD films, compared with post-annealed films, were significantly smoother with smaller crystallites and had a relatively abrupt elemental interface. Optical and electrical measurements of the PH-ALD ZnO films are also comparable to those produced by other growth techniques like PLD, PED, and MOVPE. These results demonstrate that: a) temperature is essential for directing crystal growth in ALD ZnO films, b) the timing of heat pulses is also critical for directing film structure as post-annealed films have substantially different structure and properties than PH-ALD films pulsed to the same temperature, and c) thin PH-ALD-grown template layers can effectively template epitaxial growth.

6.1.4 *Key Findings*

This thesis has contributed to the field with the following:

- A catalog of physical, optical, thermal, and electrical properties of TiO_2 grown by room to low-temperature ALD;
- The development of resistive pulsed-heating ALD for low-cost, phase-controlled film growth;
- A demonstration of using PH-ALD to grow heteroepitaxial ZnO films on highly strained lattices using low-temperature, well-established organic precursors;
- Hardware and software designs for ALD and resistive PH-ALD systems to enable the rapid development of new ALD technologies.

6.2 Dissemination

This research has been disseminated to the broader scientific community through publications and technical presentations, described below:

6.2.1 *First-Author Publications*

- **Piercy, B. D.**, Wooding, J. P., Gregory, S. A., Losego, M. D. "Heteroepitaxial Growth of ZnO on c-Plane Sapphire with the Diethylzinc-Water Reaction by Resistive Rapid Pulsed Heating Atomic Layer Deposition". *In preparation.*
- **Piercy, B. D.**, Losego, Mark. D. "Design and Thermal Properties of a Resistive High-Power Pulsed-Heating Atomic Layer Deposition Reactor". *In preparation*.
- **Piercy, B. D.**, Leng, Collen Z., Losego, Mark. D. "Variation in the density, optical polarizabilities, and crystallinity of TiO_2 thin films deposited via atomic layer deposition from 38 to 150 °C using the titanium tetrachloride-water reaction". *J. Vac. Sci. and Technol. A.* **35**, 03E107 (2017)
- **Piercy, B. D.**, Losego, M. D. "Tree-based control software for multilevel sequencing in thin film deposition applications". *J. Vac. Sci. and Technol. B*. **33**, 043201 (2015)

6.2.2 *Presentations*

- **Piercy, B. D.**, Losego, Mark. D. "Epitaxial Growth of ZnO on c-plane Sapphire Using Pulsed-Heating ALD". *ALD 2019*, Bellevue, WA. July 2019.
- **Piercy, B. D.**, Losego, Mark. D. "Microcontroller-based Sequential Deposition Control Systems using Behavior Tree Algorithms: ALD for the 'App Generation'". *AVS 64th International Symposium & Exhibition*, Tampa, FL. November 2017.

- **Piercy, B. D.**, Meyer, K. E., Hopkins, P. E., Losego, M. D. "A Fundamental Study of Thermal Conductivity in ALD-Deposited Amorphous Oxide Thin Films of Varying Density". *AVS 63rd International Symposium & Exhibition*, Nashville, TN. October 2016.

6.2.3 *Co-Authored Work*

In addition to the work described in this thesis, the author has collaborated on a number of projects related to photo- and electrocatalytic systems, studying electronic transport and catalyst stability through ultrathin ALD oxide films for organic and inorganic heterogeneous catalyst systems. Publications resulting from these works are listed in Appendix A.

APPENDIX A. Co-Authored Publications

Diphenylisobenzofuran Bound to Nanocrystalline Metal Oxides: Excimer Formation, Singlet Fission, Electron Injection, and Low Energy Sensitization

Tanmay Banerjee[†], Sean P. Hill[†], M. Alejandra Hermosilla-Palacios[‡], **Brandon D. Piercy**[‖], Jess Haney[†], Bryan Casale[†], A. Eugene DePrince III[†], Mark D. Losego[‖], Valeria D. Kleiman[‡], Kenneth Hanson[†]

[†]Department of Chemistry and Biochemistry, Florida State University, Tallahassee, Florida 32306, United States
[‡]Department of Chemistry, University of Florida, PO BOX 117200, Gainesville, Florida 32611-7200, United States
[‖]School of Materials Science and Engineering, Georgia Institute of Technology, Love Manufacturing Building, 771 Ferst Drive NW, Atlanta, Georgia 30332, United States

J. Phys. Chem. C. 2018, 122, 50, 28478-28490.

We report the photophysical properties of the dicarboxylated diphenylisobenzofuran dye (1) bound to nanocrystalline metal oxide surfaces. With increased surface loading of 1, emission from the films is significantly quenched but with a small amount of excimer emission at maximum surface loadings. Long-lived triplets were observed by ns TA spectroscopy that are consistent with singlet fission occurring on mesoporous ZrO_2. The evolution of these triplets, however, could not be convincingly resolved by our subnanosecond TA spectroscopy. Dye-sensitized devices composed of 1 on a $TiO_2|Al_2O_3$ core–shell structure exhibited an unusual decrease, increase, and then decrease in Jsc with respect to the thickness of Al_2O_3. In these films the Al_2O_3 acts as a tunneling barrier to slow electron injection from the singlet excited state such that singlet fission, and electron injection from the triplet state becomes competitive. Proof-of-principle self-assembled bilayer films that exhibit efficient triplet energy transfer from a low energy absorbing dye to 1 is demonstrated as another step toward a SF-based DSSC that can circumvent the Shockley–Queisser limit.

Effects of Al_2O_3 atomic layer deposition on interfacial structure and electron transfer dynamics at Re-bipyridyl complex/TiO_2 interfaces

Jia Song[†], Aimin Ge[†], **Brandon Piercy**[‡], Mark D. Losego[‡], Tianquan Lian[†]

[†]Department of Chemistry, Emory University, 1515 Dickey Drive, Atlanta, Georgia 30322, United States
[‡]School of Materials Science and Engineering, Georgia Institute of Technology, Love Manufacturing Building, 771 Ferst Drive NW, Atlanta, Georgia 30332, United States

Chem. Phys. 2018, 512, 68-74.

Atomic layer deposition (ALD) of oxide layers on sensitizer- and/or catalyst-functionalized semiconductor surfaces have been used to improve the stability of dye-sensitized solar cells and photoelectrosynthesis cells. However, how the ALD layer affects the interfacial structure of adsorbed molecules and interfacial electron transfer dynamics is still unclear. Herein, we investigated the effects of ALD of Al_2O_3 on adsorption structure of Re bipyridyl complex on TiO_2 nanocrystalline films and rutile (001) single crystals by IR absorption and sum frequency generation spectroscopy. Further, the electron transfer dynamics between the Re complex and TiO_2 film was also examined by ultrafast infrared transient absorption spectroscopy. Our results show that the electron injection yield decreases with the increase of ALD layer thickness.

Stabilization of Polyoxometalate Water Oxidation Catalysts on Hematite by Atomic Layer Deposition

Sarah M. Lauinger[†], **Brandon D. Piercy**[‡], Wei Li[*], Qiushi Yin[†], Daniel L. Collins-Wildman[†], Elliot N. Glass[†], Mark D. Losego[‡], Dunwei Wang[*], Yurii V. Geletii[†], Craig L. Hill[†]

[†]Department of Chemistry, Emory University, 1515 Dickey Drive, Atlanta, Georgia 30322, United States
‡ School of Materials Science and Engineering, Georgia Institute of Technology, Love Manufacturing Building, 771 Ferst Drive NW, Atlanta, Georgia 30332, United States
* Department of Chemistry, Merkert Chemistry Center, Boston College, 2609 Beacon Street, Chestnut Hill, Massachusetts 02467, United States

ACS Appl. Mater. Interfaces 2017, 9, 40, 35048-35056

Fast and earth-abundant-element polyoxometalates (POMs) have been heavily studied recently as water oxidation catalysts (WOCs) in homogeneous solution. However, POM WOCs can be quite unstable when supported on electrode or photoelectrode surfaces under applied potential. This article reports for the first time that a nanoscale oxide coating (Al_2O_3) applied by the atomic layer deposition (ALD) aids immobilization and greatly stabilizes this now large family of molecular WOCs when on electrode surfaces. In this study, $[(Ru^{IV}_4(OH)_2(H_2O)_4)(\gamma\text{-}SiW_{10}O_{34})_2]_{10}$–**($Ru_4Si_2$)** is supported on hematite photoelectrodes and then protected by ALD Al_2O_3; this ternary system was characterized before and after photoelectrocatalytic water oxidation by Fourier transform infrared, X-ray photoelectron spectroscopy, energy-dispersive X-ray, and voltammetry. All these studies indicate that Ru_4Si_2 remains intact with Al_2O_3 ALD protection, but not without. The thickness of the Al_2O_3 layer significantly affects the catalytic performance of the system: a 4 nm thick Al_2O_3 layer provides optimal performance with nearly 100% faradaic efficiency for oxygen generation under visible-light illumination. Al_2O_3 layers thicker than 6.5 nm appear to completely bury the **Ru_4Si_2** catalyst, removing all of the catalytic activity, whereas thinner layers are insufficient to maintain a long-term attachment of the catalytic POM.

Effect of Surface Ligand on Charge Separation and Recombination at $CsPbI_3$ Perovskite Quantum Dot/ TiO_2 Interfaces

Qiongyi Shang[†], **Brandon Piercy**[‡], Mark D. Losego[‡], and Tianquan Lian[†]

[†]Department of Chemistry, Emory University, 1515 Dickey Drive, Atlanta, Georgia 30322, United States
[‡]School of Materials Science and Engineering, Georgia Institute of Technology, Love Manufacturing Building, 771 Ferst Drive NW, Atlanta, Georgia 30332, United States

J. Phys. Chem. C, 2019, 123, 35, 21415-21421

$CsPbI_3$ perovskite quantum dot (QD) solar cells are a promising device platform for further development due to their improved stability compared to bulk materials. The fabrication of these devices often involves post-synthetic washing of colloidal QDs to remove surface ligands. Herein, we investigate how this post-synthetic treatment affects the charge separation (CS) and charge recombination (CR) processes at the interface of $CsPbI_3$ QDs and the TiO_2 electron extraction layer. The CS time constant at QD/TiO_2 interface decrease from 457 ± 4 ps for QDs directly deposited on TiO_2 to 288 ± 1 ps for QDs that were washed twice by methyl acetate, increasing the ET efficiency from 89.9 ± 0.3% to 98.3 ± 0.01%. Interestingly, this treatment also lengthens the average charge recombination time constants from 346 ± 18 ns to 1180 ± 60 ns, which is also beneficial for reducing charge recombination loss. This result demonstrates pronounced effect of QD washing by methyl acetate (MeOAc) on interfacial charge transfer processes, suggesting the important effect of post-synthesis modification of colloidal perovskite QDs on solar cell efficiencies.

Characterization of Electronic Transport through Amorphous TiO_2 Produced by Atomic-Layer Deposition

Paul Nunez,[†] Matthias H. Richter,[†] **Brandon D. Piercy**,[‡] Christopher W. Roske,[†] Miguel Cabań-Acevedo,[†]Mark D. Losego,[‡] Steven J. Konezny,[*,§,∥] David J. Fermin,[⊥] Shu Hu,[*,§,#] Bruce S. Brunschwig,[¶] and Nathan S. Lewis[*,†,¶]

[†]Division of Chemistry and Chemical Engineering and [¶]Beckman Institute and Molecular Materials Research Center, California Institute of Technology, Pasadena, California 91125, United States

[‡]School of Materials Science and Engineering, Georgia Institute of Technology, Atlanta, Georgia 30332, United States

[§]Energy Sciences Institute, Yale West Campus, West Haven, Connecticut 06516, United States [∥]Department of Chemistry, Yale University, 225 Prospect Street, P.O. Box 208107, New Haven, Connecticut 06520-8107, United States

[⊥]School of Chemistry, University of Bristol, Cantock's Close, Bristol BS8 1TS, U.K.

[#]Department of Chemical and Environmental Engineering, School of Engineering and Applied Sciences, Yale University, New Haven, Connecticut 06520, United States

J. Phys. Chem. C 2019, 123, 33, 20116-20129

Electrical transport in amorphous titanium dioxide (a-TiO_2) thin films, deposited by atomic layer deposition (ALD), and across heterojunctions of p^+-Si|a-TiO_2|metal substrates that had various top metal contacts has been characterized by ac conductivity, temperature-dependent dc conductivity, space-charge-limited current spectroscopy, electron para-magnetic resonance (EPR) spectroscopy, X-ray photoelectron spectroscopy, and current density versus voltage (J−V) characteristics. Amorphous TiO_2 films were fabricated using either tetrakis(dimethylamido)-titanium with a substrate temperature of 150 °C or $TiCl_4$ with a substrate temperature of 50, 100, or 150 °C. EPR spectroscopy of the films showed that the Ti^{3+} concentration varied with the deposition conditions and increases in the concentration of Ti^{3+} in the films correlated with increases in film conductivity. Valence band spectra for the a-TiO_2 films exhibited a defect-state peak below the conduction band minimum (CBM) and increases in the intensity of this peak correlated with increases in the Ti^{3+} concentration measured by EPR as well as with

increases in film conductivity. The temperature- dependent conduction data showed Arrhenius behavior at room temperature with an activation energy that decreased with decreasing temperature, suggesting that conduction did not occur primarily through either the valence or conduction bands. The data from all of the measurements are consistent with a Ti^{3+} defect-mediated transport mode involving a hopping mechanism with a defect density of 10^{19} cm^{-3}, a 0.83 wide defect band centered 1.47 eV below the CBM, and a free-electron concentration of 10^{16} cm^{-3}. The data are consistent with substantial room-temperature anodic conductivity resulting from the introduction of defect states during the ALD fabrication process as opposed to charge transport intrinsically associated with the conduction band of TiO_2.

REFERENCES

1. Suntola, T., Atomic Layer Epitaxy. *Materials Science Reports* **1989**, *4*, 261-312.
2. Lujala, V.; Skarp, J.; Tammenmaa, M.; Suntola, T., Atomic Layer Epitaxy Growth of Doped Zinc Oxide Thin Films from Organometals. *Appl. Surf. Sci.* **1994**, *82*, 34-40.
3. Suntola, T.; Antson, J., Method for Producing Compound Thin Films. Google Patents: 1977.
4. Jõgi, I.; Kukli, K.; Ritala, M.; Leskelä, M.; Aarik, J.; Aidla, A.; Lu, J., Atomic Layer Deposition of High Capacitance Density Ta2o5–Zro2 Based Dielectrics for Metal–Insulator–Metal Structures. *Microelectron. Eng.* **2010**, *87*, 144-149.
5. Xie, Q.; Jiang, Y.-L.; Detavernier, C.; Deduytsche, D.; Van Meirhaeghe, R. L.; Ru, G.-P.; Li, B.-Z.; Qu, X.-P., Atomic Layer Deposition of Tio2 from Tetrakis-Dimethyl-Amido Titanium or Ti Isopropoxide Precursors and H2o. *J. Appl. Phys.* **2007**, *102*, 083521.
6. Nabatame, T., et al. In *Design and Proof of High Quality Hfalo/Sub X/ Film Formation for Moscaps and Nmosfets through Layer-by-Layer Deposition and Annealing Process*, 2003 Symposium on VLSI Technology. Digest of Technical Papers (IEEE Cat. No.03CH37407), 10-12 June 2003; 2003; pp 25-26.
7. Dutta, S.; Leeladhar; Pandey, A.; Thakur, O. P.; Pal, R., Electrical Properties of Ultrathin Titanium Dioxide Films on Silicon. *Journal of Vacuum Science & Technology A* **2015**, *33*, 021507.
8. Colon, A.; Stan, L.; Divan, R.; Shi, J., Investigating Compositional Effects of Atomic Layer Deposition Ternary Dielectric Ti-Al-O on Metal-Insulator-Semiconductor Heterojunction Capacitor Structure for Gate Insulation of Inaln/Gan and Algan/Gan. *Journal of Vacuum Science & Technology B* **2016**, *34*, 06K901.
9. Gaskins, J. T., et al., Review—Investigation and Review of the Thermal, Mechanical, Electrical, Optical, and Structural Properties of Atomic Layer Deposited High-K Dielectrics: Beryllium Oxide, Aluminum Oxide, Hafnium Oxide, and Aluminum Nitride. *ECS J. Solid State Sci. Technol.* **2017**, *6*, N189-N208.
10. Meng, X.; Wang, X.; Geng, D.; Ozgit-Akgun, C.; Schneider, N.; Elam, J. W., Atomic Layer Deposition for Nanomaterials Synthesis and Functionalization in Energy Technology. *Materials Horizons* **2017**.
11. Wei Seh, Z.; Li, W.; Cha, J. J.; Zheng, G.; Yang, Y.; McDowell, M. T.; Hsu, P.-C.; Cui, Y., Sulphur–Tio2 Yolk–Shell Nanoarchitecture with Internal Void Space for Long-Cycle Lithium–Sulphur Batteries. *Nature Communications* **2013**, *4*, 1331.
12. Jung, Y. S.; Cavanagh, A. S.; Riley, L. A.; Kang, S.-H.; Dillon, A. C.; Groner, M. D.; George, S. M.; Lee, S.-H., Ultrathin Direct Atomic Layer Deposition on Composite Electrodes for Highly Durable and Safe Li-Ion Batteries. *Adv. Mater.* **2010**, *22*, 2172-2176.
13. Hyde, G. K.; Stewart, S. M.; Scarel, G.; Parsons, G. N.; Shih, C. C.; Shih, C. M.; Lin, S. J.; Su, Y. Y.; Monteiro-Riviere, N. A.; Narayan, R. J., Atomic Layer Deposition of Titanium Dioxide on Cellulose Acetate for Enhanced Hemostasis. *Biotechnology Journal* **2011**, *6*, 213-223.

14. Hanson, C. A.; Oldham, C. J.; Parsons, G. N., Paper Deacidification and Uv Protection Using Zno Atomic Layer Deposition. *Journal of Vacuum Science & Technology A* **2012**, *30*, 5.
15. Miikkulainen, V.; Leskelä, M.; Ritala, M.; Puurunen, R. L., Crystallinity of Inorganic Films Grown by Atomic Layer Deposition: Overview and General Trends. *J. Appl. Phys.* **2013**, *113*, 021301.
16. Puurunen, R. L., Surface Chemistry of Atomic Layer Deposition: A Case Study for the Trimethylaluminum/Water Process. *J. Appl. Phys.* **2005**, *97*, 121301.
17. AtomicLimits, Atomiclimits Ald Database. 2019.
18. George, S. M., Atomic Layer Deposition: An Overview. *Chem. Rev.* **2010**, *110*, 111-131.
19. Johnson, R. W.; Hultqvist, A.; Bent, S. F., A Brief Review of Atomic Layer Deposition: From Fundamentals to Applications. *Mater. Today* **2014**, *17*, 236-246.
20. Niemelä, J.-P.; Marin, G.; Karppinen, M., Titanium Dioxide Thin Films by Atomic Layer Deposition: A Review. *Semicond. Sci. Technol.* **2017**, *32*, 093005.
21. Tommi, T.; Maarit, K., Atomic Layer Deposition of Zno: A Review. *Semicond. Sci. Technol.* **2014**, *29*, 043001.
22. Vandalon, V.; Kessels, W. M. M., Revisiting the Growth Mechanism of Atomic Layer Deposition of Al2o3: A Vibrational Sum-Frequency Generation Study. *Journal of Vacuum Science & Technology A* **2017**, *35*, 05C313.
23. Dingemans, G.; Kessels, W. M. M., Status and Prospects of Al2o3-Based Surface Passivation Schemes for Silicon Solar Cells. *Journal of Vacuum Science & Technology A* **2012**, *30*, 040802.
24. Vandalon, V.; Kessels, W. M. M., What Is Limiting Low-Temperature Atomic Layer Deposition of Al2o3? A Vibrational Sum-Frequency Generation Study. *Appl. Phys. Lett.* **2016**, *108*, 011607.
25. Song, J.; Ge, A.; Piercy, B.; Losego, M. D.; Lian, T., Effects of Al2o3 Atomic Layer Deposition on Interfacial Structure and Electron Transfer Dynamics at Re-Bipyridyl Complex/Tio2 Interfaces. *Chem. Phys.* **2018**, *512*, 68-74.
26. DeCoster, M. E., et al., Density and Size Effects in Amorphous Al2o3 and Tio2 Thin Films. *Thin Solid Films*.
27. Vanderbilt, D.; Zhao, X.; Ceresoli, D., Structural and Dielectric Properties of Crystalline and Amorphous Zro2. *Thin Solid Films* **2005**, *486*, 125-128.
28. Sayan, S., et al., Structural, Electronic, and Dielectric Properties of Ultrathin Zirconia Films on Silicon. *Appl. Phys. Lett.* **2005**, *86*, 152902.
29. Feinberg, A.; Perry, C. H., Structural Disorder and Phase Transitions in Zro2-Y2o3 System. *J. Phys. Chem. Solids* **1981**, *42*, 513-518.
30. Kukli, K.; Ihanus, J.; Ritala, M.; Leskela, M., Tailoring the Dielectric Properties of Hfo2–Ta2o5 Nanolaminates. *Appl. Phys. Lett.* **1996**, *68*, 3737-3739.
31. Zhao, X.; Vanderbilt, D., Phonons and Lattice Dielectric Properties of Zirconia. *Physical Review B* **2002**, *65*, 075105.
32. Aarik, J.; Aidla, A.; Kiisler, A.-A.; Uustare, T.; Sammelselg, V., Effect of Crystal Structure on Optical Properties of Tio2 Films Grown by Atomic Layer Deposition. *Thin Solid Films* **1997**, *305*, 270-273.

33. Aarik, J.; Aidla, A.; Mändar, H.; Sammelselg, V., Anomalous Effect of Temperature on Atomic Layer Deposition of Titanium Dioxide. *J. Cryst. Growth* **2000**, *220*, 531-537.
34. Aarik, J.; Aidla, A.; Mändar, H.; Uustare, T., Atomic Layer Deposition of Titanium Dioxide from Ticl4 and H2o: Investigation of Growth Mechanism. *Appl. Surf. Sci.* **2001**, *172*, 148-158.
35. Aarik, J.; Aidla, A.; Uustare, T.; Sammelselg, V., Morphology and Structure of Tio2 Thin Films Grown by Atomic Layer Deposition. *J. Cryst. Growth* **1995**, *148*, 268-275.
36. Kukli, K.; Ritala, M.; Aarik, J.; Uustare, T.; Leskelä, M., Influence of Growth Temperature on Properties of Zirconium Dioxide Films Grown by Atomic Layer Deposition. *J. Appl. Phys.* **2002**, *92*, 1833-1840.
37. Kim, H.; McIntyre, P. C.; Saraswat, K. C., Microstructural Evolution of Zro2–Hfo2 Nanolaminate Structures Grown by Atomic Layer Deposition. *J. Mater. Res.* **2004**, *19*, 643-650.
38. Liu, J.; Li, J.; Wu, J.; Sun, J., Structure and Dielectric Property of High-K Zro2 Films Grown by Atomic Layer Deposition Using Tetrakis(Dimethylamido)Zirconium and Ozone. *Nanoscale Research Letters* **2019**, *14*, 154.
39. Cho, H.; Park, K.-W.; Park, C. H.; Cho, H. J.; Yeom, S.-J.; Hong, K.; Kwak, N.-J.; Ahn, J.-H., Abnormally Enhanced Dielectric Constant in Zro2/Ta2o5 Multi-Laminate Structures by Metallic Ta Formation. *Mater. Lett.* **2015**, *154*, 148-151.
40. Kukli, K.; Kemell, M.; Vehkamäki, M.; Heikkilä, M. J.; Mizohata, K.; Kalam, K.; Ritala, M.; Leskelä, M.; Kundrata, I.; Fröhlich, K., Atomic Layer Deposition and Properties of Mixed Ta2o5 and Zro2 Films. *AIP Advances* **2017**, *7*, 025001.
41. Kim, H.; Saraswat, K. C.; McIntyre, P. C., Comparative Study on Electrical and Microstructural Characteristics of Zro2 and Hfo2 Grown by Atomic Layer Deposition. *J. Mater. Res.* **2005**, *20*, 3125-3132.
42. Sønsteby, H. H.; Fjellvåg, H.; Nilsen, O., Functional Perovskites by Atomic Layer Deposition – an Overview. *Advanced Materials Interfaces* **2017**, *4*, 1600903.
43. Lujala, V.; Skarp, J.; Tammenmaa, M.; Suntola, T., Atomic Layer Epitaxy Growth of Doped Zinc Oxide Thin Films from Organometals. *Appl. Surf. Sci.* **1994**, *82-83*, 34-40.
44. Yen, K.-Y.; Chiu, C.-H.; Hsiao, C.-Y.; Li, C.-W.; Chou, C.-H.; Lo, K.-Y.; Chen, T.-P.; Lin, C.-H.; Lin, T.-Y.; Gong, J.-R., Characteristics of Gan-Based Leds Using Ga-Doped or in-Doped Zno Transparent Conductive Layers Grown by Atomic Layer Deposition. *J. Cryst. Growth* **2014**, *387*, 91-95.
45. Illiberi, A.; Scherpenborg, R.; Theelen, M.; Poodt, P.; Roozeboom, F., On the Environmental Stability of Zno Thin Films by Spatial Atomic Layer Deposition. *Journal of Vacuum Science & Technology A* **2013**, *31*, 061504.
46. Ott, A. W.; Chang, R. P. H., Atomic Layer-Controlled Growth of Transparent Conducting Zno on Plastic Substrates. *Mater. Chem. Phys.* **1999**, *58*, 132-138.
47. Dasgupta, N. P.; Neubert, S.; Lee, W.; Trejo, O.; Lee, J.-R.; Prinz, F. B., Atomic Layer Deposition of Al-Doped Zno Films: Effect of Grain Orientation on Conductivity. *Chem. Mater.* **2010**, *22*, 4769-4775.

48. Kong, B. H.; Choi, M. K.; Cho, H. K.; Kim, J. H.; Baek, S.; Lee, J.-H., Conformal Coating of Conductive Zno: Al Films as Transparent Electrodes on High Aspect Ratio Si Microrods. *Electrochem. Solid-State Lett.* **2010**, *13*, K12-K14.
49. Elam, J. W.; George, S. M., Growth of Zno/Al2o3 Alloy Films Using Atomic Layer Deposition Techniques. *Chem. Mater.* **2003**, *15*, 1020-1028.
50. McDaniel, M. D.; Ngo, T. Q.; Hu, S.; Posadas, A.; Demkov, A. A.; Ekerdt, J. G., Atomic Layer Deposition of Perovskite Oxides and Their Epitaxial Integration with Si, Ge, and Other Semiconductors. *Applied Physics Reviews* **2015**, *2*, 041301.
51. Falmbigl, M., et al., Batio3 Thin Films from Atomic Layer Deposition: A Superlattice Approach. *The Journal of Physical Chemistry C* **2017**, *121*, 16911-16920.
52. Kwon, O. S.; Lee, S. W.; Han, J. H.; Hwang, C. S., Atomic Layer Deposition and Electrical Properties of Srtio3 Thin Films Grown Using Sr (C11h19o2) 2, Ti (Oi-C3h7) 4, and H2o. *J. Electrochem. Soc.* **2007**, *154*, G127-G133.
53. Plokhikh, A. V.; Karateev, I. A.; Falmbigl, M.; Vasiliev, A. L.; Lapano, J.; Engel-Herbert, R.; Spanier, J. E., Toward a Low-Temperature Route for Epitaxial Integration of Bifeo3 on Si. *The Journal of Physical Chemistry C* **2019**, *123*, 12203-12210.
54. Watanabe, T.; Hoffmann-Eifert, S.; Peter, F.; Mi, S.; Jia, C.; Hwang, C. S.; Waser, R., Liquid Injection Ald of Pb (Zr , Ti) O X Thin Films by a Combination of Self-Regulating Component Oxide Processes. *J. Electrochem. Soc.* **2007**, *154*, G262-G269.
55. Watanabe, T.; Hoffmann-Eifert, S.; Hwang, C. S.; Waser, R., Growth Behavior of Atomic-Layer-Deposited Pb (Zr , Ti) O X Thin Films on Planar Substrate and Three-Dimensional Hole Structures. *J. Electrochem. Soc.* **2008**, *155*, D715-D722.
56. Zhang, F.; Perng, Y.-C.; Choi, J. H.; Wu, T.; Chung, T.-K.; Carman, G. P.; Locke, C.; Thomas, S.; Saddow, S. E.; Chang, J. P., Atomic Layer Deposition of Pb(Zr,Ti)Ox on 4h-Sic for Metal-Ferroelectric-Insulator-Semiconductor Diodes. *J. Appl. Phys.* **2011**, *109*, 124109.
57. Choi, J. H.; Zhang, F.; Perng, Y.-C.; Chang, J. P., Tailoring the Composition of Lead Zirconate Titanate by Atomic Layer Deposition. *Journal of Vacuum Science & Technology B* **2013**, *31*, 012207.
58. Sbrockey, N. M.; Tompa, G. S.; Lavelle, R.; Trumbull, K. A.; Fanton, M. A.; Snyder, D. W.; Polcawich, R. G.; Potrepka, D. M., Atomic Layer Deposition of Pbtio3 and Pbzrxti1-Xo3 Films Using Metal Alkyl and Alkylamide Precursors. *Journal of Vacuum Science & Technology A* **2018**, *36*, 031509.
59. Yang, J. I.; Welsh, A.; Sbrockey, N. M.; Tompa, G. S.; Polcawich, R. G.; Potrepka, D. M.; Trolier-McKinstry, S., Annealing Behavior and Electrical Properties of Atomic Layer Deposited Pbtio3 and Pzt Films. *J. Cryst. Growth* **2018**, *493*, 45-50.
60. Strnad, N. A.; Potrepka, D. M.; Pulskamp, J. S.; Liu, Y.; Jones, J. L.; Phaneuf, R. J.; Polcawich, R. G., Texture and Phase Variation of Ald Pbtio3 Films Crystallized by Rapid Thermal Anneal. *Journal of Vacuum Science & Technology A* **2019**, *37*, 020917.
61. Strnad, N. A. Atomic Layer Deposition of Lead Zirconate-Titanate and Other Lead-Based Perovskites. 2019.
62. Conley, J. F.; Ono, Y.; Tweet, D. J., Densification and Improved Electrical Properties of Pulse-Deposited Films Via in Situ Modulated Temperature Annealing. *Appl. Phys. Lett.* **2004**, *84*, 1913-1915.

63. Conley Jr, J. F.; Ono, Y.; Stecker, G. M., Modulated Temperature Method of Atomic Layer Deposition (Ald) of High Dielectric Constant Films. Google Patents: 2008.
64. Langston, M. C.; Dasgupta, N. P.; Jung, H. J.; Logar, M.; Huang, Y.; Sinclair, R.; Prinz, F. B., In Situ Cycle-by-Cycle Flash Annealing of Atomic Layer Deposited Materials. *J. Phys. Chem. C* **2012**, *116*, 24177-24183.
65. Henke, T.; Knaut, M.; Hossbach, C.; Geidel, M.; Albert, M.; Bartha, J. W., Growth of Aluminum Oxide Thin Films with Enhanced Film Density by the Integration of in Situ Flash Annealing into Low-Temperature Atomic Layer Deposition. *Surf. Coat. Technol.* **2017**, *309*, 600-608.
66. Henke, T.; Knaut, M.; Hossbach, C.; Geidel, M.; Rebohle, L.; Albert, M.; Skorupa, W.; Bartha, J. W., Flash-Enhanced Atomic Layer Deposition: Basics, Opportunities, Review, and Principal Studies on the Flash-Enhanced Growth of Thin Films. *ECS J. Solid State Sci. Technol.* **2015**, *4*, P277-P287.
67. Piercy, B. D.; Losego, M. D., Tree-Based Control Software for Multilevel Sequencing in Thin Film Deposition Applications. *J. Vac. Sci. Technol., B* **2015**, *33*, 043201.
68. Tompkins, H. G.; Hilfiker, J. N., *Spectroscopic Ellipsometry : Practical Application to Thin Film Characterization*; Momentum Press: New York, [New York] [222 East 46th Street, New York, NY 10017], 2016.
69. Renaud, G., Oxide Surfaces and Metal/Oxide Interfaces Studied by Grazing Incidence X-Ray Scattering. *Surf. Sci. Rep.* **1998**, *32*, 5-90.
70. Chason, E.; Mayer, T. M., Thin Film and Surface Characterization by Specular X-Ray Reflectivity. *Crit. Rev. Solid State Mater. Sci.* **1997**, *22*, 1-67.
71. Triboulet, R.; Perrière, J., Epitaxial Growth of Zno Films. *Prog. Cryst. Growth Charact. Mater.* **2003**, *47*, 65-138.
72. Tricot, S.; Nistor, M.; Millon, E.; Boulmer-Leborgne, C.; Mandache, N. B.; Perrière, J.; Seiler, W., Epitaxial Zno Thin Films Grown by Pulsed Electron Beam Deposition. *Surf. Sci.* **2010**, *604*, 2024-2030.
73. Millon, E.; Albert, O.; Loulergue, J. C.; Etchepare, J.; Hulin, D.; Seiler, W.; Perrière, J., Growth of Heteroepitaxial Zno Thin Films by Femtosecond Pulsed-Laser Deposition. *J. Appl. Phys.* **2000**, *88*, 6937-6939.
74. Arthur, J. R., Molecular Beam Epitaxy. *Surf. Sci.* **2002**, *500*, 189-217.
75. Haspert, L. C.; Banerjee, P.; Henn-Lecordier, L.; Rubloff, G. W., Correlation of Raman, Electrical, and Optical Properties of High-K, Atomic Layer Deposited Al-Doped Tio2. *Journal of Vacuum Science & Technology B* **2011**, *29*, 041807.
76. Zhang, W. F.; He, Y. L.; Zhang, M. S.; Yin, Z.; Chen, Q., Raman Scattering Study on Anatase Tio 2 Nanocrystals. *J. Phys. D: Appl. Phys.* **2000**, *33*, 912.
77. Niilisk, A.; Moppel, M.; Pärs, M.; Sildos, I.; Jantson, T.; Avarmaa, T.; Jaaniso, R.; Aarik, J., Structural Study of Tio2 Thin Films by Micro-Raman Spectroscopy. *Open Physics* **2006**, *4*, 105-116.
78. Benninghoven, A., Chemical Analysis of Inorganic and Organic Surfaces and Thin Films by Static Time-of-Flight Secondary Ion Mass Spectrometry (Tof-Sims). *Angewandte Chemie International Edition in English* **1994**, *33*, 1023-1043.
79. Losego, M. D.; Grady, M. E.; Sottos, N. R.; Cahill, D. G.; Braun, P. V., Effects of Chemical Bonding on Heat Transport across Interfaces. *Nature Materials* **2012**, *11*, 502-506.

80. Cahill, D. G., Analysis of Heat Flow in Layered Structures for Time-Domain Thermoreflectance. *Rev. Sci. Instrum.* **2004**, *75*, 5119-5122.
81. Wilson, R. B.; Cahill, D. G., Anisotropic Failure of Fourier Theory in Time-Domain Thermoreflectance Experiments. *Nature Communications* **2014**, *5*.
82. Cahill, D. G.; Ford, W. K.; Goodson, K. E.; Mahan, G. D.; Majumdar, A.; Maris, H. J.; Merlin, R.; Phillpot, S. R., Nanoscale Thermal Transport. *J. Appl. Phys.* **2003**, *93*, 793-818.
83. Dingle, R.; Wiegmann, W.; Henry, C. H., Quantum States of Confined Carriers in Very Thin ${\Mathrm{Al}}_{X}{\Mathrm{Ga}}_{1-X}\Mathrm{as}$-Gaas-${\Mathrm{Al}}_{X}{\Mathrm{Ga}}_{1-X}\Mathrm{as}$ Heterostructures. *Phys. Rev. Lett.* **1974**, *33*, 827-830.
84. Costescu, R. M.; Cahill, D. G.; Fabreguette, F. H.; Sechrist, Z. A.; George, S. M., Ultra-Low Thermal Conductivity in W/Al2o3 Nanolaminates. *Science* **2004**, *303*, 989-990.
85. Podsiadlo, P., et al., Lbl Assembled Laminates with Hierarchical Organization from Nano- to Microscale: High-Toughness Nanomaterials and Deformation Imaging. *ACS Nano* **2009**, *3*, 1564-1572.
86. Szeghalmi, A.; Senz, S.; Bretschneider, M.; Gösele, U.; Knez, M., All Dielectric Hard X-Ray Mirror by Atomic Layer Deposition. *Appl. Phys. Lett.* **2009**, *94*, 133111.
87. Leng, C. Z.; Losego, M. D., Vapor Phase Infiltration (Vpi) for Transforming Polymers into Organic–Inorganic Hybrid Materials: A Critical Review of Current Progress and Future Challenges. *Materials Horizons* **2017**, *4*, 747-771.
88. Selvaraj, S. K.; Takoudis, C. G., Scalable Control Program for Multiprecursor Flow-Type Atomic Layer Deposition System. *J. Vac. Sci. Technol., A* **2015**, *33*, 013201.
89. Wirth, N., *Algorithms + Data Structures = Programs*, 1st edition ed.; Prentice Hall: Englewood Cliffs, N.J, 1976, p 366.
90. Bagnell, J. A., et al. In *An Integrated System for Autonomous Robotics Manipulation*, 2012 IEEE/RSJ International Conference on Intelligent Robots and Systems (IROS), October 2012; 2012; pp 2955-2962.
91. Champandard, A. J.; Dunstan, P., The Behavior Tree Starter Kit. *Game AI Pro: Collected Wisdom of Game AI Professionals* **2013**, 72-92.
92. Nicolau, M.; Perez-Liebana, D.; O'Neill, M.; Brabazon, A., Evolutionary Behavior Tree Approaches for Navigating Platform Games. *IEEE Transactions on Computational Intelligence and AI in Games* **2017**, *9*, 227-238.
93. Khorasaninejad, M.; Chen, W. T.; Devlin, R. C.; Oh, J.; Zhu, A. Y.; Capasso, F., Metalenses at Visible Wavelengths: Diffraction-Limited Focusing and Subwavelength Resolution Imaging. *Science* **2016**, *352*, 1190-1194.
94. Li, D.; Carette, M.; Granier, A.; Landesman, J. P.; Goullet, A., Spectroscopic Ellipsometry Analysis of Tio2 Films Deposited by Plasma Enhanced Chemical Vapor Deposition in Oxygen/Titanium Tetraisopropoxide Plasma. *Thin Solid Films* **2012**, *522*, 366-371.
95. Saha, D.; Ajimsha, R. S.; Rajiv, K.; Mukherjee, C.; Gupta, M.; Misra, P.; Kukreja, L. M., Spectroscopic Ellipsometry Characterization of Amorphous and Crystalline Tio2 Thin Films Grown by Atomic Layer Deposition at Different Temperatures. *Appl. Surf. Sci.* **2014**, *315*, 116-123.

96. Tang, H.; Prasad, K.; Sanjinès, R.; Schmid, P. E.; Lévy, F., Electrical and Optical Properties of Tio2 Anatase Thin Films. *J. Appl. Phys.* **1994**, *75*, 2042-2047.
97. Zhang, M.; Lin, G.; Dong, C.; Wen, L., Amorphous Tio2 Films with High Refractive Index Deposited by Pulsed Bias Arc Ion Plating. *Surf. Coat. Technol.* **2007**, *201*, 7252-7258.
98. McDowell, M. T.; Lichterman, M. F.; Carim, A. I.; Liu, R.; Hu, S.; Brunschwig, B. S.; Lewis, N. S., The Influence of Structure and Processing on the Behavior of Tio2 Protective Layers for Stabilization of N-Si/Tio2/Ni Photoanodes for Water Oxidation. *ACS Appl. Mater. Interfaces* **2015**, *7*, 15189-15199.
99. Hu, S.; Shaner, M. R.; Beardslee, J. A.; Lichterman, M.; Brunschwig, B. S.; Lewis, N. S., Amorphous Tio2 Coatings Stabilize Si, Gaas, and Gap Photoanodes for Efficient Water Oxidation. *Science* **2014**, *344*, 1005-1009.
100. Pham, H. H.; Wang, L.-W., Oxygen Vacancy and Hole Conduction in Amorphous Tio2. *PCCP* **2014**, *17*, 541-550.
101. Alibabaei, L.; Brennaman, M. K.; Norris, M. R.; Kalanyan, B.; Song, W.; Losego, M. D.; Concepcion, J. J.; Binstead, R. A.; Parsons, G. N.; Meyer, T. J., Solar Water Splitting in a Molecular Photoelectrochemical Cell. *Proceedings of the National Academy of Sciences* **2013**, *110*, 20008-20013.
102. Amano, F.; Nakata, M.; Yamamoto, A.; Tanaka, T., Effect of Ti3+ Ions and Conduction Band Electrons on Photocatalytic and Photoelectrochemical Activity of Rutile Titania for Water Oxidation. *The Journal of Physical Chemistry C* **2016**, *120*, 6467-6474.
103. Banerjee, S.; Dionysiou, D. D.; Pillai, S. C., Self-Cleaning Applications of Tio2 by Photo-Induced Hydrophilicity and Photocatalysis. *Applied Catalysis B: Environmental* **2015**, *176–177*, 396-428.
104. Cao, F.; Xiong, J.; Wu, F.; Liu, Q.; Shi, Z.; Yu, Y.; Wang, X.; Li, L., Enhanced Photoelectrochemical Performance from Rationally Designed Anatase/Rutile Tio2 Heterostructures. *ACS Appl. Mater. Interfaces* **2016**, *8*, 12239-12245.
105. Chen, Y. W.; Prange, J. D.; Dühnen, S.; Park, Y.; Gunji, M.; Chidsey, C. E. D.; McIntyre, P. C., Atomic Layer-Deposited Tunnel Oxide Stabilizes Silicon Photoanodes for Water Oxidation. *Nature Materials* **2011**, *10*, 539-544.
106. Cheng, H.-E.; Chen, C.-C., Morphological and Photoelectrochemical Properties of Ald Tio2 Films. *J. Electrochem. Soc.* **2008**, *155*, D604-D607.
107. Kelly, C. A.; Farzad, F.; Thompson, D. W.; Stipkala, J. M.; Meyer, G. J., Cation-Controlled Interfacial Charge Injection in Sensitized Nanocrystalline Tio2. *Langmuir* **1999**, *15*, 7047-7054.
108. Kim, I. S.; Haasch, R. T.; Cao, D. H.; Farha, O. K.; Hupp, J. T.; Kanatzidis, M. G.; Martinson, A. B. F., Amorphous Tio2 Compact Layers Via Ald for Planar Halide Perovskite Photovoltaics. *ACS Appl. Mater. Interfaces* **2016**.
109. Scheuermann, A. G.; Lawrence, J. P.; Meng, A. C.; Tang, K.; Hendricks, O. L.; Chidsey, C. E. D.; McIntyre, P. C., Titanium Oxide Crystallization and Interface Defect Passivation for High Performance Insulator-Protected Schottky Junction Mis Photoanodes. *ACS Appl. Mater. Interfaces* **2016**, *8*, 14596-14603.
110. Scheuermann, A. G.; Prange, J. D.; Gunji, M.; Chidsey, C. E. D.; McIntyre, P. C., Effects of Catalyst Material and Atomic Layer Deposited Tio2 Oxide Thickness on the

Water Oxidation Performance of Metal-Insulator-Silicon Anodes. *Energy & Environmental Science* **2013**, *6*, 2487-2496.
111. Bassiri, R., et al., Order, Disorder and Mixing: The Atomic Structure of Amorphous Mixtures of Titania and Tantala. *J. Non-Cryst. Solids* **2016**, *438*, 59-66.
112. Fitzgibbons, E. T.; Sladek, K. J.; Hartwig, W. H., Tio2 Film Properties as a Function of Processing Temperature. *J. Electrochem. Soc.* **1972**, *119*, 735-739.
113. Mergel, D.; Buschendorf, D.; Eggert, S.; Grammes, R.; Samset, B., Density and Refractive Index of Tio2 Films Prepared by Reactive Evaporation. *Thin Solid Films* **2000**, *371*, 218-224.
114. Ottermann, C. R.; Bange, K., Correlation between the Density of Tio2 Films and Their Properties. *Thin Solid Films* **1996**, *286*, 32-34.
115. Richards, B. S., Single-Material Tio2 Double-Layer Antireflection Coatings. *Sol. Energy Mater. Sol. Cells* **2003**, *79*, 369-390.
116. Lichterman, M. F.; Carim, A. I.; McDowell, M. T.; Hu, S.; Gray, H. B.; Brunschwig, B. S.; Lewis, N. S., Stabilization of N-Cadmium Telluride Photoanodes for Water Oxidation to O2(G) in Aqueous Alkaline Electrolytes Using Amorphous Tio2 Films Formed by Atomic-Layer Deposition. *Energy & Environmental Science* **2014**, *7*, 3334-3337.
117. Hanson, K.; Losego, M. D.; Kalanyan, B.; Parsons, G. N.; Meyer, T. J., Stabilizing Small Molecules on Metal Oxide Surfaces Using Atomic Layer Deposition. *Nano Lett.* **2013**, *13*, 4802-4809.
118. Andreiadis, E. S.; Chavarot-Kerlidou, M.; Fontecave, M.; Artero, V., Artificial Photosynthesis: From Molecular Catalysts for Light-Driven Water Splitting to Photoelectrochemical Cells. *Photochem. Photobiol.* **2011**, *87*, 946-964.
119. Kim, D. H.; Losego, M. D.; Hanson, K.; Alibabaei, L.; Lee, K.; Meyer, T. J.; Parsons, G. N., Stabilizing Chromophore Binding on Tio2 for Long-Term Stability of Dye-Sensitized Solar Cells Using Multicomponent Atomic Layer Deposition. *PCCP* **2014**, *16*, 8615-8622.
120. Vannucci, A. K.; Alibabaei, L.; Losego, M. D.; Concepcion, J. J.; Kalanyan, B.; Parsons, G. N.; Meyer, T. J., Crossing the Divide between Homogeneous and Heterogeneous Catalysis in Water Oxidation. *Proceedings of the National Academy of Sciences* **2013**, *110*, 20918-20922.
121. Lauinger, S. M.; Piercy, B. D.; Li, W.; Yin, Q.; Collins-Wildman, D. L.; Glass, E. N.; Losego, M. D.; Wang, D.; Geletii, Y. V.; Hill, C. L., Stabilization of Polyoxometalate Water Oxidation Catalysts on Hematite by Atomic Layer Deposition. *ACS Appl. Mater. Interfaces* **2017**, *9*, 35048-35056.
122. Shang, Q.; Piercy, B. D.; Losego, M. D.; Lian, T., Effect of Surface Ligand on Charge Separation and Recombination at Cspbi3 Perovskite Quantum Dot/Tio2 Interfaces. *The Journal of Physical Chemistry C* **2019**, *123*, 21415-21421.
123. Busani, T.; Devine, R. A. B., Dielectric and Infrared Properties of Tio 2 Films Containing Anatase and Rutile. *Semicond. Sci. Technol.* **2005**, *20*, 870.
124. Gorham, C. S.; Gaskins, J. T.; Parsons, G. N.; Losego, M. D.; Hopkins, P. E., Density Dependence of the Room Temperature Thermal Conductivity of Atomic Layer Deposition-Grown Amorphous Alumina (Al2o3). *Appl. Phys. Lett.* **2014**, *104*, 253107.
125. Iatsunskyi, I.; Pavlenko, M.; Viter, R.; Jancelewicz, M.; Nowaczyk, G.; Baleviciute, I.; Załęski, K.; Jurga, S.; Ramanavicius, A.; Smyntyna, V., Tailoring the

Structural, Optical, and Photoluminescence Properties of Porous Silicon/Tio2 Nanostructures. *The Journal of Physical Chemistry C* **2015**, *119*, 7164-7171.
126. Low Temperature Temporal and Spatial Atomic Layer Deposition of Tio2 Films. *Journal of Vacuum Science & Technology A: Vacuum, Surfaces, and Films* **2015**, *33*, 041512.
127. DeCoster, M. E., et al., Density and Size Effects on the Thermal Conductivity of Atomic Layer Deposited Tio2 and Al2o3 Thin Films. *Thin Solid Films* **2018**, *650*, 71-77.
128. Nunez, P., et al., Characterization of Electronic Transport through Amorphous Tio2 Produced by Atomic Layer Deposition. *The Journal of Physical Chemistry C* **2019**, *123*, 20116-20129.
129. Swanson, H. E.; McMurdie, H. F.; Morris, M. C.; Evans, E. H., Standard X-Ray Diffraction Powder Patterns. In *Monograph*, National Bureau of Standards: 1969; Vol. 25, p 82.
130. Jin, C.; Liu, B.; Lei, Z.; Sun, J., Structure and Photoluminescence of the Tio2 Films Grown by Atomic Layer Deposition Using Tetrakis-Dimethylamino Titanium and Ozone. *Nanoscale Research Letters* **2015**, *10*, 95.
131. Miller, T. M.; Bederson, B., Atomic and Molecular Polarizabilities-a Review of Recent Advances. In *Advances in Atomic and Molecular Physics*, Bates, D. R.; Benjamin, B., Eds. Academic Press: 1978; Vol. Volume 13, pp 1-55.
132. Cahill, D. G.; Watson, S. K.; Pohl, R. O., Lower Limit to the Thermal Conductivity of Disordered Crystals. *Physical Review B* **1992**, *46*, 6131-6140.
133. Costescu, R. M.; Bullen, A. J.; Matamis, G.; O'Hara, K. E.; Cahill, D. G., Thermal Conductivity and Sound Velocities of Hydrogen-Silsesquioxane Low-K Dielectrics. *Physical Review B* **2002**, *65*, 094205.
134. Hsieh, W.-P.; Losego, M. D.; Braun, P. V.; Shenogin, S.; Keblinski, P.; Cahill, D. G., Testing the Minimum Thermal Conductivity Model for Amorphous Polymers Using High Pressure. *Physical Review B* **2011**, *83*, 174205.
135. Hatori, K.; Taketoshi, N.; Baba, T.; Ohta, H., Thermoreflectance Technique to Measure Thermal Effusivity Distribution with High Spatial Resolution. *Rev. Sci. Instrum.* **2005**, *76*, 114901.
136. Freedman, J. P.; Leach, J. H.; Preble, E. A.; Sitar, Z.; Davis, R. F.; Malen, J. A., Universal Phonon Mean Free Path Spectra in Crystalline Semiconductors at High Temperature. *Scientific Reports* **2013**, *3*.
137. Schmidt, A. J.; Chen, X.; Chen, G., Pulse Accumulation, Radial Heat Conduction, and Anisotropic Thermal Conductivity in Pump-Probe Transient Thermoreflectance. *Rev. Sci. Instrum.* **2008**, *79*, 114902.
138. Hopkins, P. E.; Serrano, J. R.; Phinney, L. M.; Kearney, S. P.; Grasser, T. W.; Harris, C. T., Criteria for Cross-Plane Dominated Thermal Transport in Multilayer Thin Film Systems During Modulated Laser Heating. *J. Heat Transfer* **2010**, *132*, 081302.
139. Simmons, G. *Single Crystal Elastic Constants and Calculated Aggregate Properties*; SOUTHERN METHODIST UNIV DALLAS TEX: 1965.
140. Su, J.; Zou, X.-X.; Zou, Y.-C.; Li, G.-D.; Wang, P.-P.; Chen, J.-S., Porous Titania with Heavily Self-Doped Ti3+ for Specific Sensing of Co at Room Temperature. *Inorg. Chem.* **2013**, *52*, 5924-5930.

141. Xing, M.; Fang, W.; Nasir, M.; Ma, Y.; Zhang, J.; Anpo, M., Self-Doped Ti3+-Enhanced Tio2 Nanoparticles with a High-Performance Photocatalysis. *J. Catal.* **2013**, *297*, 236-243.
142. Li, M.; Hebenstreit, W.; Diebold, U.; Tyryshkin, A. M.; Bowman, M. K.; Dunham, G. G.; Henderson, M. A., The Influence of the Bulk Reduction State on the Surface Structure and Morphology of Rutile Tio2 (110) Single Crystals. *The Journal of Physical Chemistry B* **2000**, *104*, 4944-4950.
143. Amano, F.; Nakata, M.; Yamamoto, A.; Tanaka, T., Effect of Ti3+ Ions and Conduction Band Electrons on Photocatalytic and Photoelectrochemical Activity of Rutile Titania for Water Oxidation. *The Journal of Physical Chemistry C* **2016**, *120*, 6467-6474.
144. Hoang, S.; Berglund, S. P.; Hahn, N. T.; Bard, A. J.; Mullins, C. B., Enhancing Visible Light Photo-Oxidation of Water with Tio2 Nanowire Arrays Via Cotreatment with H2 and Nh3: Synergistic Effects between Ti3+ and N. *J. Am. Chem. Soc.* **2012**, *134*, 3659-3662.
145. Zuo, F.; Wang, L.; Wu, T.; Zhang, Z.; Borchardt, D.; Feng, P., Self-Doped Ti3+ Enhanced Photocatalyst for Hydrogen Production under Visible Light. *J. Am. Chem. Soc.* **2010**, *132*, 11856-11857.
146. Khomenko, V.; Langer, K.; Rager, H.; Fett, A., Electronic Absorption by Ti 3+ Ions and Electron Delocalization in Synthetic Blue Rutile. *Phys. Chem. Miner.* **1998**, *25*, 338-346.
147. Suriye, K.; Jongsomjit, B.; Satayaprasert, C.; Praserthdam, P., Surface Defect (Ti3+) Controlling in the First Step on the Anatase Tio2 Nanocrystal by Using Sol–Gel Technique. *Appl. Surf. Sci.* **2008**, *255*, 2759-2766.
148. Suriye, K.; Praserthdam, P.; Jongsomjit, B., Impact of Ti3+ Present in Titania on Characteristics and Catalytic Properties of the Co/Tio2 Catalyst. *Industrial & engineering chemistry research* **2005**, *44*, 6599-6604.
149. Di Valentin, C.; Pacchioni, G.; Selloni, A., Reduced and N-Type Doped Tio2: Nature of Ti3+ Species. *The Journal of Physical Chemistry C* **2009**, *113*, 20543-20552.
150. Deskins, N. A.; Dupuis, M., Intrinsic Hole Migration Rates in Tio2 from Density Functional Theory. *The Journal of Physical Chemistry C* **2008**, *113*, 346-358.
151. Deskins, N. A.; Rousseau, R.; Dupuis, M., Defining the Role of Excess Electrons in the Surface Chemistry of Tio2. *The Journal of Physical Chemistry C* **2010**, *114*, 5891-5897.
152. Simon, D. K.; Henke, T.; Jordan, P. M.; Fengler, F. P. G.; Mikolajick, T.; Bartha, J. W.; Dirnstorfer, I., Low-Thermal Budget Flash Light Annealing for Al2o3 Surface Passivation. *physica status solidi (RRL) – Rapid Research Letters* **2015**, *9*, 631-635.
153. Murota, J.; Sakuraba, M.; Ono, S., Silicon Atomic Layer Growth Controlled by Flash Heating in Chemical Vapor Deposition Using Sih4 Gas. *Appl. Phys. Lett.* **1993**, *62*, 2353-2355.
154. Sakuraba, M.; Murota, J.; Watanabe, T.; Sawada, Y.; Ono, S., Atomic-Layer Epitaxy Control of Ge and Si in Flash-Heating Cvd Using Geh4 and Sih4 Gases. *Appl. Surf. Sci.* **1994**, *82-83*, 354-358.
155. Wang, Z. L., From Nanogenerators to Piezotronics—a Decade-Long Study of Zno Nanostructures. *MRS Bull.* **2012**, *37*, 814-827.

156. Law, M.; Greene, L. E.; Johnson, J. C.; Saykally, R.; Yang, P., Nanowire Dye-Sensitized Solar Cells. *Nature Materials* **2005**, *4*, 455-459.
157. Huang, M. H.; Mao, S.; Feick, H.; Yan, H.; Wu, Y.; Kind, H.; Weber, E.; Russo, R.; Yang, P., Room-Temperature Ultraviolet Nanowire Nanolasers. *Science* **2001**, *292*, 1897.
158. Srikant, V.; Sergo, V.; Clarke, D. R., Epitaxial Aluminum-Doped Zinc Oxide Thin Films on Sapphire: I, Effect of Substrate Orientation. *J. Am. Ceram. Soc.* **1995**, *78*, 1931-1934.
159. Chen, Y.; Tuan, N. T.; Segawa, Y.; Ko, H.-j.; Hong, S.-k.; Yao, T., Stimulated Emission and Optical Gain in Zno Epilayers Grown by Plasma-Assisted Molecular-Beam Epitaxy with Buffers. *Appl. Phys. Lett.* **2001**, *78*, 1469-1471.
160. Hiroyuki, K.; Michihiro, S.; Kazuhiro, M.; Takafumi, Y., Effect of O/Zn Flux Ratio on Crystalline Quality of Zno Films Grown by Plasma-Assisted Molecular Beam Epitaxy. *Jpn. J. Appl. Phys.* **2003**, *42*, 2241.
161. Chen, Y.; Bagnall, D. M.; Koh, H.-j.; Park, K.-t.; Hiraga, K.; Zhu, Z.; Yao, T., Plasma Assisted Molecular Beam Epitaxy of Zno on C -Plane Sapphire: Growth and Characterization. *J. Appl. Phys.* **1998**, *84*, 3912-3918.
162. Ogata, K.; Maejima, K.; Fujita, S.; Fujita, S., Growth Mode Control of Zno toward Nanorod Structures or High-Quality Layered Structures by Metal-Organic Vapor Phase Epitaxy. *J. Cryst. Growth* **2003**, *248*, 25-30.
163. Karpina, V. A., et al., Zinc Oxide – Analogue of Gan with New Perspective Possibilities. *Cryst. Res. Technol.* **2004**, *39*, 980-992.
164. Bielinski, A. R.; Kazyak, E.; Schlepütz, C. M.; Jung, H. J.; Wood, K. N.; Dasgupta, N. P., Hierarchical Zno Nanowire Growth with Tunable Orientations on Versatile Substrates Using Atomic Layer Deposition Seeding. *Chem. Mater.* **2015**, *27*, 4799-4807.
165. Kukushkin, S. A.; Osipov, A. V.; Romanychev, A. I., Epitaxial Growth of Zinc Oxide by the Method of Atomic Layer Deposition on Sic/Si Substrates. *Physics of the Solid State* **2016**, *58*, 1448-1452.
166. Särkijärvi, S.; Sintonen, S.; Tuomisto, F.; Bosund, M.; Suihkonen, S.; Lipsanen, H., Effect of Growth Temperature on the Epitaxial Growth of Zno on Gan by Ald. *J. Cryst. Growth* **2014**, *398*, 18-22.
167. Kopalko, K.; Godlewski, M.; Domagala, J. Z.; Lusakowska, E.; Minikayev, R.; Paszkowicz, W.; Szczerbakow, A., Monocrystalline Zno Films on Gan/Al2o3 by Atomic Layer Epitaxy in Gas Flow. *Chem. Mater.* **2004**, *16*, 1447-1450.
168. Kopalko, K.; Wójcik, A.; Godlewski, M.; Łusakowska, E.; Paszkowicz, W.; Domagała, J. Z.; Godlewski, M. M.; Szczerbakow, A.; Świątek, K.; Dybko, K., Growth by Atomic Layer Epitaxy and Characterization of Thin Films of Zno. *physica status solidi (c)* **2005**, *2*, 1125-1130.
169. Kaiya, K.; Yoshii, N.; Takahashi, N.; Nakamura, T., Atmospheric Pressure Atomic Layer Epitaxy of Zno on a Sapphire (0001) Substrate by Alternate Reaction of Zncl2 and O2. *J. Mater. Sci. Lett.* **2000**, *19*, 2089-2090.
170. Kaiya, K.; Yoshii, N.; Omichi, K.; Takahashi, N.; Nakamura, T.; Okamoto, S.; Yamamoto, H., Atmospheric Pressure Atomic Layer Epitaxy of Zno Using a Chloride Source. *Chem. Mater.* **2001**, *13*, 1952-1956.

171. Özgür, Ü.; Alivov, Y. I.; Liu, C.; Teke, A.; Reshchikov, M. A.; Doğan, S.; Avrutin, V.; Cho, S. J.; Morkoç, H., A Comprehensive Review of Zno Materials and Devices. *J. Appl. Phys.* **2005**, *98*, 041301.
172. Fujimura, N.; Nishihara, T.; Goto, S.; Xu, J.; Ito, T., Control of Preferred Orientation for Znox Films: Control of Self-Texture. *J. Cryst. Growth* **1993**, *130*, 269-279.
173. Guo, J.; Chang, H. L. M.; Lam, D. J., Substrate Surface Step Effects on Microstructure of Epitaxial Films. *Appl. Phys. Lett.* **1992**, *61*, 3116-3117.
174. Tsivion, D.; Schvartzman, M.; Popovitz-Biro, R.; Joselevich, E., Guided Growth of Horizontal Zno Nanowires with Controlled Orientations on Flat and Faceted Sapphire Surfaces. *ACS Nano* **2012**, *6*, 6433-6445.
175. Givargizov, E. I., Graphoepitaxy as an Approach to Oriented Crystallization on Amorphous Substrates. *J. Cryst. Growth* **2008**, *310*, 1686-1690.
176. Jur, J. S.; Sweet, W. J.; Oldham, C. J.; Parsons, G. N., Atomic Layer Deposition of Conductive Coatings on Cotton, Paper, and Synthetic Fibers: Conductivity Analysis and Functional Chemical Sensing Using "All-Fiber" Capacitors. *Adv. Funct. Mater.* **2011**, *21*, 1993-2002.
177. Iii, W. J. S.; Oldham, C. J.; Parsons, G. N., Conductivity and Touch-Sensor Application for Atomic Layer Deposition Zno and Al:Zno on Nylon Nonwoven Fiber Mats. *Journal of Vacuum Science & Technology A* **2015**, *33*, 01A117.
178. Huang, M. H.; Wu, Y.; Feick, H.; Tran, N.; Weber, E.; Yang, P., Catalytic Growth of Zinc Oxide Nanowires by Vapor Transport. *Adv. Mater.* **2001**, *13*, 113-116.

VITA

Brandon Deane Piercy is a Washington State native, where he was raised from an early age steeped in education, practical engineering, and music. Brandon spent his formative years in Soundview School, an arts- and science-focused elementary and middle school founded by his parents, Alan and Inae Piercy. At Soundview, Brandon developed wide-ranging interests in literature, science, computers, music, and art through many late nights in the school library. During this time, one of Brandon's science teachers, a former Boeing engineer, had a module about composites where the class designed and built composite armors, capable of stopping a potato cannon from everyday household supplies. This experience ignited Brandon's interest in the study of materials science. In 2008, Brandon graduated from the Lakeside School, further broadening his experiences through international travel and service, theater, and more chemistry studies. In 2008, Brandon began attending Case Western Reserve University to pursue his B.S. degree in materials science and engineering with minors in polymer science and engineering and entrepreneurship. In 2012, Brandon graduated *magna cum laude* from CWRU and began work as a research engineer at De Nora Tech, Inc., a supplier of electrolysis modules for the chemical and metal plating industries. In 2014, Brandon began his Ph. D. in materials science and engineering under Prof. Mark Losego at the Georgia Institute of Technology. At Georgia Tech, Brandon spent a considerable amount of time cleaning up old defunct laboratories and designing and building tools and infrastructure for a new generation of thin film research, while occasionally conducting science on the side. Several collaborators at Emory University were instrumental in providing time and equipment to work on a variety of projects that could leverage the nascent ALD tooling still under

construction at the Losego lab. In 2017, Brandon joined Apple Inc. for an internship working on decorative PVD coatings and returned in the summer of 2018 to finish his dissertation work on pulsed-heating atomic layer deposition. Brandon has accepted a position after his Ph. D. with Apple to continue developing his interest in industrial applications of thin films, complex systems, and international travel and experiences.